CANADIAN THESES ON MICROFICHE

I.S.B.N.

THESES CANADIENNES SUR MICROFICHE

National Library of Canada
Collections Development Branch

Canadian Theses on
Microfiche Service

Ottawa, Canada
K1A 0N4

Bibliothèque nationale du Canada
Direction du développement des collections

Service des thèses canadiennes
sur microfiche

NOTICE

The quality of this microfiche is heavily dependent upon the quality of the original thesis submitted for microfilming. Every effort has been made to ensure the highest quality of reproduction possible.

If pages are missing, contact the university which granted the degree.

Some pages may have indistinct print especially if the original pages were typed with a poor typewriter ribbon or if the university sent us a poor photocopy.

Previously copyrighted materials (journal articles, published tests, etc.) are not filmed.

Reproduction in full or in part of this film is governed by the Canadian Copyright Act, R.S.C. 1970, c. C-30. Please read the authorization forms which accompany this thesis.

AVIS

La qualité de cette microfiche dépend grandement de la qualité de la thèse soumise au microfilmage. Nous avons tout fait pour assurer une qualité supérieure de reproduction.

S'il manque des pages, veuillez communiquer avec l'université qui a conféré le grade.

La qualité d'impression de certaines pages peut laisser à désirer, surtout si les pages originales ont été dactylographiées à l'aide d'un ruban usé ou si l'université nous a fait parvenir une photocopie de mauvaise qualité.

Les documents qui font déjà l'objet d'un droit d'auteur (articles de revue, examens publiés, etc.) ne sont pas microfilmés.

La reproduction, même partielle, de ce microfilm est soumise à la Loi canadienne sur le droit d'auteur, SRC 1970, c. C-30. Veuillez prendre connaissance des formules d'autorisation qui accompagnent cette thèse.

THIS DISSERTATION
HAS BEEN MICROFILMED
EXACTLY AS RECEIVED

LA THÈSE A ÉTÉ
MICROFILMÉE TELLE QUE
NOUS L'AVONS REÇUE

NL-339 (r. 82/08)

Canada

Measurements of Hyperfine Fields in Some Concentrated Magnetic Alloys Using Mossbauer Isotopes of Fe, Sn, Te, Ir and Au.

Submitted in partial fulfillment of the requirements for the Degree of Doctor of Philosophy at Dalhousie University,

Department of Physics,

June, 1984.

In memory of

Bill Leiper

TABLE OF CONTENTS

LIST OF FIGURES

LIST OF TABLES

ABSTRACT

The hyperfine fields have been measured at Te, Sn, Au, Ir and Fe nuclei located at impurity sites in several Heusler alloys. The value of the hyperfine field at Te impurities on Sb sites in Pd_2MnSb was found to be 85(3) T. This result along with subsequent work indicates the existance of a maximum in the hyperfine fields measured at 5sp impurities at Sb sites in Pd_2MnSb which is consistant with the charge screening models of Campbell and Blandin and of Jena and Geldart but is inconsistant with the volume misfit model of Stearns. The Mossbauer spectra of Sn, Au, and Ir nuclei in PtMnSn and IrMnSn indicate poorly ordered structures. The small Sn fields, -2.9(2) and 3.57(8) T respectively, follow general trends observed for 5sp impurities in transition metal and Heusler hosts. The 4.2 K hyperfine fields at Au impurities on Pt sites in PtMnSn and at Ir atoms in IrMnSn, 77(1) T and 65(2) T respectively, are used to compare the observed trends in the hyperfine fields at period six impurities in Heusler alloys with the predictions of the charge screening models. The magnitudes and signs of hyperfine fields measured at Fe impurities located on various sites in Co_2MnZ (Z=Si,Ge,Sn,Ga) and Co_2YSn (Y=Ti,Zr,Hf) have been measured by doping separate samples of each alloy with enriched ^{57}Fe and with ^{57}Co. In the Co_2MnZ alloys, Fe was found to preferentially occupy the Mn sites and possess a field value of about -30 T while Fe located on the Co sites was found to be -11.5 T for alloys with Group IVA Z atoms and -7.5 T for Z=Ga. A strong correlation was found to exist between the isomer shifts at Fe impurities in these alloys and the atomic number of the Z atom. In the Co_2YSn alloys, Fe was found to enter both the Y and Sn sites giving field values of -35 T and -30 T respectively except for Y=Zr where a separate Sn-site field was not resolved. The magnitude of the hyperfine fields at Fe impurities located at Co sites was found to be less than 2 T. These Fe field systematics are compared to those found in intermetallic compounds of similar structure.

LIST OF SYMBOLS AND ABBREVIATIONS

A	Activity of product nucleus after neutron irradiation.
A, B, C, D	Site designations for the X,Y,X,Z atoms in the $L2_1$ Heusler alloy X_2YZ.
A_n	Natural fractional isotopic abundance of the Mossbauer nuclide.
A_Z	Hyperfine coupling constant of an atom of atomic number Z.
$\mathbf{A}$	Vector potential of gamma radiation field.
a	Lattice parameter.
$a^+_{m',m''}$, $a^-_{m',m''}$	Amplitudes of right and left circularly polarized components of gamma photons during a resonant absorption process.
BC	Blandin-Campbell model of hyperfine fields at impurity atoms in magnetic hosts.
B2	Strukturbericht designation for the CsCl-type structure.
C	Empirical proportionality constant in Stearns' "volume misfit" contribution to hyperfine fields at non-magnetic impurity atoms (E5.7.3).
CB	Caroli-Blandin theory of conduction electron polarization.
CEP	conduction electron polarization.
C1	Strukturbericht designation for the fluorite structure.
$C1_b$	Strukturbericht designation for the Heusler-like structure of the type AuMnSb.
c	Speed of light in a vacuum.
DF	Daniel-Friedel model of hyperfine fields at impurity atoms in concentrated magnetic hosts.

DO_3	Strukturbericht designation for the Fe_3Si type structure.
d	Spacing between adjacent Miller planes.
EFG	Electric field gradient.
E_A	Excitation energy of the Mossbauer state (E3.4.4).
E_D	First order shift in the gamma ray energy due to the Doppler effect.
E_F	Fermi energy.
E_i, E_f	Initial and final energies of nuclei undergoing resonant absorption or emission.
$E(k, \uparrow)$ $E(k, \downarrow)$	Free electron-like energies of spin ↑ and spin ↓ subbands in the DF model.
E	Gamma ray energy.
e	Electronic charge.
eQ	Electric quadrupole moment.
$e^+_{m',m''}$, $e^-_{m',m''}$	Amplitudes of right and left circularly polarized components of gamma photons during the resonant emission process.
F(hkl)	Geometric form factor.
f(T)	temperature dependent Mossbauer fraction.
f_A, f_B, f_C, f_D	Average atomic structure factors for atoms located on sites A, B, C, D respectively.
f_A, f_S	Mossbauer fractions for absorber and source nuclei respectively.
fcc	Face centred cubic.
f_n	Atomic scattering factor for the n^{th} atom in the unit cell.
G	Reciprocal lattice translation vector.
$g(\omega)$	Phonon frequency distribution.

$\mathcal{H}$	Quantum mechnical Hamiltonian.
$H(Z)$	Hyperfine field calculated as a function of the atomic number Z of the sp impurity atom using Stearms' Volume Misfit Model (E5.7.1).
H_Q	Hamiltonian for the electric quadruploe interaction.
H_{eQ}	Diagonalized Hamiltonian for the electric quadrupole interaction.
$H_{exp}(Cd)$	Experimental value of the hyperfine field measured at the Cd sites in the host of interest as used in Stearns' Volume Misfit model (E5.7.4).
$H_h(Z)$	Contribution to the hyperfine field due to the CEP of the host matrix in Stearns' Volume Misfit model (E5.7.1).
$H_i(Z)$	Contribution to the hyperfine field due to the "volume misfit" of the impurity atom in the host (E5.7.1).
$H_{jm',jm''}$	Matrix element for the absorption or emission process.
H_M	Hamiltonian for the magnetic dipole interaction.
$H_V(Z)$	Stearns' empirical approximation to the volume overlap contribution to the hyperfine field at non-magnetic impurities in magnetic hosts (E5.7.3).
$H_W(A)$	Hyperfine field measured A nuclides located on site W (W=X,Y,Z).
H_1	Perturbation Hamiltonian for the resonant absorption or emission process.
h,k,l	Miller indicies.
h_0, h_1, h_2	Empirically determined proportionality constants between the local, first and second nearest neighbouring magnetic atoms and their contributions to the local hyperfine field (E5.8.1).
$\hbar$	Planck's constant divided by 2π.

I_i	Cartesian components (i=x,y,z) of nuclear spin.
I',I"	Nuclear spins of the upper and lower states respectively during a Mossbauer transition.
$I_0(x)$, $I_1(x)$	Zeroeth and first order hyperbolic Bessel functions of x.
I_+, I_-	Spin shift operators.
$I(E-E_0)$	Intensity of resonant gamma ray emitted as a function of the energy difference, $E-E_0$, from the centroid energy, E_0.
I(hkl)	Relative intensity of X-ray diffraction lines.
J	Value of the sd-exchange integral in the BC model (E5.5.3, E5.5.6).
JG	The Jena-Geldart model for hyperfine fields at sp impurity sites in Heusler alloy hosts.
J(0)	Value of the sd-exchange integral in the CB model (E5.3.4).
J	Nuclear current density.
j' , j"	Spin and parity of the upper and lower states of a Mossbauer transition (T3.7.1).
$K(T_A)$	Effective intensity of a Mossbauer absorbion line as a function of effective absorber thickness, T_A, (E3.4.7,8).
k	General wave vector; wave number for the Mossbauer gamma ray (E3.2.1).
k_i, k_f	Initial and final wave numbers respectively, for a nucleus undergoing resonant absorption or emission (E3.1.6).
L	Total angular momentum of each spherical harmonic component of a resonantly emitted or absorbed gamma ray (E3.6.4,5). Orbital angular momentum quantum number of one electron (E5.2.1) or of an atom (E5.2.4).
$L2_1$	Strukturbericht designation for the Heusler alloy of the Cu_2MnSn type.

l	Orbital angular quantum number of the l^{th} spherical harmonic component of the resonantly absorbed or emitted gamma ray (S3.6).
ME	Mossbauer effect.
m	Mass of recoiling nucleus (S3.1).
m_I	Magnetic quantum number of nucleus with spin I.
m', m''	Magnetic quantum numbers for the upper and lower levels in a Mossbauer transition.
N	Number of atoms in a solid.
N_c	Number of atoms per unit cell of a host (E5.5.7).
N_i	Number of magnetic atoms in the i^{th} coordination sphere of a non-magnetic impurity atom in the BC model (E5.5.13).
NMR	Nuclear magnetic resonance.
N_0	Initial number of target nuclei prior to neutron irradiation.
$N(v), N(\infty)$	Transmitted gamma ray intensities as a function of the Doppler shift velocity, v, and far from resonance respectively.
n	Half the total number of conduction electrons (E5.3.4) Number of conduction electrons per unit volume (E5.5.7).
n_A	Crossectional density of the Mossbauer nuclei in the absorber matrix.
n_c	Number of 3-d electrons contributed by each magnetic atom to the conduction band (E5.5.12).
n_0	Average number of electrons donated to the conduction band per atom (E5.5.7).
$n_\uparrow, n_\downarrow$	Numbers of conduction electrons of spin up and spin down (E5.3.4). Number of spin up and spin down 3d electrons per atom bound on magnetic ions (E.5.5.11).

P	Probablity for the resonant emission or absorption of a Mossbauer gamma ray without a change in the phonon state of the host crystal (E3.2.1).
PAC	Perturbed angular correlations.
p_j^i	The effective s-CEP at the inpurity atomic site in units of polarized s-electrons per atom per B induced by the j^{th} neighbour atoms (E5.8.2).
$\mathbf{p}$	Momentum of the emitting or absorbing nucleus (E3.3.2).
$\hat{\mathbf{p}}$	Unit vector indicating the polarization of the gamma radiation field.
Q',Q"	Electric quadrupole moments of the upper and lower nuclear levels involved in Mossbauer transitions.
R	Recoil energy of a nucleus undergoing resonant absorption or emission.
RKKY	Ruderman-Kittel-Kasuya-Yosida theory of electron spin polarization.
$R_{l+1,l}e^{i\phi}$	Ratio of the reduced matrix elements for the l+1 multipole component to that for the l multipole component in a nuclear transition.
R_0'	Separation between the magnetic atom producing a CEP and the local non-magnetic atom in the CB model (E5.5.1).
R',R"	Radii of nuclei in their upper and lower nuclear states.
R_n	Position vector of for the n^{th} atom in a unit cell.
rf	Radio frequency.
r_0	Wigner-Seitz radius of the impurity atom in its elemental host as used in the DF and JG models.
r'	Radius of the spherically symmetric square well potential used in the CB model.
r	Position vector of an atomic electron with respect to its nucleus (E5.2.1).

r_m	Position of the m^{th} inequivalent site relative to its fcc lattice point.
s	Spin of a gamma photon.
S	Spin of an atomic electron (E5.2.1); of all atomic electrons (E5.2.4).
S_n^2	Spin operator for the localized electronic moment (E5.3.4).
$s_\uparrow, s_\downarrow$	Densities of the spin up and spin down at a nuclear site (E5.2.4).
s-CEP	Polarization of s-like coduction electrons.
s_n	Location of the n^{th} fcc lattice point relative to the sc lattice point.
T	Temperature.
T_A	Effective absorber thickness.
t	Irradiation time during neutron irradiation (E4.2.1).
$t_{1/2}$	Half-life of the product nucleus (E4.2.1).
U(0)	Effective wave function for the valence-like k-dependent conduction electrons within the nuclear volume as used in the DF model of CEP (E5.4.5,6).
V_h	Volume occupied by the impurity atom in a magnetic host (E5.7.3).
V_Z	Volume occupied by an atom in its elemental host (E5.7.3).
$V_{ij} = \frac{\partial^2 V}{\partial i \partial j}$	The negative of the EFG tensor.
$V(\uparrow_\downarrow)$	Spin dependent depth of the square-well scattering potential at impurity atoms as used in the DF model (E5.4.3).
$V(\Delta Z)$	Depth of the square-well scattering potential at impurity atoms in the absence of CEP (E5.4.3).

v	Velocity of the absorbing or emitting nucleus (E3.3.2). Relative velocity between source and absorber nuclei in a Mossbauer experiment (S3.4).
$W_{e,a}$	Relative resonant absorption intensity for a particular combination of the an emission transition in the source nuclei and an absorption transition in the absorber nuclei.
x_n, y_n, z_n	Cartesian coordinates of the n^{th} atom in the conventional fcc unit cell in units of the lattice parameter.
Z_{eff}	Effective nuclear charge, in units of the electronic charge, screened by scattered electrons (E5.5.8).
Z_V	Valence state of the impurity atom (E5.5.10).
$\langle E_n \rangle_T$	Thermal energy of the phonon state of a crystal.
$\langle f(\beta) \rangle$	Average over a unit sphere of $f(\beta)$ where β is a Euler angle.
$\langle j_1 m_1 j_2 m_2 \mid jm \rangle$	Clebsch-Gordan vector coupling coefficient linking the $j_1 m_1 j_2 m_2$ vector space to the $j_1 j_2 jm$ vector space.
$\langle jm_1 \mid D(\alpha,\beta,\gamma) \mid jm_2 \rangle$	Matrix element for the rotation operator $D(\alpha,\beta,\gamma)$ between states jm_1 and jm_2.
$\langle S_Z \rangle$	Average spin on the magnetic atom as used in the CB model (E5.5.3).
$\langle x \rangle$	Expectation value of x.
$\langle x^2 \rangle_T$	Thermal average of x^2.
$\lvert R_{l+1,l} \rvert^2$	Mixing ratio of the higher order multipole component to the next lowest one for the emission process.
$\lvert \varepsilon_+ \rangle, \lvert \varepsilon_- \rangle$	Spherical basis vectors for right and left circular polarizations.
$\lvert \Psi_S(0) \rvert^2$, $\lvert \Psi_A(0) \rvert^2$	Electronic densities at source and absorber nuclei.

α	Internal conversion coefficient.
α	Interaction strength (E5.3.1).
Γ/Γ_0	Thickness-broadened width of a Mossbauer absorption line in units of the natural width of the Mossbauer state.
$\alpha_a, \beta_a, \gamma_a$	Euler angles of the quantization axes of the absorbing nuclei relative to the direction of the incident gamma ray.
$\alpha_e, \beta_e, \gamma_e$	Euler angles of the quantization axes of the emittiong nuclei relative to the direction of the emitted gamma ray.
α', α''	Directionally-independent quantum numbers describing the upper and lower levels of a Mossbauer transition.
$\alpha^2(k_F)$	Bloch enhancement factor as used in the JG model (E5.6.1).
β	Fraction of all photons entering the absorber matrix which are due to Mossbauer transitions.
Γ	Full width at half maximum of the Lorentzian energy distribution of resonantly emitted or absorbed gamma rays.
Γ'	Thickness-broadened width of the Mossbauer absorption line.
Γ_D	Doppler broadened width of the energy distribution of resonantly absorbed photons in the absence of the Mossbauer effect.
Γ_γ	Partial width at half maximum due to decay by gamma emission.
ΔZ	Excess ionic charge on impurity atoms screened by conduction electrons as used in the DF model (E5.4.3).
Δ/E_F	Half of the splitting between the spin up and spin down conduction electron subbands as used in the DF model.
δ_{IS}	Isomer shift in the hyperfine absorption pattern.

$\delta^{j}_{m\,m}(\beta)$	β-dependent part of the matrix elements of the rotational operator $D(\ ,\ ,\ )$ between states jm_1 and jm_2.
δ_n	Electron spin polarization per unit volume as used in the DF model (E5.4.2).
$\delta n_R(0)$	Spin density at a nuclear site of a non-magnetic impurity due to conduction electrons polarized by magnetic atoms located on a spherical shell of radius R_0 (as used in the BC model).
$\delta n(r)$	Shift in the conduction electron density due to charge screening (E5.3.1).
$\delta n(0)$	Local CEP at non-magnetic impurity atoms as used in the JG model (E5.6.1).
δ_T	Thermal shifts in emitted and absorbed Mossbauer gamma rays due to the second-order Doppler shift.
δ_0^F	Phase shift for the scattered s-electrons in the CB model (E5.5.3).
$\delta(r)$	Dirac delta function centred at the nucleus (E5.2.1).
$\delta(r-R_0)$	Spherically symmetric Dirac delta function, located at a distance of R_0 from the magnetic impurity, which is used to determine the CEP in the BC model (E5.5.1).
ϵ	Half of the splitting between the electron spin subbands as used in the DF model. Half of the difference between the scattering potentials for conduction electrons of different spin as used in the BC model.
η	Assymmetry parameter in the expression for the electric quadrupole interaction (E3.5.4).
$\eta_l(k_F)$	Phase shift of scattered partial waves of angular momentum l.
$\eta(E_D)$	Fractional resonant absorption at Doppler shift energy E_D.
$\eta(v)$	Fractional resonant absorption at Doppler velocity v.

$\eta_\uparrow, \eta_\downarrow$	Phase shifts for spin up and spin down electrons due to scattering.
θ	Half the scattering angle for X-ray diffraction (E2.3.1).
θ_D	Debye temperature.
θ_E	Einstein temperature.
λ	Wavelength Decay constant for the product nuclei during neutron irradiation (E4.2.1).
μ_B	Bohr magneton.
μ_I	Magnetic moment on a nucleus of spin I.
μ_i	Magnetic moment on the magnetic atoms in the i^{th} coordination sphere of a non-magnetic impurity atom as used in the BC model (E5.5.13).
μ_N	Nuclear magneton.
μ_0, μ_1, μ_3	Magnetic moments on the probe atoms, their first, and second nearest neighbours respectively (E5.8.1).
μ', μ''	Maximum component of the magnetic dipole moment of nuclei in their upper and lower states respectively.
	Ratio of the circumference to the diameter of a circle. Parity of a gamma photon (E3.6.6).
$\rho_{bg}(0)$	Background conduction electron density at the impurity nuclear site due to scattered s-like electrons as usedin the DF model.
$\rho_{sc}(0)$	Electron density at the impurity nuclear site due to bound s-like conduction electrons as used in the DF model.
$\rho_x^{m',m''}$, x=e,a	Polarization density matrix for the emission and the absorption process respectively.
σ	Spin state of the conduction electrons ($=\pm 1$) as used in the BC model.

$\sigma_{eff}(E)$	Energy-dependent effective cross section for resonant absorption.
σ_p	Cross section of product nuclei for thermal neutrons.
σ_s	Cross section of target nuclei for thermal neutrons.
σ_o	Maximum value for the cross section for resonant absorption of Mossbauer gamma rays.
τ	Mean lifetime of an unstable nuclear state.
$\tau_{1/2}$	Half life of the Mossbauer excited state.
ϕ	Neutron flux.
ψ	Total phase shift of scattered electrons.
Ω_0	Atomic volume.
	Angular frequency of a photon.
ν_D	Debye frequency.
ν_E	Einstein frequency.

ACKNOWLEDGEMENTS

I should like to express my graditude to the several individuals without whom this project would not have been completed. To Dr. R. A. Dunlap, I wish to extend my appreciation for his patient guidance and perseverance while deciphering my cryptic penmanship in the bulk of this manuscript. I wish to acknowledge Dr. G. Stroink for his interest in seeing that it reach completion. During the course of the experimental work Dr. C. Blaauw provided much appreciated expertise and assistance. Stimulating discussions and assistance with the computer analysis from J. Judah, C. Walls, and G. Lines was much appreciated. I wish to thank B. Fullerton for preparing the samples and C. Muir for the photographing the equipment. However, I cannot express my indebtedness to the late Dr. W. Leiper for his incessant enthusiasm, friendly encouragement and guidence during the course of the experimental work and the early stages of the preparation of this manuscript. To the staff of the Physics Department of Acadia University, particularly Ms. Julia Melzer for her expertise in typing equations, I wish to extend my appreciation of the comfortable working environment and apologies for any inconvenience I may have caused. I wish to thank my sister Cathy who swiftly turned most of my scrawled manuscript into bits and bytes so that it could be manipulated to produce what follows. Apologies are due to Barb who was forced to endure my absence at the least convenient times, and to my children, Angela and Kimberly who provided much needed distraction from the tedium. Finally, I wish to acknowledge the financial support provided by the National Research Council of Canada, the Faculty of Graduate Studies of Dalhousie University and the Walter C. Sumner Foundation.

CHAPTER 1

INTRODUCTION

§1.1 Theory of magnetism.

Since their discovery in antiquity, the magnetic materials have been a constant source of interest to scholars of natural philosophy because of their peculiar magnetic properties. Howeven, it was not until this century, during which the crystalline models of solids and the mathematical techniques of quantum statistics were developed, that any appreciable advances in the understanding of the mechanisms responsible for magnetic ordering were forthcoming.

The magnetic properties of insulators can be reasonably well understood in terms of Heisenberg exchange interactions between the localized magnetic moments on the atoms in the solid. On the other hand, the magnetic properties of metallic solids are not so well understood. Indeed, the origins of magnetism in one of the most common of the of the magnetic materials, pure iron, are rather poorly understood. Part of the diffculty arises from indirect interactions between magnetic ions via the conduction electrons. Another complication is due to the fact that the moment carrying d electrons are not so well localized as, for instance, the f electrons in the rare earth metals. This gives rise to a direct overlap of the wave functions for atoms that are suffiently close to each other in the solid. This overlap introduces an additional mechanism which affects the alignment of the magnetic moments leading to a particular type of magnetic order. Attempts to understand the magnetic ordering

mechanisms in pure transition metals have therefore been limited by the fact that the relative contributions are not well known.

S1.2 Hyperfine Field Measurements.

The original purpose of measuring hyperfine fields at non-magnetic impurities in magnetic metals was to determine the extent to which the conduction electrons were polarized by the presence of magnetic moments. A considerable effort was therefore directed toward the measurement of hyperfine fields at non-magnetic impurities in the pure transition metal hosts (Fe, Co, Ni) [R1.2.1]. However, as the number of different species of impurity atoms increased, it soon became apparent that the hyperfine field values were more a function of the particular impurity atom than of the host. As a result of these findings and the complicated atomic structure of impurity atoms dissolved in metallic environments, it was desirable to seek a simpler host where the magnetic ordering was thought to be primarily due to the polarized conduction electrons.

S1.3 Heusler Alloys.

Heusler alloys seemed to provide the ideal environment because in the X_2MnZ or XMnZ (X≠Co) alloys the nearest neighbour magnetic moments which are confined to Mn atoms are more separated than those in the pure transition metal ferromagnets. Because of the existence of a large number of these alloys which exhibit ferromagnetic ordering, they offer the opportunity to determine the effects of changing the

various constituent atoms on the magnetic properties. These unique properties led to a flurry of hyperfine field measurements at non-magnetic sites in Heusler alloys during the last decade [R1.3.1]. Details of the chemical and magnetic structure of Heusler alloys along with a summary of their magnetic properties are given in Chapter 2.

S1.4 Techniques for Measuring Hyperfine Fields.

Hyperfine fields may be measured most easily by using either the Mossbauer effect (ME), perturbed angular correlations (PAC) or nuclear magnetic resonance (NMR). Of these techniques the first two give the hyperfine fields at one particular type of atom in the alloy because a specific nuclide is used as a probe. The NMR technique, on the other hand is capable of allowing the determination of field values at several types of atoms in one experiment since the radio frequency is swept through a wide range which may cover the nuclear Zeeman splittings of several isotopes. Thus the ME and PAC techniques result in spectra which can be uniquely attributed to a specific nuclear species while the various absorption lines in an NMR spectrum must be identified with the various constituent atoms in the alloy. The choice between the use of the PAC and the ME techniques depends upon the type of probe atom of interest, since probe atoms suitable for each of these techniques do not exist for all the elements. In this work the ME technique only was used to measure hyperfine fields. The theory and the experimental procedures involved with ME are described in chapters 3 and 4 respectively.

S1.5 Theory of Hyperfine Fields in Metallic Hosts.

In the course of this and other work it became apparent that the trends observed in the hyperfine fields measured at non-magnetic impurities in ferromagnetic Heusler alloys were similar to those obtained in pure transition metal ferromagnets. Three theoretical models were developed to account for these trends. Two of these models, due to Blandin and Campbell [R1.5.1] and Jena and Geldart [R1.5.2], are applicable to non-magnetic probe atoms and attribute the change in the hyperfine field values to be due primarily to the screening of the varying ionic charges by the conduction electrons as the atomic number of the impurity atom is changed. The third, due to Stearns [R1.5.3], is more widely applicable in that it may be applied to magnetic atoms as well. According to this theory the magnetic hyperfine field trends are due to two separable effects: (a) the overlap between the extended moment carrying d electron wave functions of the host magnetic ions and the those of the impurity ions, and (b) the interaction between the spin polarized s-like conduction electrons of the host and the localized electrons on the impurity ions. In this theory the effective valence of the impurity ions are considered to be relatively constant across the sp series. These models are described in Chapter 5 where some attention is paid to the characteristics which distinguish them.

S1.6 Hyperfine fields measured in this work.

Most of the hyperfine field measurements in Heusler alloys had been made at 5sp constituent Z atom or transition constituent X atom sites. An important line of work was initiated by Campbell and Leiper [R1.6.1] and Schwartzendruber and Evans [R1.6.2] when they began substituting 5sp impurity atoms into Heusler alloys. Using these techniques it soon became apparent that for a given Heusler host, the hyperfine fields were negative for low valence 5sp impurities (Cd,In) and became more positive with increasing valance, changing sign near valence 4 (Sn). In this work, the magnitude of the hyperfine field at the Te (valence 6) impurity atoms in Pd_2MnSb was determined to see if the upward trend would continue. The details of this experiment are found in the second section of Chapter 6 (S6.2).

Previously the only measurements of hyperfine fields at period 6 atoms were on X sites in the Heusler alloy PtMnSn (H_X(Pt)) by Malik et al. [R1.6.3] and H_X(Au) in AuMnSb [R1.6.4] and in Au_2MnAl [R1.6.5] by Leiper et al. To extend these measurements in period 6, the values of H_X(Au) in PtMnSn and H_X(Ir) in $Ir_{1.07}Mn_{1.07}Sn_{0.86}$ were obtained in this work. The details of these measurements are found in S6.3 and S6.4 respectively. In S6.5 the values of the period 6 hyperfine field values measured in Heusler alloys are discussed in the context of the theoretical models.

In addition to the measurement of the hyperfine fields at the X atoms, the hyperfine field was also measured at the Z constituent atom in PtMnSn, and $Ir_{1.07}Mn_{1.07}Sn_{0.86}$. Details of these measurements

appear in S6.3 and S6.4 respectively.

Because of the existance of theoretical models which attempt to account for the experimental trends observed in magnetic hyperfine fields measured at non-magnetic sites, the bulk of the activity in the measurement of hyperfine fields in Heusler alloys has involved the use of non-magnetic probe atoms. Except for fields measured at Mn atoms, and Co atoms, little attention has been paid to the use of transition metal probe atoms, particularly those which might carry a moment. It should be pointed out that the recent theoretical models advanced to account for hyperfine field systematics at non-magnetic sites followed a rather substantial amount of experimental data chronologically. A similar situation is expected to occur for magnetic atoms. Thus, it would seem that there is a need to extend the hyperfine field measurements to atoms carrying magnetic moments.

With this in mind, several measurements of hyperfine fields at Fe impurity atoms in Co_2YZ alloys were made. The Co alloys were chosen because the ME nuclide ^{57}Fe can be incorporated into the Co sites by preparing the alloy with ^{57}Co, the parent nuclide of ^{57}Fe. By using these alloys as ME sources and a single line ME absorber the value of $H_{Co}(Fe)$ can be obtained. Also alloys prepared with small amounts of enriched ^{57}Fe were used as ME absorbers along with conventional single line sources to obtain hyperfine fields at Fe atoms located at other sites in the alloys. The experimental details of this work are found in S5.2 and the ME measurements are described in S7.2 and S7.3.

The final chapter contains a summary of the conclusions drawn from this work and some recommendations for future experiments.

S1.7 References.

R1.2.1 Rao, G.N., Atomic Data and Nuclei Data Tables, 15 (1975) 553.

R1.3.1 Campbell, C.C.M., J. Phys. F: Met. Phys. 5 (1975) 1931.

R1.5.1 Blandin A. and Campbell I.A. Phys. Rev. Lett. 31 (1973) 51. Campbell I.A. and Blandin A., J. Mag. Mag. Mat. 1 (1975) 1.

R1.5.2 Jena P. and Geldart D.J.W., Sol. St. Comm. 15 (1974) 139; J. Mag. Mag. Mat. 8 (1978) 99.

R1.5.3 Stearns M.B., Phys. Lett. A 34 (1971) 146; Phys. Rev. B 4 (1971) 4081, 8 (1973) 4383.

R1.6.1 Campbell C.C.M. and Leiper W., A.I.P. Conf. Proc. 18 (1973) 319.

R1.6.2 Schartzendruber L.J. and Evans B.J., A.I.P. Conf Proc. 10 (1972) 1369.

R1.6.3 Malik S.K., Damle S.D., and Vijayaraghavan R., Sol. St. Comm. 15 (1974) 953.

R1.6.4 Leiper W., Rush J.D., Thomas M.F., Johnson C.E., Woodhams F.W.D., Blaauw C., and MacKay G.R., J. Phys. F: Met. Phys. 7 (1977) 533.

R1.6.5 Leiper W., Blaauw C., MacKay G.R., and Woodhams F.W.D., J. Phys. F: Met. Phys. 11 (1976) 2191.

CHAPTER 2

HEUSLER ALLOYS

2.1 Introduction.

The study of the mechanisms responsible for magnetic ordering in Heusler alloys is important for several reasons:

(a) Most Heusler alloys have a simple cubic structure and tend to be well ordered both chemically and magnetically.

(b) There are a large number of alloys with which to vary relevant experimental parameters so as to test the theories of magnetic ordering.

(c) The distance between the magnetic moments for the X_2MnZ Heusler alloys is relatively large and is thought to preclude the possibility of direct exchange coupling being the dominant mechanism responsible for magnetic ordering. Although there is still some controversy over this point [R2.1.1, R2.1.2, R2.1.3], the study of Heusler alloys provides for a clearer understanding of the effect of conduction electrons on magnetic ordering.

(d) Continuous single phase solid solutions of two different Heusler alloys in the form of quarternary alloys ($Pd_2MnIn_{1-x}Sn_x$, [R2.1.4]; $Co_2Mn_{1-x}Ti_xSn$, [R2.1.5]) provide further experimental information with which to test current theories.

(e) The substitution of various probe atoms into the various lattice sites in Heusler alloys provides a means of determining the

systematics of impurity site hyperfine fields in ferromagnets. Because most metal atoms tend to selectively enter only one particular crystallographic site (A and C, B or D) [R2.1.6], the local environment of the impurity is known. Thus the impurity field measurements may also be used to advantage in the study of the hyperfine field trends in these alloys.

Because of these features, Heusler alloys offer the experimentalist a large variety of possible experiments which can lead to a clearer understanding of the role played by the conduction electrons in magnetic ordering.

S2.2 Structure of Heusler Alloys.

Heusler alloys are of chemical composition X_2YZ where X is a transition metal from the groups to the right of Fe in the periodic table (Co, Ni, Cu, Pd, Au, Pt, Rh), Y is a transition metal from groups to the left of Fe (Mn, Ti, V, Zr, Hf), and Z is an sp metal from groups IIIA, IVA, or VA (Al, Si, Ga, Ge, In, Sn, Sb). In this work the related ternary alloys, XYZ with vacancies on half of the X sites were also studied. Since it is now common practice to refer to these alloys as Heusler alloys, this practice although strictly incorrect will be adopted here. Not all combinations of these constituent atoms form the Heusler structure on alloying. Nevertheless, the number of Heusler alloys of different composition is large: a recent list of alloys of the $L2_1$ structure contains over one

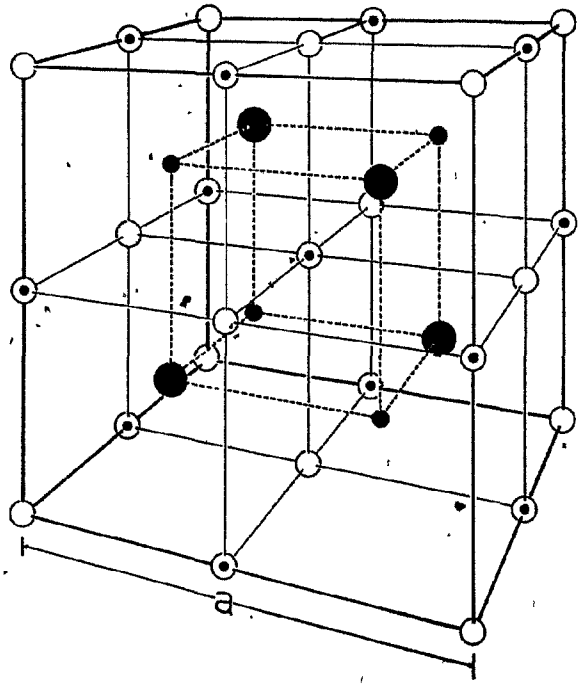

Site		Site occupancy				
Structure →		$L2_1$	B2	DO_3	$C1_b$	C1
Composition →		X_2YZ	X_2YZ	X_3Z	XYZ	XYZ
○	A	X	X	X	X	X
●	B	Y	Y,Z	X	Y	Y,Z
⊙	C	X	X	X	-	-
● (large)	D	Z	Y,Z	Z	Z	Y,Z

F2.2.1 The location and occupation of the four inequivalent sites in the conventional fcc unit cell of the structure for Heusler and related alloys. Where two types of atoms occupy the same site they are randomly distributed over equivalent sites in equal proportions.

hundred entries [R2.2.1].

These alloys are actually intermetallic compounds in that they usually exhibit a high degree of chemical order and exist in a single phase for only small departures from stoichometry. The X_2YZ and XYZ Heusler alloys order in what is refered to as the Strukturbericht types $L2_1$ and $C1_b$ respectively. These structural types have in common the fcc crystalographic lattice. They differ by the basis of atoms located at each lattice point. The basis may be considered to consist if four inequivalent sites, usually denoted by A, B, C, and D, located at the positions 0 0 0, 1/4 1/4 1/4, 1/2 1/2 1/2, and 3/4 3/4 3/4 respectively with respect to each lattice point. Thus, the structure

T2.2.2 Nearest neighbour configuration of four sites in Heusler alloys.

Shell	1nn	2nn	3nn	4nn	5nn	6nn
Radius*	$(3)^{1/2}$	$(4)^{1/2}$	$(8)^{1/2}$	$(11)^{1/2}$	$(12)^{1/2}$	$(19)^{1/2}$
A	4B,4D	6C	12A	12B,12D	8C	12B,12D
B	4A,4C	6D	12B	12A,12C	8D	12A,12C
C	4B,4D	6A	12C	12B,12D	8A	12B,12D
D	4A,4C	6B	12D	12A,12C	8B	12A,12C

* In units of $a/4$.

may be viewed as of four interpenetrating fcc sublattices displaced from each other along the body diagonal by one quarter of its length. The $L2_1$ structure is formed when the X atoms occupy the A and C sites, the Y atoms the B sites, and the Z atoms the D sites. The $C1_b$ structure is similar except that the C sites are vacant. These structures are shown in F2.2.1 where they are compared to related structures. The type and number of nearest neighbours to each of the sites in the Heusler structure are given in T2.2.1.

S2.3 Structure determination by x-ray diffraction.

X-ray diffraction was employed in this work in order to determine if the alloys used possessed a well ordered Heusler structure. A brief outline of the theory behind the analysis of the x-ray diffraction spectra of fcc crystal structures of the Heusler type is given below.

The condition for diffraction is given in terms of the wave vector of the x-rays, $\vec{k}$, and the reciprocal lattice vector, $\vec{G}$, as

$$2k\sin\theta = |\vec{G}| = (h^2+k^2+l^2)^{1/2}2\pi/a \qquad \text{E2.3.1}$$

which is equivalent to the usual expression for the Bragg diffraction law with $G=2\pi/\lambda$ and $d=a/(h^2+k^2+l^2)^{1/2}$. However, not all integral combinations of hkl will result in diffraction because x-rays coherently scattered from atoms on adjacent planes of particular orientations may interfere destructively. The intensity of the

diffracted x-ray beam is proportional to the square of the magnitude of the geometrical form factor given by:

$$F(hkl) \simeq \sum_{n=1}^{N} f_n e^{-i\vec{G}\cdot\vec{R}_n} \qquad \text{E2.3.2}$$

where f_n and $\vec{R}_n$ are, respectively, the the atomic scattering factor and the position vector of the n^{th} atom in the unit cell. The sum is over the N atoms of the unit cell. The position vectors are expressed as;

$$\vec{R}_n = (x_n\hat{x}+y_n\hat{y}+z_n\hat{z})a \qquad \text{E2.3.3}$$

This expression can be simplified by first summing over the inequivalent lattice sites per fcc lattice point and then over the inequivalent fcc lattice points per unit cell by writing $\vec{R}_n$ in the form:

$$\vec{R}_n = \vec{r}_m+\vec{s}_n \qquad \text{E2.3.4}$$

The $\vec{r}_m$ gives the relative position of each of the sites A, B, C, and D with respect to each fcc lattice point and may be given the values 0 0 0, $a/4$ $a/4$ $a/4$, $a/2$ $a/2$ $a/2$, and $3a/4$ $3a/4$ $3a/4$ respectively. The $\vec{s}_n$ gives the location of four inequivalent fcc lattice points with respect to the origin and may assume the values 0 0 0, 0 $a/2$ $a/2$, $a/2$ 0 $a/2$, and $a/2$ $a/2$ 0. This yields:

$$F(hkl) = \sum_m e^{-\vec{G}\cdot\vec{r}_m} \sum_n f_n e^{i\vec{G}\cdot s_n}$$

$$= [1+e^{-i\pi(k+l)}+e^{-i\pi(l+h)}+e^{-i\pi(h+l)}] \times$$

$$[f_A+f_C e^{-i\pi(h+k+l)}+(f_B+f_D e^{-i\pi(h+k+l)})e^{-i\pi(h+k+l)/2}] \quad \text{E2.3.5}$$

The atomic scattering factors f_i, i = A, B, C, D represent the <u>average</u> atomic scattering factor for the atoms on sublattice .

The first factor owes its existance to the fact that the lattice is of the fcc type. It vanishes unless hkl are all even or all odd integers in which case it has the value of 4. The second factor is due to the particular arrangement of atoms at each lattice point and further restricts the values of hkl which lead to diffraction. The value of this factor depends upon whether $h+k+l$ is even or odd and whether $(h+k+l)/2$ is even or odd. The possible values of hkl which give rise to diffraction are listed in T2.3.1 along with the values of $I(hkl)$ for arbitrary structures consisting of four fcc sublattices and the relative intensities for the fully ordered $L2_1$ and $C1_b$ structures.

As can be seen from T2.3.1 only reflections with $(h+k+l)/2$ even have intensities which are independent of the ordering of the X, Y, and Z atoms on the A, B, C, and D sites. The peaks in the diffraction spectrum which are due to these reflections are refered to as principal reflection lines in contrast to the others which are refered to as superlattice lines. In the extreme case, where the crystal is

T2.3.1 Geometrical form factors and relative intensities for Heusler alloys.

hkl	$h+k+l$	$(h+k+l)/2$	$F(hkl)/4$	$I(L2_1)$	$I(C1_b)$
odd	odd	-	$f_A-f_C \pm i(f_B-f_D)$	$(f_Y-f_Z)^2$	$f_X^2+(f_Y-f_Z)^2$
even	even	odd	$f_A+f_C-f_B-f_D$	$(2f_X-f_Y-f_Z)^2$	$(f_X-f_Y-f_Z)^2$
even	even	even	$f_A+f_C+f_B+f_D$	$(2f_X+f_Y+f_Z)^2$	$(f_X+f_Y+f_Z)^2$

completely randomly disordered, i.e. $f_A=f_B=f_C=f_D$, then the superlattice lines are absent in the diffraction spectrum. If disorder occurs among the atoms on the B and D sites, then the odd superlattice lines will be reduced while the even ones remain unchanged. In the extreme case of complete random disorder between these sites, the $L2_1$ and $C1_b$ structures become the B2 and C1 structures respectively. Preferential disorder of this type is found in some of the Co_2YZ alloys [R2.3.1] and in many $C1_b$ Heusler alloys [R2.3.2].

The amount of this type of disorder cannot be accurately determined from x-ray diffraction alone. Because the atomic scattering factors are monatonically increasing functions of the number of localized electrons on the atoms in the alloys, there are relatively small differences in the atomic scattering factors for

atoms with similar atomic numbers. Hence, the intensities of the superlattice lines are small compared to those of the principal lines. This is particularly relevent to the alloys studied in this work.

In this work x-ray diffraction was employed to compare the structure of the alloys prepared for ME analysis to those of previous workers. No attempt was made to determine quantitatively the extent to which disordering may have occurred. This can be justified to some extent by the fact that the resonant absorption lines of the Mossbauer spectra of these alloys are usually broadened or more numerous if there exists a variety of local order in the vicinity of ME probe atoms. A ME spectrum consisting of a simple arrangement of narrow absorption lines is usually indicative of uniform local order in the alloy. The lattice parameters (obtained from the relative spacing of the diffraction lines, see E2.3.1) were determined and compared to previous reported results. Also, care was taken to make sure of the absence of additional diffraction lines due to non-Heusler phases in the alloys. The x-ray diffraction measurements were made by Ben Fullerton.

S2.4 Magnetic Structures of Heusler Alloys.

The magnetic structure of Heusler alloys is best determined by means of the neutron diffraction technique. (Details of this technique applied to the determination of the magnetic structures of Heusler alloys are given by Webster [R2.4.1]). Most of the alloys containing Co or Mn are magnetically ordered with the magnetic moments

localized on these atoms only. A recent list of Heusler alloys of the $L2_1$ structure indicates that about 50 alloys exhibit some form of magnetic ordering [R2.4.2]. For the alloys of composition X_2MnZ ($X \neq Co$), the magnetic moments range from 3.27 μ_B for Ni_2MnSb to about 4.4 μ_B for Ni_2MnIn and Pd_2MnSb, however a value nearer 4 μ_B is more typical. In Heusler alloys of composition Co_2MnZ the size of the Co and Mn moments depends on the particular type of Z atom in the alloy. The Mn moments are 3.0, 3.6, and 3.75 μ_B for group IIIA, IVA, and VA atoms, respectively. The Co moments, however, fall into only two catagories: about 0.50 μ_B for group IIIA atoms and about 0.75 μ_B for group IVA and VA atoms. For the Co_2YZ ($Y \neq Mn$) alloys the systematics in the moments depend in a complicated way on the types of both Y and Z atoms. When Y and Z atoms are respectively group IVA and IIIA atoms or group VA and IVA atoms then the Co moment tends to be small, about 0.3 μ_B. However, when the Y and Z atoms are respectively group IVB and IVA atoms or group VB and IIIA atoms then the Co moment tends to be large, about 0.8 to 1.0 μ_B. The Heusler alloys of the $C1_b$ structure are much less numerous that the $L2_1$ alloys. As a rule the Mn moments are smaller in the XMnZ alloys and tend to vary more than in the $L2_1$ alloys, ranging between 2 and 4 μ_B. Because these alloys tend to be less well ordered than the $L2_1$ alloys it is difficult to see clear trends in the moments in these alloys.

Most (about 80 %) of the magnetically ordered $L2_1$ Heusler alloys are ferromagnetic. The other types of order found include antiferromagnetic order (eg Pd_2MnAl) and more complicated types such

as helical antiferromagnetic order (eg Ni_2MnAl [R2.4.3]). The magnetic ordering temperatures cover a wide range: 23 K for PdMnTe to 985 K for Co_2MnSi. For the X_2MnZ alloys the Curie points seem to depend mainly on the type of X atom, being highest for X=Co and decreasing as X in changed to Cu, Rh, Ni, Pd, and Ir in that order. For the XMnZ alloys the Curie points tend to be higher (by about a factor of 2) than the corresponding X_2MnZ alloy with the same X and Z atoms. For alloys of composition Co_2YZ (Y≠Mn), the Curie points cover a smaller range (119 K for Co_2NbSn to 444 K for Co_2ZrSn). The Curie points of these alloys follow the same trends as do the magnetic Co moments in their dependence on the type of Y and Z atoms.

The chemical and magnetic structure of the alloys used in this work appear in those sections in chapters 6 and 7 where the ME measurements are described.

S2.5 References.

R2.1.1 Stearns M.B., Phys. Rev. B 13 (1976) 4180.

R2.1.2 Campbell I.A. and Vincze I., Phys Rev B 13 (1976) 4178.

R2.1.3 Price D.C., Rush J.D., Johnson C.E., Thomas M.F., and Webster P.J., J. de Physique C-37 (1976) C6-317.

R2.1.4 Webster P.J. and Ramadan M.R.I. J. Mag. Mag. Mat. 20 (1980) 271.

R2.1.5 Dunlap R.A. and Stroink G., Can. J. Phys. 60 (1982) 909.

R2.1.6 Burch T.J., Budnick J.I., Niculescu V. A., Raj K., and Litventa T., Phys. Rev. B 24(2) (1981) 3866.

R2.2.1 Nakamichi T., Sci. Rep. RITU A 30(1) (1981) 3866.

R2.3.1 Webster P.J., J. Chem. Sol. 31 (1971) 1221; 34 (1973) 1647.

R2.3.2 Masumoto H. and Watanabe K., Trans. JIM 14 (1973) 408.

R2.4.1 Webster P.J. Cont. Phys. 10 (1969) 559.

R2.4.2 Nakamichi T., Sci. Rep. RITU A 30(1) (1981) 3866.

R2.4.3 Ziebeck K.R.A. and Webster P.J., J. Phys. F: Met. Phys. 5 (1975) 1756.

CHAPTER 3

MÖSSBAUER SPECTROSCOPY

S3.1 Resonant absorption.

Gamma ray resonant absorption consists of the emission of a gamma ray from a nucleus initially in an excited state and the subsequent absorption of this gamma ray by another nucleus initially in its ground state. This sequence of events is followed by the decay of the second nucleus to its ground state by one of several processes. The gamma ray energy distribution is given by the Breit-Wigner or Lorentz function:

$$I(E-E_o) \propto \frac{\Gamma/2\pi}{(E-E_o)^2+(\Gamma/2)^2} \qquad \text{E3.1.1}$$

where E_o is the energy centroid and Γ is the 'natural width' of the gamma ray. This last quantity is related to the mean lifetime, τ, of the excited state through the Heisenberg uncertainity relation,

$$\tau\Gamma \simeq \hbar \qquad \text{E3.1.2}$$

For ME excited states, the full widths range from 7×10^{-11} eV for ^{67}Zn to 6×10^{-5} eV for ^{187}Re. Typical values are about 10^{-8} eV.

The maximum cross section for resonant absorption is given by

$$\sigma_o = \frac{\hbar^2 c^2}{E_\gamma^2} \frac{2I'+1}{2I''+1} \frac{\Gamma_\gamma}{\Gamma} \qquad \text{E3.1.3}$$

where E is the energy of the photon, I'' and I' are the spins of the ground and excited states respectively. Γ_γ/Γ is the relative probability for a nuclear decay from the excited state by means of gamma emission. Where gamma emission and internal conversion are the principal modes of decay, Γ_γ/Γ is related to the conversion coefficient, α, by

$$\frac{\Gamma_\gamma}{\Gamma} = \frac{1}{1+\alpha} \qquad \text{E3.1.4}$$

For ME nuclides, the cross sections range from 3.2 b for ^{67}Zn to 1.7 x 10^6 b for ^{121}Ta while typical values are about 10^4 b or 10^5 b.

For free nuclei, both the emission and the absorption processes must conserve linear momentum. Hence the nucleus must recoil with a momentum, $\hbar\vec{k}$, where $\vec{k}$ is the wave number of the gamma ray. For initially stationary nuclei the energy of the recoil is given by:

$$R \equiv \frac{(\hbar k)^2}{2m} = \frac{1}{2m}\left[\frac{E_o - R}{c}\right]^2 \simeq \frac{E_o^2}{2mc^2} \qquad \text{E3.1.5}$$

where m is the nuclear mass, E is the gamma ray energy, and E_o is the

transition energy between the two nuclear states. Typical recoil energies for ME nuclides range from 10^{-4} to 0.1 eV. For non-stationary sources and absorbers of gamma rays, the resulting gamma ray energy is given by:

$$E = E_o \pm E_i \mp E_f$$

$$= E_o \pm \frac{(\hbar k_f)^2}{2m} \mp \frac{\hbar^2(\vec{k}_f - \vec{k}_i)^2}{2m}$$

$$= E_o \mp \frac{\hbar^2 k_f^2}{2m} \pm \frac{\hbar^2 \vec{k}_f \cdot \vec{k}_i}{m}$$

$$= E_o \mp R \pm \frac{\dot{E}}{c} v\cos\theta \qquad \text{E3.1.6}$$

where the upper and lower signs refer to the emission and absorption processes respectively. E_i and $\vec{k}_i$ (E_f and $\vec{k}_f$) are the initial (final) values of the kinetic energy and the wave number of the nucleus respectively. $\vec{v}$ is the initial value of the velocity of the nucleus and θ is the angle between $\vec{k}_i$ and $\vec{k}_f$. For a gas, the initial velocities of the nuclei are governed by a Boltzman distribution; hence, $\langle v\cos\theta \rangle = 0$, and the following averages result:

$$\langle E_\gamma \rangle = E_o \mp R \qquad \text{E3.1.7}$$

$$\langle E_\gamma^2 \rangle = \langle E_\gamma \rangle^2 \left[1 + \frac{\langle v^2 \cos^2 \theta \rangle}{c^2} \right] \qquad \text{E3.1.8}$$

The gamma ray energy is now centered at $E_0 \mp R$ and hence for maximum resonance absorption the emitted gamma ray must be externally augmented with an energy of $2R$. Furthermore, the width of the gamma ray distribution is increased from the natural width to:

$$\begin{aligned} \Gamma_D &\sim \left[\langle E_\gamma^2 \rangle - \langle E_\gamma \rangle^2 \right]^{1/2} \\ &\sim \langle E_\gamma \rangle \left[\langle v^2 \rangle \right]^{1/2} / c \\ &\sim \langle E_\gamma \rangle \left(k_B T / m \right) \\ &\sim \sqrt{2 m k_B T} \end{aligned} \qquad \text{E3.1.9}$$

For ME nuclides this corresponds to a range of .005 to .07 eV, an increase by a factor of 10^3 to 10^8 over the natural width. The effective maximum absorption cross section would be reduced by the same factor.

S3.2 Mossbauer effect.

When nuclei are bound within a crystal lattice, however, the total energy of the nucleus becomes quantized. For cases where the nuclei are bound by velocity independent forces within the crystal lattice, it can be shown the first two moments of the distribution of E are the same as those for unbound nuclei [R3.2.1]. Only higher order moments differ. At high temperatures these higher order moments become negligible because the nuclei are in states of high quantum numbers and the energy distribution approaches a continuum.

At low temperatures these higher order terms become important. In particular, at $T = 0$, the nuclei are moving with quantum mechanical zero-point motion. Because it is the minimum energy state for the lattice, a gamma ray can neither be emitted with energies larger than E_0 nor be absorbed with energies less than E_0. However, since the first two moments for the gamma-ray energy distribution are the same for bound or unbound nuclei, the probability for emission and absorption of gamma rays with energy equal to E_0 must be considerably different for bound nuclei than for unbound nuclei. It is this probability difference which is the basis of the Mossbauer effect.

The probability that an atom will remain in the same state upon emission or absorption of a gamma ray of wave number $\vec{k}$ is given by:

$$P = |\langle n|e^{-i\vec{k}\cdot\vec{x}}|n\rangle|^2 \qquad \text{E3.2.1}$$

and is referred to as the Mossbauer fraction. When calculating this

quantity the conventional approach is to use the harmonic approximation for the forces binding the atoms in the lattice. However, the harmonic approximation implicitly assumes infinite lifetimes for the phonon states by ignoring phonon - phonon interactions. In real solids these interactions and crystal imperfections reduce the phonon lifetimes to values much smaller than the typical lifetimes of the nuclear excited states. This can be taken into account explicitly by thermally averaging the matrix elements in E2.2.1 before squaring them to obtain the Mossbauer fraction [R3.2.2]. The result for the harmonic crystal is given by:

$$f = \exp\left[-k^2 \langle x^2 \rangle_T\right] \qquad \text{E3.2.2}$$

where $\langle x^2 \rangle_T$ indicates the thermal average of the displacement of the Mossbauer nuclei in the direction of gamma emission from the equilibrium positions in the crystal lattice. For one phonon frequency distribution, we find:

$$\langle x^2 \rangle_T = \frac{1}{3} \langle r^2 \rangle_T = \frac{\langle E_n \rangle_T}{3N m\omega^2} = \frac{\hbar}{m\omega} \left[\frac{1}{\exp(\hbar\omega/k_B T) - T} + \frac{1}{2}\right] \qquad \text{E3.2.3}$$

Here k_B is Boltzman's constant and T is the temperature. E_n is the energy of n^{th} eigenstate. One may now use a continuous phonon frequency distribution, $g(\omega)$ normalized for N atoms by:

$$3N = \int_0^\infty g(\omega)\, d\omega \qquad \text{E3.2.4}$$

to obtain:

$$f(T) = \exp\left\{ - \frac{k^2}{3Nm} \int_0^\infty \frac{1}{\omega^2} \langle E_n \rangle_T \, g(\omega)\, d\omega \right\}$$

$$= \exp\left\{ - \frac{\hbar k^2}{3Nm} \int_0^\infty \left[\frac{1}{\exp(\hbar\omega/k_B T)-1} + \frac{1}{2} \right] \frac{g(\omega)}{\omega}\, d\omega \right\} \qquad \text{E3.2.5}$$

For the Einstein solid only one frequency of oscillation, ω_E is assumed, so that

$$g(\omega) = 3N\, \delta(\omega-\omega_E) \qquad \text{E3.2.6}$$

where $\theta_E = \hbar\omega/k_B$ is the Einstein temperature. This yields:

$$f(T) = \exp\left\{ \frac{-R}{k_B \theta_E} \left[\frac{2}{\exp(\theta_E/T)-1} + 1 \right] \right\}.$$

$$\simeq \exp(-R/\hbar\omega_E) \text{ for } T \ll \theta_E \qquad \text{E3.2.7}$$

For the Debye model

$$g(\omega) = \begin{cases} \frac{9N\omega^2}{\omega_D} & 0<\omega<\omega_D \\ & \\ & \omega>\omega_D \end{cases} \qquad \text{E3.2.8}$$

Therefore we obtain:

$$f(T) = \exp\left\{-\frac{3R}{2k_B\theta_D}\left[1 + \frac{4T^2}{\theta_D{}^2}\int_0^{\theta_D/T}\frac{x}{e^x-1}\,dx\right]\right\}$$

$$\simeq \exp[-6R\ \chi(T,\theta_D)/k\theta_D] \qquad \text{E3.2.9}$$

where

$$\chi(T,\theta_D) = \begin{cases} 1/4, & T\simeq 0 \\ & \\ T/\theta_D, & T\gtrsim\theta_D/2 \end{cases} \qquad \text{E3.2.10}$$

Although the Debye model represents only a crude approximation to the distribution in the phonon frequency in real solids, it is in reasonable agreement with the temperature dependence of the Mossbauer fraction for most cubic systems where the phonon frequency distribution does not consist of widely separated bands [R3.2.3]. The reason for this is that the Mossbauer fraction is essentially a bulk property of the solid due to the fact that the nuclear gamma rays are

emitted during times much longer than typical phonon lifetimes. More details concerning the applicability of the Debye model to real solids in determining the temperature dependence of the Mossbauer fraction are given by Disatnik [R3.2.4].

In summary, the probability for nuclear resonance absorption is increased by choosing nuclei with low recoil energies; i.e. with small transition energies, and placing them in lattices where they are strongly bound giving high Debye temperatures, and finally by cooling the host matrix to low temperatures. For some of the ME nuclides used in this work measurements at T = 4.2 K were necessary in order to obtain sufficient resonant absorption to resolve the individual absorption lines.

S3.3 Thermal shifts.

It has already been indicated that in spite of the first order Doppler shift, there exists a significant fraction of unshifted gamma rays for source nuclei bound within a crystal lattice. Because of the fact that the Doppler broadened gamma rays have a much wider energy distribution and a much lower maximum resonant cross section, these gamma rays do not contribute to the conventional Mossbauer resonant absorption spectra.

However there also exists a second order Doppler shift in all gamma ray energies. This may be derived by considering the gamma ray to be a clock whose period is dilated because of the fact that its source is moving with respect to the stationary absorber nuclei. This

shift referred to as the thermal shift, is given by

$$\delta_T = -E_\gamma \frac{\langle v^2 \rangle_T}{2c^2} \qquad \text{E3.3.1}$$

Because of the velocity distribution of the emitting nuclei bound in a solid, one might expect the Mossbauer gamma rays to be Doppler broadened due to this shift. However, again due to the fact that during the emission of a gamma ray the emitting nucleus is effectively in a statistical average of photon states, all Mossbauer gamma rays are shifted the same amount and no broadening occurs. Thus Mossbauer gamma rays have the natural line width given by E2.1.2.

In view of fact that

$$\langle v^2 \rangle_T = \langle P^2 \rangle_T / m^2 = \langle \epsilon \rangle_T / m \qquad \text{E3.3.2}$$

the explicit temperature dependence of the thermal shift for a Debye solid is given by

$$\delta_T(T) = -\frac{9R}{E_\gamma}\left[\frac{k_B\theta_D}{8} + \left(\frac{T}{\theta_D}\right)^3 k_B T \int_0^{\theta_D/T} \frac{x^2}{e^x - 1}\, dx\right]$$

$$\simeq -\frac{9Rk_B\theta_D}{E_\gamma}\left[\frac{1}{8} + \frac{\pi^4}{15}\left(\frac{T}{\theta_D}\right)^4\right] \qquad \text{E3.3.3}$$

for $T \sim 0$. Because this shift is dependent upon the equilibrium and

Debye temperatures of the host it is present in all cases where the source and absorber nuclei are in different types of matrices and/or they are at different temperatures. Because the Debye temperatures tend to be of the order of room temperature for good Mossbauer matrices (see E3.2.10 and E3.2.11) the thermal shifts which are fourth order temperature effects tend to be small and can generally be neglected when compared to shifts due to hyperfine interactions.

S3.4 Lineshapes of Mossbauer absorption curves.

There are two basic methods of observing gamma ray response. Both methods involve the use of two matrices; one containing source nuclei, the other absorber nuclei. One of these matrices is usually a standard matrix in which the excited and ground leved of the Mossbauer nuclei remain wholly degenerate. Thus a single x-ray energy is emitted or absorbed. The other matrix is the one of interest. In the first method the emitted gamma rays, x-rays, or conversion electrons following resonant absorption of the absorber nuclei by the Mossbauer gamma rays from the source nuclei are detected as a function of the source gamma ray energy. This is referred to as the scattering geometry. In the second, the attenuation of a beam of Mossbauer gamma rays emitted from the source nuclei due to resonant absorption by the absorbing nuclei is detected as a function of source gamma ray energy. This is referred to as the transmission geometry. Since only the latter method was used in this work the former will not be discussed further.

Usually a relative velocity between source and absorber matrices is externally introduced to vary the relative gamma ray energies. The resulting shift in the gamma ray energy is obtained to first order in v/c from the relativistic Doppler frequency shift expression and is given by:

$$E_D = E_\gamma \frac{v}{c} \qquad \text{E3.4.1}$$

where v is the relative velocity between source and absorber (taken as positive when they are approaching each other), c is the velocity of light in vacuo and E_D is the gamma ray energy for $v = 0$.

It is customary in the literature to refer to shifts and splittings of nuclear energy levels in terms of this velocity. Hence both the absorber and sources matrices and their temperatures must be specified, as well as the Mossbauer nuclide if they are to be compared to the results of other experiments.

A transmision Mossbauer spectrum may thus be represented by

$$N(v) = N(\infty)[1-\eta(v)] \qquad \text{E3.4.2}$$

where $N(v)$ and $N(\infty)$ are the gamma ray intensities near and far from resonance respectively and $\eta(v)$ is the fractional resonant absorption velocity v.

For cases where the density of Mossbauer nuclei within the source matrix is sufficiently small so that resonant absorption of source gamma rays by source nuclei (self absorption) is negligible, and the nuclear levels are unsplit and indentical for all Mossbauer nuclei, $n(E_D)$ is given by:

$$n(E_D) = \beta f \int_{-\infty}^{\infty} \left\{1-\exp[-\sigma_{eff}(E)]\right\} I[E-(E_S+E_D)]\, dE \qquad \text{E3.4.3}$$

where β is the fraction of radiation detected due to the decay of source Mossbauer states and f_S is the Mossbauer fraction of the source. E_S is the excitation energy of the source nuclei, E_D is the externally introduced Doppler shift in the emission spectrum, given by E3.4.1 and $I(E-(E_S+E_D))$ is the Lorentzian energy distribution given by E3.1.1. $\sigma_{eff}(E)$ is the effective cross section for the absorber matrix. For cases where the Mossbauer atoms in the absorber matrix all occupy identical sites, and the nuclei states are unsplit, $\sigma_{eff}(E)$ is given by

$$\sigma_{eff}(E) = \sigma_o n_A f_A \frac{(\Gamma/2)^2}{(\Gamma/2)^2 + (E-E_A)^2} \qquad \text{E3.4.4}$$

where f_A and n_A are respectively the Mossbauer fraction of the absorber and linear density of Mossbauer nuclei in the absorber matrix, σ_o is the maximum resonant cross section given by E3.1.3, and

E_A is the excitation energy of the Mossbauer state in the absorber nuclei.

The coefficient of the Lorentzian function in E3.5.4 is usually referred to as the effective absorber thickness, T_A, which, in this case, is

$$T_A = \sigma_o n_A f_A \qquad \text{E3.4.5}$$

E3.4.3 has not been solved in closed form, however, the value of the maximum absorption has been obtained by Mossbauer and Weidemann [R3.4.1] and is given by:

$$n(E_S-E_A) = \beta f_S \left[1-\exp(T_A/2) I_o(T_A/2)\right] \qquad \text{E3.4.6}$$

where $I_0(x)$ is the zeroeth order hyperbolic Bessel function of x. The total absorption area has been found by Bykov and Hien [R3.4.2] to be

$$A = \int_{-\infty}^{\infty} \eta(E_D) dE_D = \beta F_S \frac{\Gamma}{2} \pi K(T_A) \qquad \text{E3.4.7}$$

Here $K(x)$ is defined by:

$$K(\chi) \equiv \chi e^{-\chi^2/2}[I_0(\chi/2) + I_1(\chi/2)] \qquad \text{E3.4.8}$$

where $I_1(\chi)$ is a first order hyperbolic Bessel function. Because for small T, E3.5.3 reduces to a Lorentzian function,

it is standard procedure to replace E3.4.3 with a Lorentzian function in which the full width at half maximum (FWHM) has been "thickness broadened". The effective FWHM is expressed as

$$\Gamma' = \alpha\Gamma \qquad \text{E3.4.9}$$

and the area under a Lorentzian of half width Γ' is related to the height of the peak by

$$A_L = \int \frac{I_0(\Gamma'/2)^2}{(\Gamma'/2)^2 + (E-E_0)^2}\, dE = \pi I_0 \Gamma'/2 \qquad \text{E3.4.10}$$

Using E3.4.2 to E3.4.10, one obtains the proportionality constant in E3.4.9 to be given by

$$\alpha = \frac{K(T_A)}{1-\exp(-T_A/2)I_0(T_A/2)} \qquad \text{E3.4.11}$$

In the limit as T_A becomes small, α approaches 2. Thus the minimum

observable Mossbauer absorption linewidth is twice the width of the excited state of the nucleus. This linewidth characterizes the resolution capability of the gamma ray associated with a particular Mossbauer nuclide when used in a transmission resonant absorption experiment. The Mossbauer widths are listed in T3.6.1 for the nuclides used in this work. Numerical calculations by Bykov and Hien [R3.4.2] indicate that the Lorentzian function deviates from E3.4.3 by less than 3 % for $T_A < 10$.

Although this calculation assumes identical and unsplit nuclear states in the Mossbauer nuclei in each matrix, these results are still valid if the absorption lines are well resolved, that is, separated by at least three half widths [R3.4.2]. In this case is multiplied by the relative probability for resonant absorption occurring between the two particular levels. Accurate analyses of unresolved spectra may require the direct application of E3.4.3 instead of a "sum of Lorentzians".

Another assumption in the derivation of E3.4.11 is that the source and absorber have equal widths. This may not be the case in general because small differences in the local environment from site to site of Mossbauer nuclei may result in distributions in the strength of the hyperfine interactions. The result is a broadened emission spectrum and a broadened effective cross section. The effect of different widths upon the validity of the use of a Lorentzian fitting funotion has been investigated by O'Conner [R3.4.3]. Assuming that the broadened emission spectra and broadened effective cross

section remain Lorentzian, then the resulting Mossbauer spectrum should remain Lorentzian, for $T_A < 4$, with a deviation of less than 2% of the actual value given by E3.4.3.

It would appear that the use of Lorentzians to fit Mossbauer spectra is justified, at least for well resolved absorption lines. In view of the computational time required to fit E3.4.3 directly to the experimental spectra, it is worthwhile to attempt to fit poorly resolved spectra with the simple "sum of Lorentzians" as well. In particular, since the major concern in this work is the determination of hyperfine fields and hence line positions only it would seem that a sum of Lorentzian approach is reasonable.

S3.5 Hyperfine Interactions.

The high resolution of gamma ray resonance techniques allows small changes in the nuclear states due to the presence of magnetic and electric fields to be readily detected. There are three important interactions between the nucleus and its environment:

(a) the electrostatic interaction between the nuclear charge and the non-zero electronic charge at the nucleus, which leads to the so called isomer shift of the resonant absorption line,

(b) the interaction between the electric quadrupole moment of the nucleus and electric field gradient at the nucleus, which leads to the "quadrupole splitting" of the resonant absorption line,

(c) the interaction between the magnetic dipole moment of nucleus and non-zero magnetic field at the nucleus, which leads to the "hyperfine splitting" of the resonant absorption line.

These three interactions are discussed briefly below.

S3.5.1 The isomer shift.

Because the nuclear charge is distributed over a finite volume, the interaction between this charge distribution and the electronic charge density in the same volume is a function of the nuclear eigenstates. The resulting energy perturbation is dependent upon both the electronic charge density at the nucleus and the particular state of the nucleus. Since two nuclear states are involved during gamma emission or absorption, the gamma ray energy shift is proportional to only the difference in the nuclear volumes of the two states. Furthermore, since gammma ray resonance reveals only the difference between the energies of the resonantly emitted gamma rays and those of the resonantly absorbed gamma rays, only the difference between the electron densities at source nuclei and at the absorber nuclei is measured. Assuming spherically symmetric nuclear and ionic charge distributions, the general form of this energy shift is given by:

$$\delta_{IS} = \frac{2}{5}\pi Ze^2[\langle R'^2\rangle - \langle R''^2\rangle][\,|\Psi_a(0)|^2 - |\Psi_s(0)|^2] \qquad \text{E3.5.1}$$

where a small correction due to relativistic effects has been omitted. Here Z is the nuclear charge on the Mossbauer nucleus, $\langle R'^2\rangle$ and $\langle R''^2\rangle$ are the expectation values of the square of the nuclear radii when the nucleus is in the excited and ground states respectively, and $|\Psi_a(0)|^2$ and $|\Psi_s(0)|^2$ are the electron densities (assumed constant) within the nuclear volume for absorber and source nuclei, respectively. Neglecting relativistic effects only electrons with zero angular orbital momentum (s electrons) have a finite probability of being at the nucleus.

However, indirect contributions may result because the s electron density at the nucleus is sensitive to the electrons of non-zero orbital angular momentum (p, d, and f electrons). Furthermore, in metallic matrices, the isomer shift is sensitive to the local conduction electron density, both directly for conduction electrons of s character and indirectly for conduction electrons of p, d, and f character. Thus isomer shift measurements at the same Mossbauer nuclide on the same site in a series of Heusler alloys reveal information about the relative conduction densities in these alloys.

S3.5.2 The electric quadrupole splitting.

Nuclei with non-spherical nuclear charge distributions (spins not equal 0 or 1/2) may have some of the orbital degeneracy of the nuclear energy levels lifted in the presence of electric fields. The typical non-spherical distortions of the nuclear charge density are such that only the interaction between the quadrupole moment (eQ) of an electric multipole expansion of the nuclear charge distribution and the gradient of the electric field (EFG) is important. Because nuclear charge distributions are the same for orbital s states differing only in the sign of the nuclear magnetic quantum number (m_I), these states remain degenerate. The Hamiltonian for the interaction is given by:

$$H_Q = \frac{eQ}{6I(2I-1)} \sum_{ij} V_{ij}[3I_iI_j-\delta_{ij}I(I+1)] \qquad \text{E3.5.2}$$

where I_i, I_j are components ($i,j = x,y,z$) of the nuclear spin I. δ_{ij} is the Kronecker delta and $-V_{ij} = -\partial^2V/\partial_i\partial_j$ is the EFG tensor.

Choosing the coordinate system so that the V_{ij} is diagonalized and

$$|V_{xx}| \leq |V_{yy}| \leq |V_{zz}| \qquad \text{E3.5.3}$$

$$H_{eq} = \frac{eq^2Q}{4I(2I-1)} [3I_z^2 - I(I+1) + \frac{\eta}{2}(I_+^2+I_-^2)] \qquad \text{E3.5.4}$$

Here $eq=V_{zz}$, and $\eta= (V_{xx}-V_{yy})/V_{zz}$ is the asymmetry parameter. I_+ and I_- are the shift operators for the nuclear states. Because only the spherically symmetric s electrons possess a finite probability of occuring at the nucleus, Laplace's equation applies and $0\leq\eta\leq1$.

There two main contributions to the EFG at nuclei in lattices of less than cubic symmetry. Firstly, the surrounding ions (usually taken as point charges) may give rise to a non-zero EFG at the atomic site. This contibutes to a EFG at the nuclear site directly and also indirectly by distorting the otherwise spherically symmetric wave functions of the electrons around the nucleus. This effect is referred to as Sternheimer antishielding because the effective EFG is enhanced by the distortion. The total EFG so produced is referred to as the ligand contribution. Secondly, the nuclear spins may orient the local valence electrons. This results in a direct contribution to the EFG at the nucleus and in addition an indirect contribution due to the distortion of the spherically symmetric filled electron shells. Since this distortion tends to oppose the direct contribution, it is referred to as Sternheimer shielding. The total EFG produced this way is referred to as the valance contribution. For nuclei in a cubic environment the ligand contribution vanishes. In metallic hosts the valence electrons enter the conduction band causing the valence contribution to vanish when the crystal structure is of high symmetry.

S3.5.3 Magnetic dipole splitting.

A magnetic field at a nucleus of non-zero spin removes all of the spin degeneracy of the nuclear state splitting it into $2I+1$ sublevels. The Hamiltonian operator for this interaction is given by

$$H_M = -\vec{\mu}_I \cdot \vec{H}_A(X)$$

$$= -g\mu_N \hat{I} \cdot \vec{H}_A(X) \qquad \text{E3.5.5}$$

where $\vec{H}_A(X)$ is the effective magnetic field strength at X nuclides located on A sites; μ_I is the nuclear magnetic dipole moment; $\hat{I}$ is the nuclear spin operator; g is the Lande g factor for the nucleus; and $\mu_N = 5.050951\ 10^{-27}$ J/T is the nuclear magneton. The resulting $2I+1$ energy perturbations are:

$$E_{m_I} = -g\mu_N H_A(X)\, m_I \qquad \text{E3.5.6}$$

where $m_I = (-I, -I+1, \ldots I-1, I)$ is the nuclear magnetic quantum number.

In addition to being a measure of the hyperfine interaction strength, E3.5.6 also provides the basis for an operational definition of the hyperfine magnetic field.

In order to define $H_A(X)$, both its magnitude and its orientation must be constant for times greater than the characteristic time associated with experimental technique of measurement. For ME this time is the mean life time of the Mossbauer state, τ.

S3.6 Relative intensities of resonant absorption lines.

The relative intensity of resonant absoption lines for a variety of physical situations have been discussed by Misra [R3.6.1], Kundig [R3.6.2], Wong [R3.6.3], Dehn et al [R3.6.4], and Frauenfelder et al [R3.6.5]. What follows is an outline of the theory involved in the calculation of these relative intensities.

Because in the resonant emission or absorption process, the total angular momentum of the system is conserved, the quantum mechanical theory of angular momentum plays a dominant role in the discussion. Several texts have been written on this subject: for example, Brink and Satchler [R3.6.6], Edmonds [R3.6.7], and Rose [R3.6.8]. Unfortunately the notation and conventions used by these authors vary considerably although cross references are found in the appendices of the first reference. These various notations coupled with the rather complex expressions involved in the theory provides for some difficulty in using expressions from different authors to arrive at the desired result. Rather than go through the detailed mathematical expressions, a physical explanation of the derivation is presented in the following paragraphs.

According to first order perturbation theory, the transition probabilities are proportional to the matrix elements of the perturbing Hamiltonian between the initial and final nuclear states. This perturbation is due to the electromagnetic field in the region of the emitting or absorbing nucleus. These matrix elements may be written as

$$H_{j'm',j''m''} = \langle \alpha' j' m' | H_1 | \alpha'' j'' m'' \rangle \qquad \text{E3.6.1}$$

Here j,m are respectively the quantum numbers for the total angular momentum and one component of the angular momentum of the relevent nuclear states. The single primes denote the excited states and the double primes the ground state. Other quantum numbers which are collectively symbolized as are irrelevent to this discussion since only the angular momentum quantum numbers determine relative intensities of absorption lines.

To first order in the vector potential of the gamma radiation field, the appropriate perturbation Hamiltonian is

$$H_1 = \vec{A} \cdot \vec{J} \qquad \text{E3.6.2}$$

where $\vec{J}$ is just the nucleon current density.

The use of only this first order term is reasonable because the second order term which is the diamagnetic term is usually several orders of magnetude less than the Zeeman term for the magnetic fields encountered here (Park [R3.6.9]).

The vector potential may be regarded as a plane wave with polarization denoted by the unit vector $\hat{p}$. Thus

$$H_1 = \vec{A} \cdot \hat{p} e^{i\vec{k}\cdot\vec{r}} \qquad \text{E3.6.3}$$

where $\vec{k}$ is the wave vector and $\vec{r}$ the displacement vector from the

nucleus located at the origin. For electromagnetic radiation, the polarization vector is perpendicular to the direction of propagation, i.e. $\hat{p}\cdot\vec{k} = 0$. To take advantage of the conservation of angular momentum, this plane wave can be expanded as a series of spherical harmonics which are the angular momentum eigenfunctions. The coefficents of each term in the multipole expansion are spherical Bessel functions of kr and order ℓ, the angular momentum quantum number for each term. Since, for nuclear dimensions, $r \sim 10^{-4}$ and for transition energies of about 20 keV, $kr \sim 10^{-3}$ nm for any of these terms (ℓ=1,2,3 ...). Under these circumstances the spherical Bessel functions are of the order of $(kr)\ell \sim 10^{-3}\ell$. Thus each term is about a factor of 1000 times smaller than the preceding term in the series. Hence only the first term in the expansion which gives rise to a non-vanishing matrix element of the form of E2.5.1 is sufficient to obtain the transition probability.

The total angular momentum of the photon during the emission (or absorption) process is composed of two components, the orbital angular momentum due to the spatial dependence of the plane wave function with respect to the emitting (or absorbing) nucleus and the intrinsic spin angular momentum due to the polarization state of the photon. Since S=1 for photons, these numbers are related by

$$L = \ell, \ell \pm 1 \qquad \text{E3.6.4}$$

By convention L=ℓ represents magnetic 2^L pole ML radiation while

$L=\ell\pm1$ represents electric 2^L pole or EL radiation. The lower limit placed upon in the multipole expansion which contributes to the emitted or absorbed photon is set by E2.5.4 together with the conservation of angular momentum and of parity. The former restricts the values of L to

$$|j'-j''| \leq L \leq j'+j'' \qquad \text{E3.6.5}$$

and the latter requires the change in the parity of the nuclear states during the transition to equal that of the photon which is given by

$$\pi = (-1)^{\ell+1} \qquad \text{E3.6.6}$$

These matrix elements for the emission process can be written in the form of a vector in two dimensional polarization space with $\mathbf{k}$ parallel to $\hat{\mathbf{z}}$ [R3.6.1]:

$$|em'm''\rangle = e^{+}_{m'm''}|\varepsilon_{+}\rangle + e^{-}_{m'm''}|\varepsilon_{-}\rangle \qquad \text{E3.6.7}$$

where $|\varepsilon_{+}\rangle$ and $|\varepsilon_{-}\rangle$ are the spherical basis vectors corresponding to right and left circularly polarized radiation respectively. Here the dependence of the coefficients $e^{+}_{m'm''}$ and $e^{-}_{m'm''}$ on the $j'm'$ and $j''m''$ values for the two lowest terms in the multiple expansion are given by [R3.6.1]:

$$e^{+}_{m'm''} = \exp(i\alpha_e)\ [\langle j''m''\ell M|j'm'\rangle \delta^{\ell}_{1M}(\beta_e)$$

$$+ R_{\ell+1,\ell} e^{i\phi} \langle j''m'',\ell+1,M|j'm'\rangle \delta^{\ell+1}_{1M}(\beta_e)] \qquad \text{E3.6.8}$$

$$e^{-}_{m'm''} = \exp(-i\alpha_e)\ [\langle j''m''\ell M|j'm'\rangle \delta^{\ell}_{-1M}(\beta_e)$$

$$- R_{\ell+1,\ell} e^{i\phi} \langle j''m'',\ell+1,M|j'm'\rangle \delta^{\ell+1}_{-1M}(\beta_e)] \qquad \text{E3.6.9}$$

Similarly for the absorption process the matrix elements can be written

$$|\alpha m'm''\rangle = a^{+}_{m'm''}|\varepsilon_+\rangle + a^{-}_{m'm''}|\varepsilon_-\rangle \qquad \text{E3.6.10}$$

where

$$a^{+}_{m'm''} = \exp(i\alpha_a)\ [\langle j''m''\ell -M|j'm'\rangle \delta^{\ell}_{-1-M}(\beta_a)$$

$$-R_{\ell+1,\ell} e^{-i\phi} \langle j''\ell+1,m'',-M|j'm'\rangle \delta^{\ell+1}_{-1-M}(\beta_a)] \qquad \text{E3.6.11}$$

and

$$a^{-}_{m'm''} = \exp(i\alpha_a)\ [\langle j''\ell''m'', -M | j'm'\rangle \delta^{\ell}_{1-M}(\beta_a)$$

$$R_{\ell+1,\ell} e^{-i\phi} \langle j''\ell+1m'', -M | j'm'\rangle \delta^{\ell+1}_{1-M}(\beta_a)] \qquad \text{E3.6.12}$$

In the above equations α_x, β_x, and γ_x are the Euler angles which give the axis of quantization in the source ($x=e$) or absorber ($x=a$). The functions $\delta^{j}_{M_1M_2}(\beta)$ are the β-dependent part of the matrix elements of the rotation operator $D(\alpha,\beta,\gamma)$ between states jm_1 and jm_2 [R3.6.10].

$$\langle jm_1 | D(\alpha,\beta,\gamma) | jm_2\rangle = \exp(im_1\alpha)\ \delta^{j}_{m_1m_2}(\beta)\ \exp(im_2\gamma) \qquad \text{E3.6.13}$$

The quantities $\langle j_1m_1j_2m_2 | jm\rangle$ are the Clepsch-Gordan coefficients which are the expansion coefficients which give the state $|j_1j_2jm\rangle$ in the $2j+1$ dimensional space in terms of the $|j_1m_1j_2m_2\rangle$ state functions in the $(2j_1+1)(2j_2+1)$ dimensional space. Tables of values for the functions $\delta^{j}_{m_1m_2}(\beta)$ and the Clepsch-Gordan coefficients can be found in the books mentioned earlier or in R3.6.11.

The value of $R_{\ell+1,\ell} e^{i\phi}$ is the ratio of the so called reduced matrix element for the $\ell+1$ multipole term to that of the multiple term. These reduced matrix elements depend only on the total angular momenta of the two nuclear states and of the photon together with other variables which describe the nuclear states but do not depend on the values m', m'' and the direction in which the photon is travelling.

The square of this quantity is referred to as the mixing ratio for the two multipole terms.

All physical information regarding each process is contained in the density matrix for that process which is defined as follows:

$$\rho_x^{m',m''} = |xm'm''><xm'm''| = \begin{vmatrix} |x_+|^2 & x_+x_-^* \\ x_-^*x_+ & |x_-|^2 \end{vmatrix}, \quad x = e, a \qquad \text{E3.6.14}$$

The relative probability for the absorption of a photon by transition $t=m_a' \rightarrow m_a''$ which was emitted by means of transition is $s=m_s' \rightarrow m_s''$ obtained from the trace of the density matrix:

$$W_{e,a} = Tr(\rho_e^s \rho_a^t) \qquad \text{E3.6.15}$$

If the Mossbauer source is a single line unpolarized source, then the emission density matrix is proportional to the unit matrix and the relative absorption lines are determined entirely by the absorption density matrix. This was generally the case for the hyperfine field measurements in the work. However, the ^{197}Au and ^{125}Te work involved hyperfine field measurements in the source matrix. In these cases a single line unpolarized absorber was used so that the absorption density matrix was proportional to unity and the desired relative intensities are given by trace of the emission density matrix.

The transition probabilities given by E2.5.15 are for oriented nuclei and are functions of β which gives the angle between the quantization axis of the nuclei and the direction of propagation of the gamma rays. To obtain the relative intensities for the case where randomly oriented polycrystalline absorbers or sources are used, this function must be averaged over a unit sphere using:

$$\langle f(\beta)\rangle = \frac{1}{2}\int_0^{\pi} f(\beta)\,\sin(\beta)\,d\beta \qquad \text{E3.6.16}$$

All Mossbauer nuclides used in this work possessed excited and ground states of the same parity and $|j' - j''| = 1$. Hence, the radiation was mainly of the M1 type. For ^{193}Ir and ^{197}Au there was a significant E2 component which has the same parity as M1 radiation. The intensity ratios used in this work for polycrystalline absorbers (or sources) are given in the next section.

S3.7 Characteristics of Mossbauer isotopes used in this work.

The pertinent characteristics of the Mossbauer nuclides used in this work are given in T3.7.1. The relative positions and the relative intensities of the individual absorption lines of the magnetically split Mossbauer patterns for the five isotopes used in this work are given in T3.7.2 and T3.7.3. These values are given for

T3.7.1 Nuclear properties of Mossbauer Nuclides.

Mossbauer Nuclide	^{57}Fe	^{119}Sn	^{125}Te	^{193}Ir	^{197}Au
Parent Nuclide	^{57}Co	$^{119}Sn^{m}$	^{125}Sb	^{193}Os	^{197}Pt
E_γ (keV)	14.412	28.875	35.48	73.0	77.34
Γ (eV x 10^{-2})	0.195	0.258	0.541	1.48	7.63
$\tau_{1/2}$ (ns)	99.3	18.3	1.535	6.2	1.892
R (mm/s)	0.23	0.625	5.02	0.60	1.87
j''^{π}, j'^{π}	$1/2^-, 3/2^-$	$1/2^+, 3/2^+$	$1/2^+, 3/2^+$	$3/2^+, 1/2^+$	$3/2^+, 1/2^+$
Radiation type	M1	M1	M1	M1+E2	M1+E2
$(R_{E2,M1})^2$	-	-	-	0.31	0.11
σ_o (b)	2.57	1.40	0.28	0.03	0.041
α	8.17	5.12	12.7	6	4.0
μ'' (μ_N)	+0.0904206	-1.04621	-0.8872	+0.1589	+0.14486
μ' (μ_N)	+0.15491	+0.682	+0.60	+0.470	+0.4165
Q'' (b)	0	0	0	+1.5	+0.56
Q' (b)	0.2	-0.08	-0.2	0	0
A_n (%)	2.17	8.58	6.99	61.5	100

* For a defination of the above symbols see the List of Symbols.

T3.7.2 Magnetic Hyperfine Splitting Pattern for ^{57}Fe, ^{119}Sn, ^{125}Te.

Transition $m' \leftarrow m''$	$-M=m''-m'$	Relative Intensity	Relative Position ^{57}Fe	^{119}Sn	^{125}Te
+3/2 +1/2	-1	3	+0.5000	-0.5000	-0.5000
+1/2 +1/2	0	2	+0.2514	-0.3625	-0.3650
-1/2 +1/2	+1	1	+0.0686	-0.2370	-0.2299

T3.7.3 Magnetic Hyperfine Splitting Pattern for ^{193}Ir and ^{197}Au

Transition $m' \leftarrow m''$	$-M=m''-m'$	Relative Intensity ^{193}Ir	^{197}Au	Relative Position ^{193}Ir	^{197}Au
+1/2 +3/2	-1	1.000	1.000	-0.5000	-0.5000
+1/2 +1/2	0	0.766	0.670	-0.6702	-0.6778
+1/2 -1/2	+1	0.486	0.391	-0.8405	-0.8556
+1/2 -3/2	+2	0.235	0.097	-0.6767	-1.0333

only one half of the possible transitions because a magnetic hyperfine splitting pattern exhibits mirror symmetry about the unsplit level in the absence of an electric quadrupole interaction. This symmetry in both the ground and excited states of Mossbauer nuclei produces a Mossbauer spectrum which has mirror symmetry about the position centroid of the individual absorption lines. The values for the other half of the transitions are obtained by changing the signs of all explicitly signed entries in the two tables.

The relative positions are given in units of the separation between the positions of the two most intense absorption lines. The signs are appropriate to the case where Mossbauer radiation from unsplit source nuclei is resonantly absorbed by magneticly split ramdomly oriented absorber nuclei. All signs should be changed for the case where radiation from magneticly split source nuclei is absorbed by unsplit nuclei. However, because of the mirror symmetry, the resulting Mossbauer spectrum for this latter case is identical to that of the former case.

The integral intensities given in T3.7.2 result from the fact that the E2 component of the Mossbauer radiation of these nuclides is negligible. Hence, they are numerically equal to the square of the appropriate Clepsch-Gordan coefficients. In T3.7.3, however, where this is not the case, the intensities are given relative to the most intense lines.

S3.8 References.

R3.2.1 Lipkin, Harry J., Quantum Mechanics, New Approaches to Selected Topics, North-Holland Pub. Co., (1973) 48-50.

R3.2.2 Ibid. 80-88.

R3.2.3 Disatnik Y. Lectures on the Mossbauer Effect (J. Danon ed.), Gordon and Breach (1968) 14.

R.3.4.1 Mossbauer, R.L. and Wiederman, W.H.Z. Physik 159 (1960) 33.

R3.4.2 Bykov, G.A. and Hien, P.Z., Sov. Phys. JETP 16 (1963) 646.

R3.4.3 O'Connor D.A., Nuc. Instr. Meth. 30 (1964) 290.

R3.6.1 Misra, S.K., Il Nuovo Cimento, 59 (1969) 152.

R3.6.2 Kundig W., Nuc. Instr. Meth. 48 (1967) 219.

R3.6.3 Wong M.K.F., Phys. Rev. 149 (1966) 378.

R3.6.4 Dehn J.T., Marzalf J.G., and Salmon J.F., Phys. Rev. B 135 (1964) 1307.

R3.6.5 Frauenfelder H., Nagle D.E., Taylor R.D., Cochran D.R.F., Visscher W.M., Phys. Rev. 126 (1962) 1065.

R3.6.6 Brink D.M. and Satchler G.R., Angular Momentum (2nd Ed.), Oxford University Press, (1968).

R3.6.7 Edmonds A.R., Angular Momentum in Quantum Mechanics, Princton University Press, (1960).

R3.6.8 Rose M.E., Elementary Theory of Angular Momentum, John Wiley and Sons Inc., New York, (1957).

R3.6.9 Park D., Introduction to Quantum Theory, McGraw-Hill, Inc. (1964) 203.

R3.6.10 Edmonds A.R., See R3.6.7, 57.

R3.6.11 Particle Data Group; Review of Particle Properties, Rev. Mod. Phys. 48(2) (1976) 536.

R3.7.1 Greenwood N.N. and Gibb T.C., Mossbauer Spectroscopy ., Chapman and Hall Ltd., London, (1971) 608-611,

INSTRUMENTATION AND EXPERIMENTAL PROCEDURES

S4.1 Introduction.

This chapter deals with the apparatus and procedures involved in the preparation of Mossbauer sources, fabrication of Heusler alloys, and the accumulation and computer analysis of Mossbauer spectra.

S4.2 Mossbauer source preparation.

The Mossbauer sources used during this work were, for the most part, fabricated by the commercial firm of New England Nuclear. These include ^{57}Co, $^{119}Sn^{m}$, ^{125}Sb Mossbauer sources which were used respectively in Fe, Sn, and Te measurements. However, the sources used to obtain the Au and Ir hyperfine field measurements were prepared at the Slowpoke reactor facility located in the Life Sciences Centre at Dalhousie University.

Because of the relatively low maximum neutron flux (10^{11} - 10^{12} neutrons /s) of this reactor, only relatively weak Mossbauer sources could be produced. This can be seen by observing the following equation which gives the activity of the product nuclide as a function of irradiation time

$$A = \frac{N_0 \sigma_t \phi \lambda}{\lambda + \sigma_p \phi - \sigma_t \phi} \left[\exp(-\sigma_t \phi t) - \exp(\lambda + \sigma_p \phi) t \right] \qquad \text{E4.2.1}$$

Here N_0 is the initial number of target nuclei present in the sample

and ϕ is the neutron flux in units of $s^{-1}cm^{-2}$. The neutron absorption cross. sectrons for the target and product nuclide are given by σ_t and σ_p respectively and the natural decay constant for the product nuclides is given by λ. For a thermal neutron flux of 10^{11} $cm^{-2}s^{-1}$, and typical values of σ_t and σ_p (10^{-24} cm^{-2}) and of $\lambda = 0.693/t_{1/2} \sim 10^6$ s^{-1}, where $t_{1/2}$ is the half life of the excited state of product nucleus of interest, the decay of the product and target nuclides due to absorption of neutrons can be neglected and this coefficient then turns out to be ~ 1 mCi of activity per 100 mg of target nuclei of interest. In order to achieve the maximum specific activity for the sources, the relative fraction of target nuclide in a given isotope was increased by using highly enriched isotopes >97% for irradiation.

The preparation of the ^{193}Os Mossbauer source was rather straight-forward since the Heusler alloy $Ir_{1.07}Mn_{1.07}Sn_{0.86}$ to be analysed was the absorber matrix in this measurement. However in the measurement[9] of the Au hyperfine field in the alloy PtMnSn, it was necessary to use the Heusler alloy as the Mossbauer source matrix in order to ensure that the daughter of the $^{197}Pt \rightarrow {}^{197}Au$ reaction would be at the Pt sites of the alloy.

Because of the relatively high cross section for the neutron capture by Mn atoms, the resulting large background radiation would prevent the resolution of the Mossbauer gamma rays resulting in very weak absorption lines in the Mossbauer spectra. Hence the ^{196}Pt in the form of a thin foil was first irradiated and then used to

fabricate the PtMnSn alloy.

More details about the irradiation procedures and which Mossbauer isotopes can be made using the Slowpoke facility are given by Judah [R4.2.1].

S4.3 Fabrication of Heusler Alloys.

Heusler alloys can be prepared by either sintering or melting the constituents in an inert atmosphere. The former method consists of compressing stoichiometric mixtures of finely ground powders of the constituents of the alloy into pellets and heating at temperatures below their melting points for a prolonged period of time. The chief advantage of this technique is that the evaporation of the more volatile components of the alloy is kept to a minimum. However, because the technique relies upon diffusion processes for a homogeneous ordered alloy to be formed, heating times are considerably longer than if the melting process is employed. The melting technique is the more common method employed in the fabrication of Heusler alloys. Loss of the more volatile constituents is kept to a minimum by one of two methods:

(a) Two of the more violatile components are first melted together, followed by the melting of this preliminary alloy with the third component;

(b) Rapid heating followed by short melt times. This technique was employed to make the Heusler alloys used in this work.

Several types of furnaces are used for melting the constituents but the two most common are the Argon arc furnace and the rf induction furnace. Both of these furnaces allow faster heating rates than conventional electrically heated ovens. However, the rf induction furnace offers the following advantages over the arc furnace:

(a) The eddy currents induced by the rf radiation continually stir the molten mixture providing for more homogeneous samples in one melting. The samples heated in the Argon arc furnace must be repeatedly melted with the ingot being turned over between meltings to provide the same level of homogeneity. Hence, shorter melt times are required using the rf induction furnace.

(b) By controlling the rf current in the coils, the temperature of the sample is more accurately controlled in the rf furnace, since the heat is generated in the sample directly. The thermal conduction between one of the electrodes and the sample in the arc furnace causes temperature inhomgenetics in the sample when the furnace is used and hence, temperature control is more difficult.

For these reasons, rf induction heating results in a smaller fraction of the more volatile constituents being lost due to evaporation. The rf induction furnace was used to prepare the alloys used in this work. The constituents were sealed in quartz tubes containing one atmosphere of argon (at the melting temperature) and

heated until melting occurred. After about a minute the rf current was turned off and the sample was allowed to cool.

Frequently, cooling directly from the melt does not result in fully ordered Heusler alloys. This disorder may be minimized or completely eliminated by annealing these alloys at temperature near, but below, the melting points for a day or two. This annealing also removes any stress caused by grinding the solid samples into powders for use in Mossbauer spectroscopy and X-ray diffraction.

The rate at which the samples are cooled from the annealing temperature also affects the amount of disorder. Usually rapid cooling by quenching the alloys into ice water or silicon oil produces the best ordered alloys, although this depends on the particular alloy being prepared. Exceptions are some of the $C1_b$ alloys, e.g. PtMnSn [R4.3.1], which seem to be better ordered when slowly cooled.

With these considerations in mind, the fabrication of the Heusler alloys involved the following procedures:

(a) Stoichiometric amounts of the constituents of the alloy were placed in an alumina crucible which is placed inside a quartz tube. The quartz tube is evacuated and backfilled with an inert gas (usually argon) to a pressure sufficient to produce one atmosphere at the melting point. For samples which were too small to allow the formation of induced currents of sufficient magnitude for heating, the crucible rested on a cylinder of graphite which, when heated by rf induction, melted the samples by thermal conduction.

(b) The samples were quickly heated and held in the molten state for a minute or two and were then allowed to cool or were quenched into Dow Corning 705 silicon oil.

(c) Portions of the sample were ground by hand in acetone into powder (325 mesh size) using a pestle and mortar.

(d) The powder was annealed in a quartz ampoule under an argon atmosphere using an electrically heated oven. The oven consisted of a vertical open-ended cylinder which allowed the sample to be quenched by dropping it into a container of ice water located beneath the oven. Annealing times and temperatures for each sample are given in the later chapters.

(e) X-ray diffraction results were obtained for samples both prior to and after the samples were annealed for comparison purposes. A Philips Debye-Scherrer powder camera or a Philips powder diffractometer were used for this purpose.

In some cases several samples had to be prepared before a suitable alloy was obtained.

The fabrication of the Co_2YZ alloys which were doped with enriched ^{57}Fe or ^{57}Co was a somewhat more complicated procedure. These samples were made using those undoped samples which yielded satisfactory x-ray diffraction patterns. To a solid portion of the unannealed sample was added about 0.5 to 1.0 wt% of enriched ^{57}Fe powder. The sample was remelted and the heat treatment as indicated

above was performed. Onto another portion of the undoped sample was deposited about 0.1 mCi of ^{57}Co activity dissolved in dilute HCl. This was done by despositing the solution drop by drop onto the solid piece of alloy which was supported by three thin needles. The solvent in each drop was evaporated using heat from a 150 watt incandescent light bulb. The ^{57}Co was integrated into the alloy by melting it in the rf furnace. The subsequent heat treatment, if necessary, was as described above.

S4.4 Preparation of absorber and sources for Mossbauer Spectroscopy.

According to Margulis et al [R4.4.1] and Bykov and Hien [R4.4.2] the shape of the Mossbauer absorption lines will not be Lorentzian if the thickness of the source and absorber is too great. This is due to resonant self-absorption within thick sources and saturation of the resonant gamma rays in thick absorbers. The effect is to broaden the absorption lines in the Mossbauer spectrum, thereby decreasing the resolution of the individual lines.

Resonant self absorption was not a problem in any of the sources used in this work because the number of Mossbauer nuclei in the source matrix was negligible.

To prevent saturation broadening in the absorbers the prescription used previously [R4.4.3] due to Bykov and Hien [R4.4.2] was ultilized. For the Co_2YZ alloys absorber thickness of the order of 30 mg/cm^2 give thickness broadenings of the order of 10% of the ideal Mossbauer linewidth. However for the ^{197}Au and ^{193}Ir work where

relatively weak, short-lived sources were available, larger degrees of broadening of the order of 80% were allowed in order to gain sufficiently well defined absorption lines in the Mossbauer spectra.

The ^{57}Co doped Co_2YZ sources were prepared by depositng the powdered material on wet low-temperature varnish (supplied by Oxford Instruments) on the flat surface of disk shaped aluminum source holders. The material was then covered with a few more drops of varnish and allowed to dry.

The absorbers were prepared using one of two methods:

(a) The absorber powder was compressed into the form of a disk between the thin walls of a specially designed perspex container.

(b) Absorber powder was deposited on the sticky side of several layers of 3M Scotch tape. Sufficient layers of this tape were then sandwiched together to provide an absorber of the appropriate thickness.

These absorber holders were subsequently clamped firmly to the Cu absorber mounting brackets of one of the several Mossbauer spectrometers used to accumulate the absorber spectra.

The source matrices used for these absorber experiments were either commercially manufactured ($^{57}Co/Rh$, $^{119}Sn^{m}/V$) or were prepared in the Slowpoke reactor ($^{193}Os/^{192}Os$, $^{197}Pt/^{196}Pt$). The commercial sources were securely attached to Al source holders with epoxy while

the ^{193}Os source was clamped to the source holder using a thin nylon disk.

For the source experiments, the absorbers consisted of non-magnetic metallic foils (^{57}Fe/310 stainless steel foil, ^{197}Au/Au foil) or a non-magnetic powder (^{125}Te/ZnTe). The sources used in these experiments were in powdered form which was secured to an Al source holder with low-temperature varnish manufactured by Oxford Instruments.

S4.5 Mossbauer Spectrometer.

The purpose of a Mossbauer spectrometer is to introduce, in a carefully controlled manner, a Doppler shift in the Mossbauer gamma ray energy and to record the intensity of the gamma rays transmitted through (or resonantly scattered from) the absorber (or target) as a function of the relative velocity. To first order, the energy shift in the Mossbauer gamma ray is given by E3.4.1. There are several types of Mossbauer spectrometers in use, depending upon how the relative velocity is introduced. The system used in this work was of the constant acceleration type, ie. the relative velocity was a linear function of time.

Mossbauer spectra can be obtained by either detecting the attentuation of the gamma rays due to resonant absorption or by detecting the radiation emitted upon the de-excitation of the resonantly excited nuclei. The former, which is referred to as transmission Mossbauer spectrometry, was the method used in this work.

The Mossbauer spectrometer consisted of three basic subsystems: the drive system, the nuclear detection equipment, and the data accumulation and storage system.

Two drive systems were used in this work, each consisting of two components:

(A) a linear motor consisting of a drive coil to convert the drive signal to mechanical motion and a pick up coil which created an electric signal proportional to the instaneous velocity of the motor armature,

(B) a function generator which used the pick up signal to correct the drive signal by means of a feed back loop.

One unit was manufactured by Austin Science Associates and the other by Frank Woodhams while at the University of Aberdeen, Scotland. The latter system is described in detail elsewhere [R4.4.3] and the theory behind its operation may be found in Clark et al [R4.5.1]. The Austin system is described by Judah [R4.2.1].

The purpose of the nuclear detection subsystem was to be able to detect and resolve the Mossbauer gamma rays against background radiation. It consisted of the following components: a gamma ray detector, a preamplifier, an amplifier and a single channel analyser.

The main feature of the detectors was that they were capable of resolving gamma rays of different energies. Because the detection, efficiency and energy resolution of nuclear detectors can be optimized

for restricted gamma energy ranges, several detectors were used to detect the gamma rays of the different Mossbauer isotopes used in this work. For the higher energy Mossbauer gamma rays ($E(^{197}Au)$ = 77.34 keV, $E(^{193}Ir)$ = 73.0 keV) a NaI (Tl) crystal optically coupled to a photomultipler tube (RCA8575) was used as the detector. For the lower energy Mossbauer gamma rays ($E(^{57}Fe)$ = 14.4 keV, $E(^{119}Sn)$ = 23.875 keV, $E(^{125}Te)$ = 35.48 keV) gas filled proportional counters manufactured by Reuter-Stokes Inc. (Model RG-61) were used. For ^{57}Fe work, the detector gas was a mixture of 97% Krypton 3% CO_2. While for work involving the other isotopes Xenon gas was used instead of Krypton.

The advantage of using Krypton gas instead of Xenon gas for detecting the ^{57}Fe Mossbauer radiation is that the K absorption edge for Krypton is at 14.3 keV just below the energy of the ^{57}Fe gamma ray which results in preferential absorption of Mossbauer gamma rays to background radiation slightly lower in energy. Hence Krypton gas provides for better resolution of the Mossbauer gamma rays then does Xenon gas.

The Xenon gas filled proportional counter is capable of adequately resolving the ^{121}Sb gamma ray (E =37.15keV) from the Sb K X-rays centered at 26.4 keV. However, such is not the case with the ^{119}Sn and ^{125}Te isotopes. For the ^{119}Sn Mossbauer measurements, the tin K X-ray were preferentially filtered out by a thin Pd foil whose K absorption edge (24.35 keV) was below the K X-ray energies (25.04, 25.27 keV) but above the ^{119}Sn Mossbauer gamma ray energy (23.88 keV).

This method could not be used to improve the resolution of the ^{125}Te gamma ray because its gamma ray energy (35.48 keV) exceeds the K_α (27.4 keV) and K_β (31.8 keV) tellurium X-rays. This problem was overcome by detecting the 6.0 keV escape peak which is due to the escape from the counter of the Xenon K X-rays emitted following the photoelectric absorption of the gamma rays by the Xenon gas. Further improvement in the resolution of this escape peak was obtained by using a filter consisting of Cu foil sandwiched between two layers of household Al foil. The Cu with a K absorption edge of 8.0 keV preferentially attenuated radiation immediately above this energy but did not apprerciably attenunate the gamma rays. The purpose of the Al foil with K absorption edge of 1.5 keV was to attenuate the 8.0 keV K X-rays emitted from the Cu foil.

The preamplifier, variable-gain amplifier, and single channel analyser served to create pulses whose amplitude were proportional to the energy of the radiation absorbed by the detector and to discrimate out pulses corresponding to energies other than those near the Mossbauer gamma ray energies. Details of their operation have been described elsewhere [R4.4.3].

The data accumulation and storage system consisted of either a Northern Tracor NS 600 or a Northern Tracor NS 900 multichannel analyser and has been diacussed previously [R4.4.3].

The velocity calibration of the analyser was performed by accumulating a room temperature spectrum using a source of ^{57}Fe/Cu or ^{57}Fe/Rh and an absorber consisting of foils of Fe foil and 310

stainless steel. The known difference (in velocity units) between the six absorption lines for Fe foil and the known Isomer shifts between Cu and Fe and between Rh and Fe provided information about the linearity of the drive wave form and served to assign absolute velocity units to each channel. Where possible, calibration spectra were performed both before and after each experiment to detect any changes in the system that might have occurred during data accumulation.

S4.6 Cryogenic equipment for Mossbauer spectrocopy.

For those measurements that were carried out at liquid nitrogen and liquid helium temperatures, three different cryostats were used.

The first consisted of 1.25 inch diameter cylindrical Cu cold finger which extended vertically into liquid nitrogen contained in a commercial liquid nitrogen dewar. The absorber was mounted above the nitrogen and styrofoam insulation maintained the absorber between 93 to 97 K over a twenty four hour period. The source was held at room temperature. This cryostat is pictured in F4.6.1. The picture on the left shows the cryostat with the transducer pulled back to reveal the lead shielding and collimator around the Mossbauer source while the picture on the right shows the cylindrical proportional counter and top of the Cu absorber holder contained in the styrofoam insulation. Also the aluminum disk, to which the source is mounted, is shown in the background on the end of the drive rod.

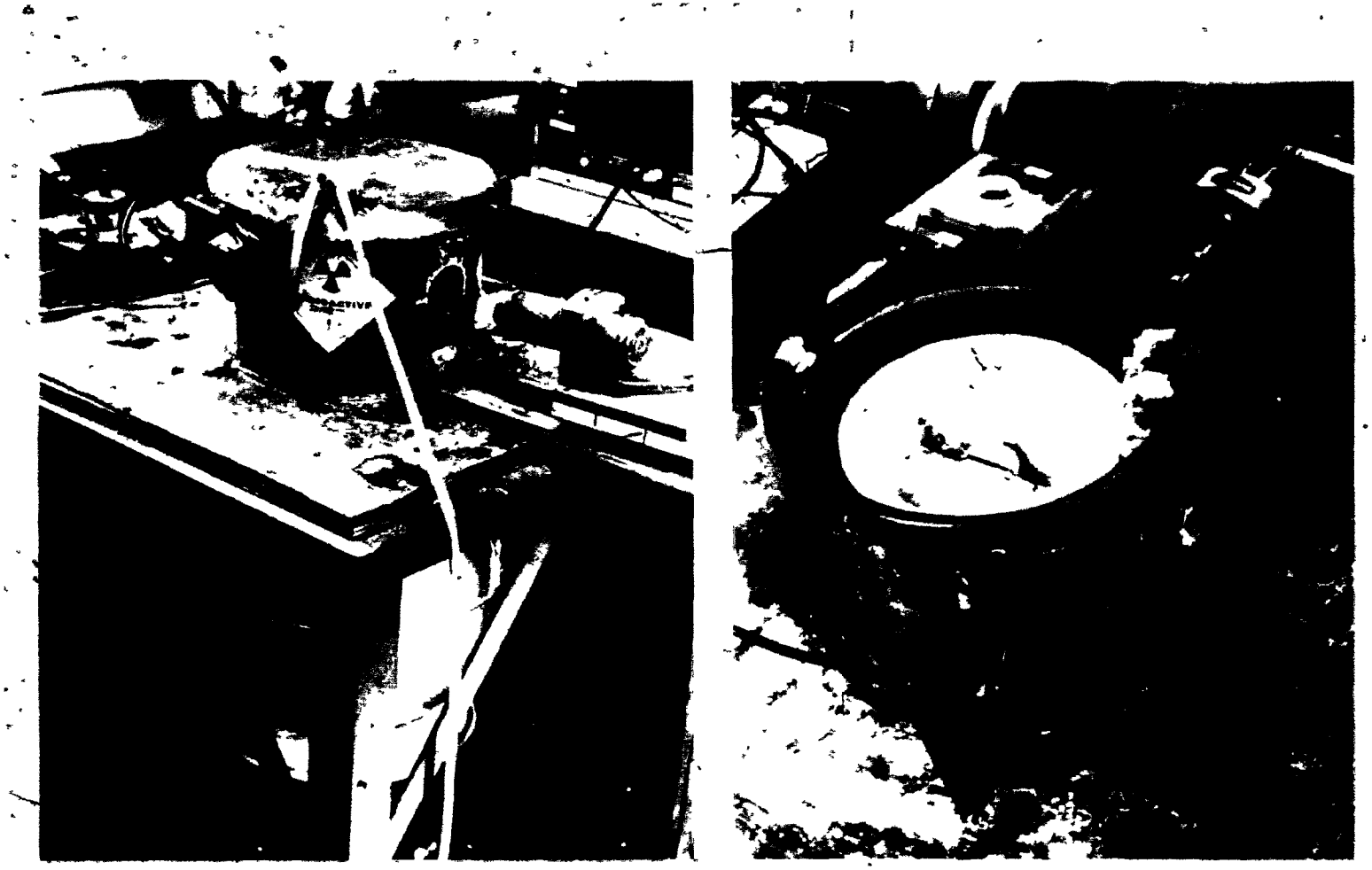

F4.5.1 Styrofoam-insulated liquid nitrogen cryostat, assembled for operation (left) and disassembled for source and absorber mounting (right).

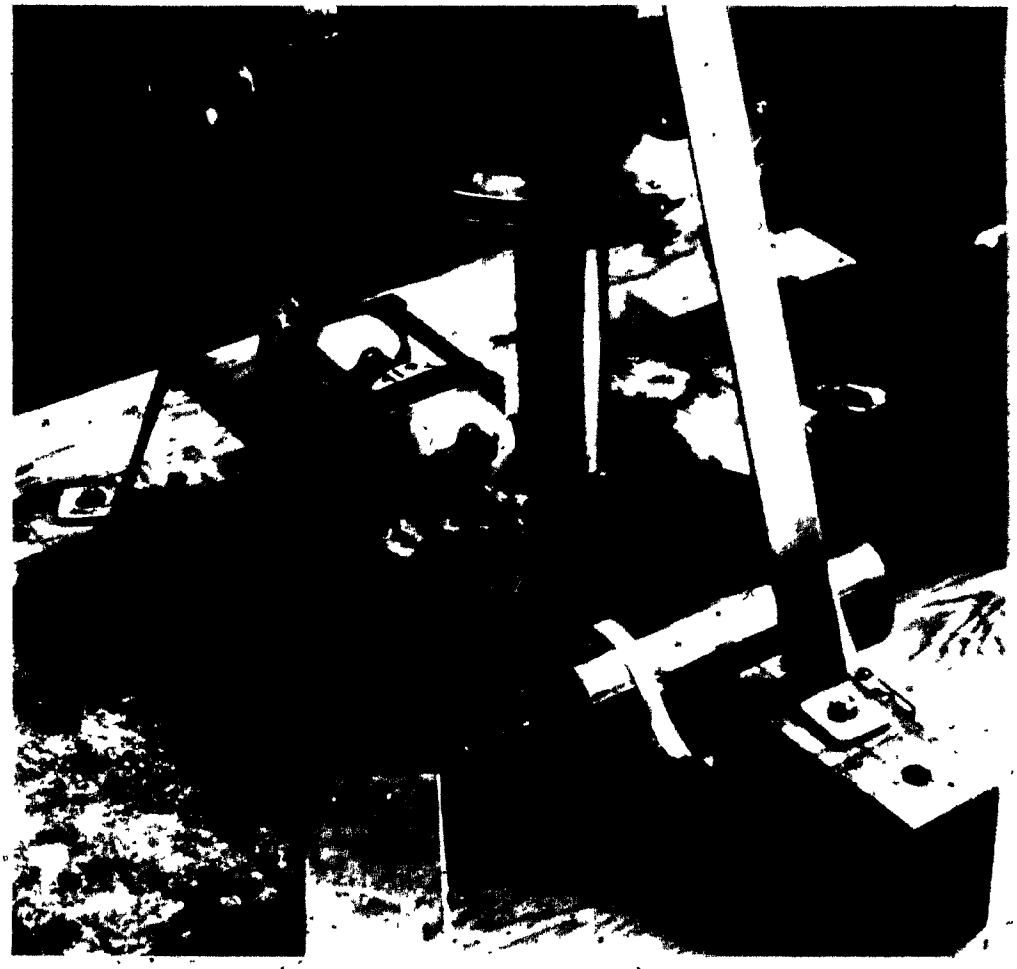

F4.6.2 The vacuum-insulated cryostat used for sign measurements at liquid nitrogen temperatures.

The second cryostat was designed by C. C. M. Campbell [R4.6.1] and consisted of an absorber holder mounted on the end of a Cu cold finger. This was suspended from the bottom of a liquid nitrogen container and the entire assembly was enclosed in a vaccuum jacket. Aluminized mylar windows on the tail piece of the vacuum jacket allowed for the transmission of gamma rays through the absorber. The thermal insulation provided by the vacuum jacket was sufficient for the liquid nitrogen to last about 8 hours or so before it required topping up. This was done with an automatic filling system built for this purpose. The cryostat was used for the measurements of the sign of the hyperfine fields because its slender tail section allowed a narrow gap between the pole pieces of the magnet and thus maximized the externally applied magnetic field. In F4.6.2 is depicted this cryostat positioned between the pole pieces of the magnet used for a sign measurements.

The third cryostat used was a commercial unit made by Oxford Instruments. This cryostat could be used with either liquid helium or liquid nitrogen. The Mossbauer source was maintained at the temperature of the cryogenic fluid while the Mossbauer absorber could be maintained anywhere from this temperature to room temperature. However, for this work the absorber was held at room temperature, liquid nitrogen and liquid helium temperatures only. A diagram of this cryostat, showing its functional components, appears in F4.6.3. The Mossbauer source was cooled by means of a phosphor bronze spring which provided a thermal link with the bottom of the liquid He vessel.

The absorber was mounted on a Cu heat exchanger below the source. The temperature of the heat exchanger was controlled by a needle value which regulated the flow of the cryogenic fluid from the liquid helium vessel and by a electrical resistance heater whose current was regulated by a feed back system. The photographs in F4.6.4 show the cryostat assembled for operation (on the left) and with the nuclear radiation shield, the outer vacuum can, and the thermal shield lowered to reveal the heat exchanger and the source holder on the end of the drive rod (on the right).

The temperature of the heat exchanger relative to the bottom of the liquid helium vessel was monitored by a Au-0.03%Fe v.s. constantan thermocouple and the absolute temperature of the absorber was monitored using a calibrated carbon resistor. A superconducting liquid helium level detector monitored the amount of helium in the cryostat.

The use of this cryostat at liquid nitrogen temperatures was straight forward. For use with liquid helium the cryostat and fixed transfer tube were precooled with liquid nitrogen. Although the system was designed to hold 15 centimeters of liquid helium usually about 35 centimeters of liquid helium was transferred to the liquid helium vessel to increase the fraction of time during which data could be accumulated. Under these conditions the cryostat could maintain the source and absorber at liquid helium temperatures for up to 18 hours.

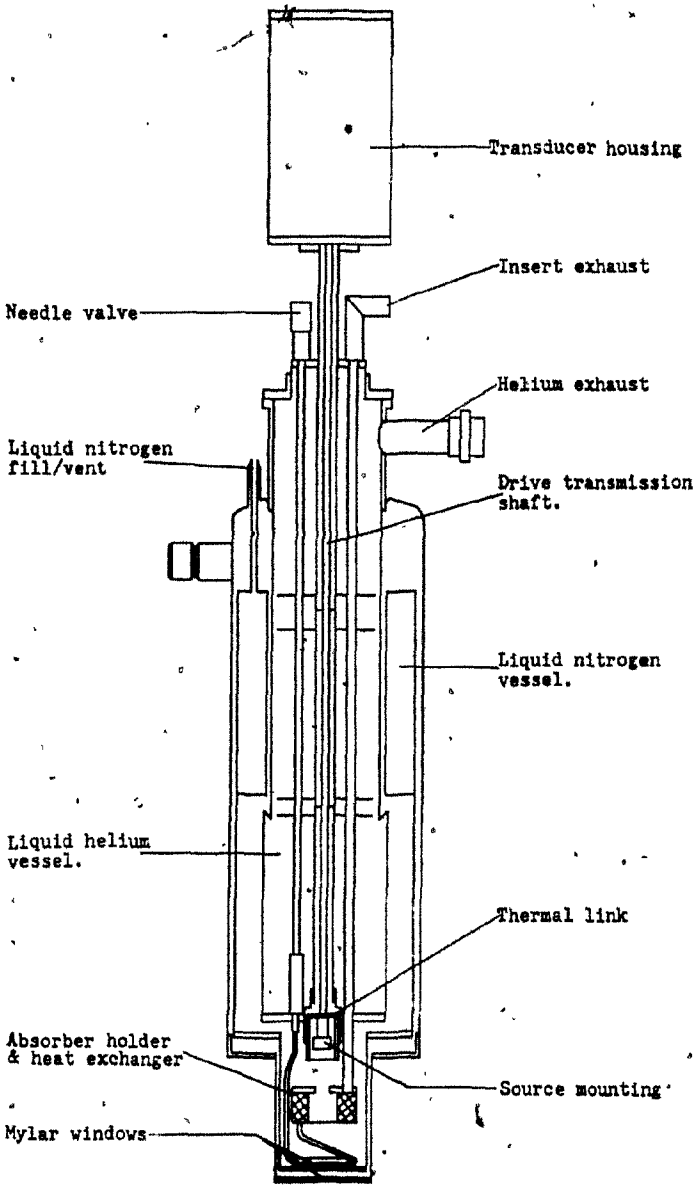

F4.6.3 Diagram of the Oxford Instruments liquid helium cryostat.

F4.6.4 Photograghs of the liquid helium cryostat showing it assembled for operation (left) and disassembled for source and absorber mounting (right).

§4.7 Computer analysis of Mossbauer spectra.

Spectra were read out of the multichannel analyser by means of teletype onto punched paper tape. This paper tape was subsequently read into the Dalhousie University CDC 6400 computer via a teletype terminal. In Spectra in which the absorption lines were relatively broad and poorly defined due to insufficient statistics (eg. ^{125}Te, ^{197}Au, ^{193}Ir) the spectra were treated in one of two ways or both:

(a) Consecutive pairs of channels were summed so as to increase the intensity of the absorption lines relative to the statistical background.

(b) The double Mossbauer spectra were folded about the mirror point by summing the channels which were mirror images of each other. The mirror image points were obtained either by fitting the unfolded spectra or by fitting the Fe foil calibration spectra.

The unfitted spectra were plotted using the line printer at the computer centre. These were used to estimate the initial estimates for the fitting parameters. The fitting program was then used to fit the spectra. The operation of this program has been previously discussed in [R4.4.3]. Using the data from the fitted calibration spectra, the hyperfine field values and isomer shifts were obtained for the spectra.

Each spectrum could be fitted with any combination of single absorption lines (singlets), two identical absorption lines (doublets), and magnetic hyperfine field absorption patterns (multiplets). Each singlet had as independent fitting parameters, the position, the area and the width of the absorption line. Each doublet possessed four independent parameters: the position of the centroid of the doublet, the separation between the two lines, and the area and the width of each line. The multiplets consisting of six absorption lines (^{57}Fe, ^{119}Sn, ^{125}Te) possessed up to seven fitting parameters. These allowed for the determination of the isomer shift (centroid of multiplet), the hyperfine field (separation of two of the lines), the quadrupole splitting (the difference between the centroid of the outer two lines and that of the inner four), the width and intensity of one line and variable intensity ratios (3:x:y:y:x:3). The multiplets for the other isotopes (^{197}Au, ^{193}Ir) were similar except the quadrupole splitting parameter was fixed at zero, and intensity ratios were not variable. This is reasonable in view of the fact that the Heusler alloys have cubic structures and should not give rise to electric field gradients. Also, since the Heusler alloys used in these measurements were in the form of polycrystalline powders, the intensity ratios were known a priori. Details of the relative intensities and relative positions of the five Mossbauer isotopes used in this work are given in §3.7.

In addition, a provision was incorporated into the program to constrain any number of fitting parameters to its initial value. This was useful when the correlation between two fitting parameters was too high to allow the fitting routine to converge on a unique pair of values. By fixing one of them (usually the one of little interest) a unique value could be obtained for the other (the one of most interest).

S4.8 References.

R4.2.1 Judah J., M.Sc thesis, Dalhousie University, (1978).

R4.3.1. Watanabe K., J. Phys. Soc. Jap. 28 (1970) 302.

R4.4.1 Margulis S., Debrunner P. and Frauenfelder H., Nuc. Inst. Meths., 21 (1963) 217.

R4.4.2 Bykov G.A. and Hein P.Z., Sov. Phys. JETP 16 (1963) 646.

R4.4.3 MacKay G.R., M.Sc. thesis, Dalhousie University, (1975).

R4.5.1 Clark P.E., Nichol A.W. and Carlow J.S., J. Sci. Instr. 44 (1967) 1001.

R4.6.1 Campbell C.C.M.,M.Sc. thesis, Dalhousie University, (1973). 44 (1967) 1004.

CHAPTER 5

THE THEORY OF HYPERFINE FIELDS IN HEUSLER ALLOYS

S5.1 Introduction.

In this chapter, the theoretical attempts to account for the observed hyperfine fields measured at nuclei located in crystalline solids are presented. In S5.2 the mechanisms by which electrons in the vicinity of a nucleus give rise to magnetic fields at the nuclear site are discussed. The polarization of the conduction electrons in metals is discussed in S5.3. In the next three sections current theoretical models of the contribution of polarized conduction electrons to the hyperfine fields at non-magnetic atoms are discussed. In the final section, the present status of the theory of hyperfine fields at magnetic atoms is briefly discussed.

S5.2 Origins of Hyperfine Magnetic Fields at Nuclear Sites.

The magnetic dipole part of the interaction between the magnetic moment of a nucleus μ_I and an electron can be written as [R5.2.1, R5.2.2]:

$$\mathcal{H} = 2\frac{\vec{\mu}_I \cdot \vec{L}}{r^3} - 2\mu_B\left[\frac{\vec{\mu}_I \cdot \vec{S}}{r^3} - 3\frac{(\vec{S}\cdot\vec{r})(\vec{\mu}_I\cdot\vec{r})}{r^5}\right] + \frac{16}{3}\mu_B\vec{\mu}_I\cdot\vec{S}\,\delta(\vec{r}) \qquad \text{E5.2.1}$$

where $\vec{L}$ and $\vec{S}$ are the orbital angular momentum and spin of the electron, μ_B the Bohr magneton and $\vec{r}$ the position vector of the electron with respect to the nucleus.

By comparing this equation to the interaction of μ_I with a local magnetic field, $\vec{H}$

$$\Delta E = -\vec{\mu}_I \cdot \vec{H} \qquad \text{E5.2.2}$$

we obtain the effective hyperfine field due to one electron

$$\vec{H} = -\frac{2\vec{L}}{r^3} + 2\mu_B\left[\frac{\vec{S}}{r^3} - 3\frac{(\vec{S}\cdot\vec{r})\vec{r}}{r^5}\right] - \frac{16}{3}\mu_B\vec{S}\,\delta(\vec{r}) \qquad \text{E5.2.3}$$

Summing over all electrons in the vicinity of the nucleus we obtain

$$\vec{H} = -2\mu_B\langle L\rangle\langle 1/r^3\rangle + 2\mu_B\langle\vec{S}/r^3 - 3\vec{r}(\vec{S}\cdot\vec{r})/r^5\rangle - 16\tfrac{\pi}{3}\mu_B\langle\Sigma(S_\uparrow - S_\downarrow)\rangle \qquad \text{E5.2.4}$$

where $\vec{L}$ and $\vec{S}$ are the total angular momentum and spin of the electrons of the parent atom of the nucleus, and $S_\uparrow$ and $S_\downarrow$ are the densities of the spin up and spin down electrons at the nucleus.

The first term, which is due to the orbital moment of the atom, is always positive. It is frequently negligible because of angular momentum quenching at atomic sites located in an environment with non-cubic symmetry. Even for cubic environments a Jahn-Teller distortion may cause a complete quenching of the angular momentum. The only reported evidence of significant contributions from unquenched orbital moments in these alloys is for Co sites in Co_2YZ, (Y≠Mn) [R5.2.3]. At these sites the hyperfine fields are expected to

be negative. However, small positive fields of about 1 or 2 T have been observed.

The second term is the contribution due to the dipole field of the total spin S on the atom. In a cubic metal, in the absence of spin-orbit coupling, this contribution vanishes [R.5.2.1, R5.2.4]. Thus, in Heusler alloys the contribution to the hyperfine field at the nucleus due to the spin of the parent atom can be neglected.

It is the third term which is thought to be predominately responsible for the hyperfine fields measured at nuclear sites in Heusler alloys. This is referred to as the Fermi contact interaction and it is the interaction between the nuclear moment and the spin polarization of the electrons contained within the nuclear volume. Since only s electrons have non-vanishing probability of being located within the nuclear volume, only s electron spin polarization contributes directly to the hyperfine field.

While electrons with non-zero angular momentum do not contribute directly to the Fermi contact interaction, unpaired d (or f electrons) in transition (or rare earth) metals can, via an sd Coulomb exchange interaction, cause the s electron wave functions to become spin dependent. The spin up (down) wave functions are pushed toward (pulled away from) the nucleus increasing (decreasing) the spin up (down) electron density at the nucleus. This so called core polarization of s electrons gives rise to a negative field at transition metal nuclei relative to the magnetic field due to the atomic moment. This field is typically of the order of 20 to 70 T.

In metals a further contribution to the contact term may arise from polarized s-like conduction electrons. In this situation either a positive or negative contribution to the hyperfine field at the nucleus is obtained depending on the local polarization of the conduction electrons. If the conduction electron polarization (CEP) is due to magnetic moments on neighbouring atoms, this contribution is usually referred to as a tranferred hyperfine field. In this manner, hyperfine fields may exist at the nuclear sites of atoms not possessing local atomic moments.

Thus, the measurement of transferred hyperfine fields at non-magnetic atomic sites gives information about the CEP in metals and provides crucial tests for the various theories which attribute magnetic ordering in metals to CEP. This is, in part, relevant to the Heusler alloys X_2MnZ, and XMnZ (X≠Co) where the Mn moments are second nearest neighbours and are thought to be too widely separated for the direct interaction due to the overlapping 3d orbitals of neighbouring Mn atoms to be strong enough to cause ferromagnetic alignment. For this reason, various theories involving the exchange interaction between the localized d electron of Mn atoms and s-like conduction electrons were developed.

S5.3 Polarization of the Conduction Electron Band.

These theories rely on the effects of the screening of the ionic positive charge of impurity ion by conduction electrons to preserve charge neutrality within the metal. While the ionic charge is typically screened in the order of ~atomic distances, long range sinusoidal oscillations in the conduction electron density relative to that of a pure metal are produced. The asymtotic expression for these oscillations for distances large compared to atomic dimensions is given by [R5.3.1]:

$$\delta n(r) \approx \frac{-\alpha}{2\pi r^3} \cos(2k_F r + \varphi) \qquad \text{E5.3.1}$$

where

$$\alpha \sin\varphi = \sum_{\ell}(-1)^{\ell}(2\ell+1)\sin^2[\eta_\ell(k_F)] \qquad \text{E5.3.2}$$

and

$$\alpha \cos\varphi = -\sum_{\ell}(-1)^{\ell}(2\ell+1)\sin[\eta_\ell(k_F)]\cos[\eta_\ell(k_F)] \qquad \text{E5.3.3}$$

Here k_F is the free electron Fermi wave vector for the conduction electrons, φ is the total phase shift of the scattered electrons, and $\eta_\ell(k_F)$ are the phase shift of the partial waves of angular momentum ℓ. The interaction strength is proportional to α.

If the impurity atom possesses a magnetic moment, then the unequal spin up and spin down localized d electron densities give rise to different phase shifts for the spin up and spin down conduction electrons. This results in a shift in the spin up oscillations relative to the spin down oscillations and gives rise to a net CEP which is the difference between two expressions of the form of E4.3.1. This spin polarization is also sinusoidal and has an amplitude which is proportional to the inverse cube of the radial distance from the magnetic ion in the asymtotic limit of large distances.

The two earliest models of CEP to be used for predicting hyperfine field values in Heusler alloys were based on the work of Ruderman and Kittel [R5.3.2], Kasuya [R5.3.3], and Yosida [R5.3.4] (RKKY) and of Caroli and Blandin [R5.3.5] (CB). They differ in the manner in which the magnetic moment is formed on the Mn impurity ion. In the former, the 3d electrons are considered to occupy bound states on the Mn ion and the spin polarization is due to a Coulomb exchange interaction between these localized 3d electrons and the conduction electrons. In the case of the CB theory, the Mn moment is due to the 3d electrons occupying virtual bound states or equivalently to d-wave resonance scattering of conduction electrons. In the asymtotic limit at large r, both theories predict that the CEP is a sinusoidal function of $k_F r$ with radial amplitude with $1/r^3$ dependence. The hyperfine fields are assumed to be primarily due to the Fermi contact interaction between these polarized conduction electrons and the nuclear magnetic moment. The resulting asymtotic expressions for the

electron polarization induced by one Mn atom at a distance r from the Mn atom are given by:

$$\delta n(r) = -J(0)\, S_n \frac{6\pi (3n)^2}{V E_F N} \frac{\cos(2k_F r)}{(2k_F r)^3} \qquad \text{E5.3.4}$$

for the RKKY theory and

$$\delta n(r) = \frac{10 k_F^3}{\pi^2} \sin(\eta_\downarrow) \frac{\cos(2k_F r + \eta_\downarrow)}{(2k_F r)^3} \qquad \text{E5.3.5}$$

for the CB theory.

In these expressions, V and N are the total volume and number of lattice sites in the sample, $2n = n_\downarrow + n_\uparrow$ is the total number of conduction electrons, J(0) is the value of the s-d exchange integral assumed to be constant, $\eta_\uparrow$ and $\eta_\downarrow$ are, respectively, the phase shifts for the scattering of spin up and spin down electrons at Mn ions and r is the radial distance between the Mn moment and the point at which the polarization is determined.

In both theories, the sign of the CEP depends on the argument of the cosine function and the sign of J(0) or the magnitude of n. In Heusler alloys not containing Co, the local moments on the Mn ions all tend to be very close to 4 μ_B. The value of n and J(0) which is determined primarily by the magnitude of this moment are not expected to change from one Heusler alloy to another by a large amount. Furthermore, the lattice parameter, which is again relatively constant

from one alloy to another (6.0Å), only indirectly affects these values through the dependence of k_F on a. Hence, the sign of the field depends primarily on $k_F r$. This quantity is independent of the lattice parameter for a given nearest neighbour distance in isostructural alloys. Thus, these theories essentially predict that the sign of the hyperfine field measured at a particular site in a Heusler alloy does not change from one alloy to the next. In particular, if several impurity sp elements are substituted for the Z atom in the same Heusler host matrix, the hyperfine fields measured at these sites would, according to these theories, all have the same value. However, experimental evidence shows that the hyperfine field measured at different impurities in transition ferromagnetic hosts depends predominately on the impurity atom (See Rao [R5.3.6] for a summary of the hyperfine fields measured in transition metals). Similar trends were also shown to exist when the sp impurities Sn and Sb were substituted in Heusler alloys (Campbell and Leiper, [R5.3.7], and Swartzendruber and Evans [R5.3.8]). The fields at the Z-sites in Heusler alloys were found to change from negative to positive as a function of the "valance" of the impurity for the 5sp series, this sign change occuring near Sn.

S5.4 The Daniel-Friedel Model.

Clearly, if these models of CEP are correct, then the localized electrons on the impurity atom must strongly perturb the CEP at the atomic site. The Daniel-Friedel (DF) model (Daniel and Friedel [R5.4.1]) is a model which examines the screening of the excess ionic charge on a non-magnetic impurity by means of a polarized conduction band. The model was proposed to account for the trends of hyperfine fields measured at non-magnetic, sp impurities in concentrated ferromagnetic transition metals such as Fe. Here the hyperfine field is negative for the Ag impurity and approaches zero as the atomic number of the 5sp impurity increases becoming positive for Sb and reaching a maximum positive value for the I impurity, then finally decreasing toward zero again for the Xe impurity.

According to the model, the presence of ferromagnetic order creates two distinct polarization states for the conduction electrons, one with electron spins parallel to the spin on the magnetic ions denoted by ↑ and the other with the spins anti-parallel and denoted by ↓. An sd Coulomb exchange interaction between localized 3d spins on Fe atoms and the conduction band manifests itself as a uniform positive spin polarization of the conduction band. The conduction band is viewed as two free electron sub-bands of opposite polarizations with energies given by:

$$E(k,\uparrow) = \frac{\hbar^2 k^2}{2m} \mp \epsilon \qquad \text{E5.4.1}$$

where the + and - signs refer to the spin ↑ and spin ↓ sub-bands. Hence, the splitting between the sub-bands is 2ϵ. The spin polarization per unit volume is given by:

$$\delta_n = \frac{\sqrt{m}\,k_F}{\pi^2\hbar}\,\epsilon \qquad \text{E5.4.2}$$

When a non-magnetic impurity is substituted for one of the magnetic ions, it is represented by a spherically symmetric square well whose depth is determined by the amount of ionic charge, ΔZ, which must be screened relative to that of the host ions. Because there is no magnetic moment on the ion the s-d exchange interaction is suppressed within the atomic shell of the impurity. This is taken into account by making the well depth spin dependent so that the well is the same depth below the Fermi energy for both polarization states. The depth may be represented by:

$$V(\updownarrow) = V(\Delta Z) \mp \epsilon \qquad \text{E5.4.3}$$

where $V(\Delta Z)$ is the well depth in the absence of a polarized conduction band. The radius, r_0, of the well is taken to be the Wigner-Seitz radius of the impurity in its elemental matrix. The potential well

is, therefore, less attractive for the more numerous spin ↑ electrons than for the spin ↓ electrons.

Two limiting cases illustrate the physical processes involved in this model:

(a) When the valence of the impurity is the same as the magnetic ions, then $V \to 0$ and the difference in the depth of the two potential wells 2ϵ becomes dominant. Thus, the majority spin carriers are preferentially repelled giving rise to a local CEP opposite to that of the background CEP in the matrix.

(b) On the other hand, as ΔZ becomes larger, the scattering well depth becomes increasingly less dependent upon the electron spin and, if the conduction electron density remains small enough, the local CEP becomes parallel to the background CEP.

Thus, it is possible for the sign of the hyperfine field to become valence dependent. The local CEP is given as a sum of two contributions, one due to the positive background CEP and a negative CEP due to bound s electrons resulting from charge screening. Each of these terms is of the form:

$$\delta n(o) = -2\frac{n\epsilon}{\pi t}\frac{\partial \delta_i(o)}{\partial(V)} \qquad \text{E5.4.4}$$

$$\rho_{bg}(0) = \frac{3a^3}{5\pi}\left|u(0)\right|^2 \int_0^{k_F} \frac{k'^2 dk}{1-(k_o^2/k'^2)\sin(k'a)} \qquad \text{E5.4.5}$$

and

$$\rho_{sc}(0) = \frac{2}{5}\left|u(0)\right|^2 \frac{(\mu a)^2}{1-[\tan(\mu a)]/\mu a} \qquad \text{E5.4.6}$$

Here, u(r) is normalized to a sphere of radius a, the binding energy is $h^2\lambda^2/2m$, and the well depth, V, in the absence of CEP is $h^2k_o^2/2m$. These quantities are further related by: $k'^2 = k_o^2 + k^2$, $\lambda^2 + \mu^2 = k_o^2$ and $\lambda a = -\mu a/\tan(\mu a)$. Using this model, Daniel and Friedel were able to account for the observed trends in the 5sp impurity hyperfine fields in an Fe host.

One important criticism of the DF model is that a positive CEP was assumed in order to account for these trends. This is contrary to the fact that a negative CEP is necessary in order to explain the observed resistivity minima when transition metal impurities are substituted into ferromagnetic hosts. Campbell [R5.4.2] has shown, however, that the assumption of a positive CEP is not necessary in this model in order to predict the observed trends in hyperfine fields. He suggests that a negative CEP due to virtual d-resonance states on the Fe atoms can lead, using the DF model, to better predictions if smaller contributions to the conduction band from Fe atoms are assumed.

§5.5 The Blandin-Campbell Model.

To account for the observed strong dependence of hyperfine fields on the local properties of the probe atom, Blandin and Campbell [R5.5.1] considered an electron gas into which was placed two impurity atoms, one with and the other without a localized magnetic moment. A s-d exchange interaction between the magnetic atom and the electrons, induces a spin polarization in the electrons of the RKKY type. Since the spin polarization is only required to be known at a specific point (ie. at the nucleus of the non-magnetic atom), the effective potential which produces this spin polarization is represented by a potential which is spherically symmetric about the impurity atom and has a radial dependence given by a delta function located at R_0, the separation distance between the atoms. The total potential at the non-magnetic ion is thus given by:

$$V(r) = V_0 - \tfrac{1}{2}\sigma\epsilon\delta(r-R_0) \qquad \text{E5.5.1}$$

where $V_0(r)$ is the spherical symmetric square well potential of radius R_0 and depth V_0 describing the unshielded excess positive charge at the non-magnetic impurity atom. The spin dependent part of the total potential is contained in the second term where $\sigma = +1\ (-1)$ denotes $\uparrow\ (\downarrow)$ spin states and 2ϵ is a measure of the energy separation between the two spin states in the absence of the ionic potential.

For situations where ϵ is small, the total spin density at the nucleus of the non-magnetic ion will be given exactly by:

$$\delta n_{R_o}(0) = \frac{4\epsilon}{\pi}\int_0^{k_F} |\psi_k(0)|^2 \sin(2kR_o + 2\delta_o)\, k\,dk \qquad \text{E5.5.2}$$

where $\psi_k(0)$ is the wave function for the s component of the scattered waves with wave vector k. In leading powers of R_o^{-1}, the asymtotic expression for $\delta n_{R_o}(0)$ is given by:

$$\delta n_{R_o}(0) = -\frac{k_F}{2\pi^2} J\Omega_o \langle S_z\rangle |\psi_{k_F}(0)|^2 \frac{\cos(2k_F R_o + 2\delta_o^F)}{R_o^3} \qquad \text{E5.5.3}$$

In this expression, valid for R_o large compared to r_0, J is the value of the s-d exchange integral, Ω_o is the atomic volume of the magnetic ion, $\langle S_Z\rangle$ is the average value of the spin on the magnetic atom and is the phase shift in the s-component of the scattered wave.

The hyperfine field at non-magnetic ion is assumed to be due to the Fermi contact interaction only and is calculated by summing the contributions of the CEP from the nearby magnetic ions. The hyperfine field is then given by:

$$H_{eff} = \tfrac{8}{3}\pi N_0 \sum_i \delta n_{R_{oi}}(0) \qquad \text{E5.5.4}$$

Using the fact that the Knight shift for the same non-magnetic impurity in a non-magnetic, but otherwise similar, host is given by:

$$K = \tfrac{8}{3}\pi\mu_B^2(4k_F/\pi)|\psi_{k_F}(0)|^2 \qquad \text{E5.5.5}$$

the hyperfine field may be written as

$$H_{eff} = -\frac{Jn_0K}{8\pi\mu_B}\sum_i\langle S_z(R_{0i})\rangle\frac{\cos(2k_FR_{0i}+2\delta_0^F)}{(R_{0i})^3} \qquad \text{E5.5.6}$$

When $V_0 = 0$, which implies that $\delta_0 = 0$, this expression is identical that of the RKKY theory.

In practice, this expression is applied by assuming the conduction band is adequately described by the free electron theory, in which case:

$$k_F = (3\pi^2n)^{1/3} = (3N_c\pi^2n_0)^{1/3}/a \qquad \text{E5.5.7}$$

Here n is the number of conduction electrons per unit volume, N_c the number of atoms per unit cell of the structure of the host (12 for $C1_b$ and 16 for $L2_1$ structures), a is the lattice parameter, and n_0 is the average number of electrons donated to the conduction band per atom.

The s-phase shift δ_0 is determined by requiring the excess ionic charge on the non-magnetic ion to be completely screened within the atomic volume in which case the Friedel Sum rule [R5.5.2] is satisfied:

$$Z_{eff} = \frac{2}{\pi}\sum_{l}(2l+1)\delta_l \qquad E5.5.8$$

For an sp conduction band where δ_1 is assumed to be equal to δ_0 this gives:

$$2\delta_0 = Z_{eff}\pi/4 \qquad E5.5.9$$

Z_{eff} is the effective charge of the impurity atom and is given in terms of the valence state of the sp impurity Z_v and N_0 by:

$$Z_{eff} = Z_v - n_o \qquad E5.5.10$$

It is the uncertainty in determining n_0 that makes the application of this theory difficult. Blandin and Campbell [R5.5.1] originally employed the model to predict the hyperfine fields measured at 5sp impurity atoms substituted for the In atom the Heusler alloy Cu_2MnIn by assuming Cu and Mn each contributed one electron while the In atom contributed 3 electrons to the conduction band. This results in a constant k_F value of $2.8/a^{-1}$ with the hyperfine field depending only on Z_{eff} and K. The resulting predictions agreed with the observed trends in the hyperfine field values although numerical agreement was poor.

The major difficulty in choosing n_0 arises when one attempts to determine hyperfine fields at Z atoms for different Heusler alloy hosts. In this case the hyperfine fields systematics now depend on k_F and 2δ through this dependence on the value of n_0. Thus, the choice of n_0 becomes critical. The conventional approach is to assume that noble metals contribute 1 electron/atom, the sp impurities contribute Z electrons/atom. For magnetic ions the contribution to the conduction band n_0 is determined from the number of outer electrons on the free atom after allowing for the magnetic moment on the ion in the Heusler alloy (Caroli and Blandin [R5.3.3], Blandin and Campbell [R5.5.1]). If $n_\uparrow$ and $n_\downarrow$ are the numbers of bound 3d electrons of spin up and spin down respectively, then:

$$n_\uparrow - n_\downarrow = \mu/\mu_B \qquad \text{E5.5.11}$$

and

$$n_\uparrow + n_\downarrow + n_c = \begin{cases} 7 \text{ for Mn} \\ 9 \text{ for Co} \end{cases} \qquad \text{E5.5.12}$$

If, for the Mn atoms one assumes that the number of bound spin up electrons is 4.5 electrons this gives about 2 electrons per atom for Mn in X_2MnZ (X≠Co) alloys and 1.0 to 1.5 electrons per atom in Co_2MnZ alloys. For Co atoms, if one assumes $n_\uparrow = 4.7$, then 0.1 to 0.6 electrons per Co atom in the Co_2MnZ alloys and -0.1 to -0.3 electrons per Co atom in Co_2YZ (Y≠Mn) alloys are contributed to the conduction

band.

Problems are encountered when trying to estimate the contributions of Ni and Pd atoms to the conduction band. Generally, it has been found that Ni and Pd must make only small contribution (about 0.1 electrons). Mayo and Dunlap [R5.5.3] found it necessary to use this low value if the change in sign of H_Z(Sn) was to be obtained in the solid series of $(Ni_xPd_{1-x})_2MnSn$ alloys. The results are consistent with those of Price et al [R5.5.4] where the values of H_Z(Sb) in the $Ni_{1+x}MnSb$ alloys are essentially independent of x. However, such is not the case of the $Pd_{1+x}MnSb$ alloys [R5.5.4, R5.3.6], where the Sb Mossbauer spectra indicate one hyperfine field for low x values but two hyperfine fields for higher x values. This suggests that a free electron model of the conduction band is not applicable to the Pd based Heusler alloys.

These values of n were used by Dunlap and Jones [R5.5.5] to estimate hyperfine fields at Sn sites in the $Co_2MnZ_{0.98}Sn_{0.02}$, (Z=Al,Ge,Si,Ge,Sn). The assumption of constant n values for these alloys implicity assumes that the Fermi level at the magnetic ions is reflected only by the variation in the magnetic moments from one alloy host to another. This implies that there exists some correlation between the magnetic moments on Mn ions in X_2MnZ and the free atom valence states of the Z atoms, particularly if the 3d spin ↑ and spin ↓ orbitals on the Mn atoms are completely separated.

There appears to be no such correlation for the Heusler alloys in general. For example, in the alloys Pd_2MnZ (Z=In,Sn,Sb) the moments are 4.3, 4.23, and 4.4 μ_B respectively. Since Ni has the same electronic configuration as Pd, one would expect a similar trend for Ni_2MnZ alloys. However, for the isostructural Ni_2MnZ alloys, the moments decrease with increasing valence of the Z atom. Thus, it would appear that this rigid band model does not apply to the Heusler alloys in general. In view of this, detailed band structure calculations are necessary for the Heusler alloys in order to determine the contribution of each atom to the conduction band. Only recently have such calculations been performed and then for only six Heusler alloys, namely Co_2MnSn, Co_2TiSn, Co_2TiAl, Cu_2MnAl, Ni_2MnSn and Pd_2MnSn [R5.5.6]. However, no theoretical model of hyperfine fields in Heusler alloys has yet made use of these calculations. Hence, the empirical methods of obtaining the contributions to the conduction band will be employed here.

In addition to the difficulty in choosing reasonable n_0 values, there are several other shortcomings of this theory (Jena and Geldart [R5.5.7]):

(a) If experimental values for n_0 were available they would have to be very accurately known because the value of the hyperfine fields is determined by a periodic function of n_0 which leads to increasingly larger uncertainties in the contributions from the more distant magnetic moments.

(b) The scattering of conduction electrons from the magnetic ions is assumed to be completely incoherent since the contributions from the CEP due to individual atomic moments are summed independently. It is not clear that this is valid (See Daniel [R5.5.8]).

(c) Only the scattering of the s-like components of the conduction band is considered in the formation of CEP. Although only s-electron wave functions have a finite probability of existing at nuclear sites, and hence, can influence the hyperfine field, they then be indirectly perturbed by polarized electrons of higher character. Hence, the scattering of these partial waves should not be ignored.

(d) In practice only the moments on first, second, and third necan best neighbours can be considered in determining the total CEP (because of the problems given in the first criticism) even though the weak $1/R^3$ dependence does not result in rapid convergence of E5.5.6.

(e) Finally, the expression E5.5.6 is only an asymtotic expression valid for separation distances between the impurity atoms much larger than atomic dimensions. Since the Mn and Z atoms are only second near neighbours in Heusler alloys, this condition is not satisfactorily fulfilled.

The last condition has been remedied by including an phenominological adjustment of $\pi/2$ in the phase of the argument of the cosine function for first and second neighbour distances (Campbell and Blandin [R5.5.9]). This has been done following the more detailed calculation of the CEP around a magnetic impurity in a non-magnetic metallic host matrix by Jena and Geldart [R5.5.10] and Allout [R5.5.11]. In this work they suggest that this preasymtotic correction should be inversely proportional to $k_F r$. Using this in the BC theory then gives for the CEP at nuclear sites:

$$\delta_n(0) \propto \sum_i \mu_i \frac{N_i}{r_i^3} \cos(2k_F r + 2\delta_0 + C/k_F r) \qquad \text{E5.5.13}$$

where C is usually chosen so that $C/k_F r = \pi/2$ for the second nearest neighbour distances r in the Heusler alloys (Campbell and Blandin [R5.5.9]). This is the form of the BC theory as it is currently applied to the study of hyperfine fields at non-magnetic sites in Heusler alloys.

In spite of the shortcomings of this theory, it has two advantages over other theories:

(a) The spatial oscillatory CEP is explicitly determined from the scattering of conduction electrons from both the magnetic ions and the charge screened non-magnetic ions. Thus, information about the spatial dependence of the effective CEP at various sites in Heusler alloys can be obtained by substituting the same

impurity in different sites in the same alloy.

(b) The resulting uncomplicated expressions provides a simple physical interpretation of the empirical trends found to exist in the Heusler alloys.

S5.6 The Jena-Geldart Model.

The Jena Geldart (JG) theory is a refined version of the DF theory which was developed explicitly for the purpose of explaining the hyperfine field at non-magnetic ions in Heusler alloys (Jena and Geldart [R5.6.1]) In principle the two models are identical. They differ only in the manner in which the wave functions for the conduction electrons at the nuclear site are calculated. In the DF theory plane waves were used while in the JG theory the Bloch wave functions were determined by orthogonalizing them to the localized atomic wave functions. This was done to correctly reproduce the highly local character of the valence electrons at the nuclear site which is neglected by the use of a square well potential.

Also in computing the appropriate well depth V_0, the phase shifts for the $\ell = 0,1,\ldots 7$ partial waves were included in order to satisfy the Friedel sum rule (E5.5.8) in contrast to the DF and BC models where only the $\ell = 0$ and the $\ell = 0,1$ partial waves were employed, respectively. Thus, in the JG theory an attempt is made to allow for the indirect contribution to the hyperfine fields due to spin

dependent scattering of conduction electrons not of sp character. In the spirit of the DF model the hyperfine field at the nucleus is then determined from the local CEP via the Fermi contact interaction:

$$H_{eff} = -\frac{8\pi}{3}\mu_B \alpha^2(k_F)\,\delta n(0) \qquad \text{E5.6.1}$$

Here $\delta n(0)$ is the local CEP as calculated by the DF model and depends on Δ/E_F, the splitting of the conduction band relative to the Fermi energy in the absence of splitting, and the value of $k_F r_0$, where r_0 is the Wigner-Seitz radius of the impurity potential well. The Bloch enhancement factor $\alpha^2(k_F)$ is the above mentioned correction to the square well potential and depends upon the Fermi wave number k_F as well as on the atomic number of the impurity atom. Values of $\delta n(0)/k_F^3$ are plotted by Jena and Geldart [R5.6.2] as a function of the valence of the impurity atom for various values of k_F assuming $\Delta/E_F = 0.001$ Values of $\alpha^2(k_F)$ are plotted in Jena and Geldart [R5.6.3] as a function of k_F for different impurity atoms and as a function of the impurity atom with $k_F = 0.62\ a_0^{-1}$. These parameters are obtained by estimating k_F from the average number of conduction electrons using the free electron model as for the BC theory. The value of the Wigner-Seitz radius r_0 is determined for the impurity ion in its pure state. The potential well depth is fixed by the relative valence of the impurity relative to the average number of conduction electrons per atom. Suitable values for Δ/E_F are obtained by fitting this value to in an experimental field value (for Sb in PdMnSb) and

then scaling this value in proportion to the magnetic moment per molecule in other Heusler hosts. In this manner hyperfine field values at the 5sp impurity atoms for several hosts XMnZ and X_2MnZ (X≠Co) have been calculated by these workers [R5.6.3].

From a theoretical point of view, this theory is superior to the BC theory because it is specifically devised for a concentrated ferromagnetic host into which non-magnetic impurities have been substituted. Thus, effects of coherent scattering from individual magnetic moments and the various exchange interactions are explicitly taken into account by means of the empirically determined splitting parameter Δ/E_F. Also, this theory allows the use of more realistic impurity potentials in order to calculate the hyperfine fields. A major disadvantage of the theory is that there is no explicit dependence on the distance between the probe atoms and the magnetic host atoms. Such a spatial dependence has been found in isostructural Heusler alloys differing only in lattice parameters (Delyagin et al [R5.6.4] and Mayo and Dunlap [R5.5.3]). Also the problems associated with the determination of suitable values for k_F and Z_{eff} plague this theory for the same reasons as they do the BC theory.

S5.7 Stearns' Volume Misfit Model.

This model was originally devised to account for the trends observed in the hyperfine fields at dilute non-magnetic impurities in Fe, Co, and Ni [R5.7.1]. However, she has recently employed it to explain the hyperfine fields observed at Z impurity atoms in Heusler alloys. (Norbeck and Stearns [R5.7.2]).

This model in contrast to the previous models discussed assumes that the impurity atom has little affect on the CEP for electrons of s character (s-CEP). The major advantage of this assumption is that the contribution to the hyperfine field measured on non-magnetic sites in ferromagnetic hosts can then be considered to be a sum of two independent contributions; one due to the s-CEP in the host matrix and the other due to the local properties of the impurity ion. That is:

$$H(Z) = H_h(Z) + H_i(Z) \qquad E5.7.1$$

Where $H_h(Z)$ is the incoherent sum of the s-CEP contributions to the field at probe atoms due to the surrounding magnetic moments and $H_i(Z)$ is due to the interaction between the host electrons and the impurity atom.

In practice $H_h(Z)$ is calculated by assuming that s-like conduction electrons adopt the character of local s-like valence electrons when in the vicinity of a particular nucleus and hence, the ratio of $H_h(Z)$ to the hyperfine coupling constant A is constant for different impurities at the same site in a given host and is given by:

$$H_h(Z) = H_h(Z')\frac{A_Z}{A_{Z'}} \qquad \text{E5.7.2}$$

Implicit in this assumption is that the sp atoms all contribute about the same number of electrons to the conduction band as do the X and Y atoms, i.e. approximately one electron per atom.

The value of $H_i(Z)$ is considered to be due to the overlap between the 3d electrons of the host atoms and the inner closed s orbitals of the impurity atoms. This results in distorted orbitals and thus perturbs the conduction electron density at the nucleus giving rise to a positive contribution to the hyperfine field at the nuclear site. By examining the $H_i(Z)$ values calculated from experimental values of sp impurities in Fe using E5.7.1 and E5.7.2 Stearns [R5.7.3] found that this so called "volume misfit" contribution was approximately proportional to the difference between the volume of the impurity atom in its pure state and that of the host and approximated it by

$$H_V(Z) = CA_Z(V_Z - V_h) \qquad \text{E5.7.3}$$

where C and V_h are constants determined by fitting H_V to $H(Z)-H_h(Z)$ as a function of the atomic number of the impurity atom. A_Z and V_Z are respectively the hyperfine coupling constant and atomic volume for the impurity.

In calculating hyperfine fields in Heusler alloys the host contribution is determined by scaling the hyperfine field measured at Cd impurities (which are assumed to be too small to have a significant

volume overlap contribution) using the hyperfine coupling constants:

$$H_h(Z) = H_{exp}(Cd)\frac{A_Z}{A_{Cd}}$$

Values of the hyperfine coupling constants have to be calculated by several workers (Watson and Bennett [R5.7.4], Campbell [R5.7.5], Norbeck and Stearns [R5.7.2]. This results in contributions which become more negative as the valence increases in the Z impurity atom. The total change in $H_h(Z)$ across the 5sp series is by a factor of 4. In order to account for the observed change of sign in hyperfine fields at the middle of the 3sp series using E5.7.1 then the values of $H_i(Z)$ must be small positive values for $H_Z(Cd)$ and rapidly increase with the atomic number of the atom.

Sondhi [R5,7.6] calculated H_V for the 5sp series of impurities in Fe using atomic Hartree-Fork $Fe^+(3d^7)$ radial wave functions for Fe. His results were an order of magnitude smaller than the experimental $H_i(Z)$ values and hence, he concluded that the volume overlap contribution was relatively unimportant in the determination of hyperfine field in Fe. This result supports the view (eg. Campbell and Vincze [R5.7.7], Price et al [R5.5.4]) that the Mn atoms in Heusler alloys are too distant from the 2nn Z sites to allow overlap between Mn 3d orbitals and Z s orbitals. However, Norbeck and Stearns [R5.6.2] using less localized 3d orbitals on the Mn ions and including second and third nearest neighbours have been able to obtain values of $H_i(Z)$ which are comparable to the experimental values of $H_V(Z)$ for the 5sp substitutional atoms in Heusler alloys.

The main advantage of the volume misfit model over the charge perturbation models of BC and JG is the fact that the contributions from the host matrix due to s-CEP and from the local properties of the impurity atom due to volume overlap are separable. Thus, by measuring hyperfine fields at small atoms such as Cd, Cu, Pt and Au where volume overlap contributions are expected to be small, then one obtains information about the s-CEP at various sites in Heusler alloy hosts. In addition, information about the electronic structure of different impurities in a single host is obtained from the volume overlap contribution and the measured hyperfine fields.

The main disadvantage in this theory is that a large number of hyperfine field measurements are required in order to define the empirical quantities in the emperical equations (E5.7.1, E5.7.2, E5.7.3). These include a hyperfine field measurement at a small atom (eg. Cd) located on the site of interest in order to determine H_h and hyperfine field measurements on at least 2 more sp impurity atoms on the same site where overlap is significant in order to obtain the constants C and V_h in E5.7.3. As a result, this theory can be usefully applied to only those experimental investigations where a large number of impurity atoms are substituted onto the same site in the same host matrix. Studies where one impurity atom is substituted into a series of host matrices cannot be analysed in terms of this theory. This is a serious shortcoming since it is this latter type of investigation which is currently the more popular of the two.

S5.8 Hyperfine Fields at Magnetic Sites.

Theoretical attempts to calculate the hyperfine fields measured at the nuclei of atoms processing a magnetic moment are even less fruitful than for non-magnetic atoms. This is largely due to the fact that the unpaired spins in the localized d electrons greatly perturb the core s electron densities at the nuclear site. This core polarization dominates other mechanisms (such as s-CEP and volume overlap with unpaired d orbitals on neighbouring atoms) which give rise to polarized electron densities at the nuclear site. Since this core polarization is opposite to the spin on the outer unpaired orbitals, the hyperfine field is usually negative at magnetic atoms. Exceptions occur when the core polarization contribution is dominated by the positive orbital contribution in the absence of quenching of the orbital moment. This effect is assumed to hold for the local contribution to the Co hyperfine fields in Heusler alloys where there is no moment on the Y atom (Khoi et al [R5.2.3]).

In view of the difficulties involved in calculating hyperfine fields form first principles, the usual approach is to separate the local contributions from the transferred contributions and determine the former by taking the difference between the total hyperfine field and the latter which is determined by substituting a non-magnetic impurity at the site of the magnetic ion. Khoi et al [R5.8.1] use the following empirical relationship to account for the observed hyperfine magnetic fields at Co and Mn ions in Heusler alloys:

$$H_i = h_0^i \mu_0 + h_1^i \Sigma \mu_1 + h_2^i \Sigma \mu_2 + \cdots \qquad \text{E5.8.1}$$

Here μ_0, μ_1, and μ_2 etc. are respectively the magnetic moments on the probe ion, first nearest neighbour ion, and the second nearest neighbour ions and h_0^i, h_1^i, h_2^i are coefficients to be determined. The contributions to the hyperfine field due to local properties of the prove atom is contained in the first term, while the transferred contributions due to the s-CEP induced at the probe site by the neighbouring magnetic ions are given by the other terms. Those transferred contributions were assumed to scale with the hyperfine coupling constants so that the induced s-CEP could be compared for different probe atoms,

$$p_j^i = h_j^i / A_i \qquad \text{E5.8.2}$$

Where A_i is the hyperfine coupling constant for the probe atom i and the p_j^i is the effective s-CEP in units of polarized s electrons per atom per μ_B induced by the j^{th} neighbour atom. Consistent values of the partial contributions were obtained by observing the change in the hyperfine fields when a non-magnetic atom was substituted for either the probe atom or one of its magnetic neighbour atoms. However, the magnetic moments of the magnetic probe atoms must be known a priori if this empirical approach is be used to determine the approximate contributions to hyperfine fields on the magnetic atoms. In the work

involving Fe hyperfine field measurements discussed in Chapter 7, this was not the case.

S5.9 References.

R5.2.1 Milford F.J., Am. J. Phys. 28 (1960) 521.

R5.2.2 Bethe H. and Salpeter E., Handbuch der Physik, 35 (1957) 193.

R5.2.3 Le Dang K., Veillet P. and Campbell I. A., Hyp. Int. 4 (1978) 379.

R5.2.4 Wertheim G.K., The Mossbauer Effect: Principles and Applications; Academic Press, New York, 1964.

R5.3.1 Daniel E. and Friedel J., Low Temp. Phys. LT9(B) (1965) 993.

R5.3.2 Ruderman M.A. and Kittel C., Phys. Rev. 96 (1954) 99.

R5.3.3 Kasuya T., Prog. Theor. Phys. 16 (1956) 45.

R5.3.4 Yasida K., Phys. Rev. 106 (1957) 893.

R5.3.5 Caroli B. and Blandin A., J. Phys. Chem. Sol. 27 (1966) 503.

R5.3.6 Rao G.N., At. Data Nuc. Data Tab. 15 (1975) 553.

R5.3.7 Campbell C.C.M. and Leiper W., A.I.P. Conf. Proc. 18 (1973) 319.

R5.3.8 Swartzendruber L.J. and Evans B.J., A.I.P. Conf: Proc. 10 (1972) 1369.

R5.4.1 Daniel E. and Friedel J., J. Phys. Chem. Sol. 24 (1963) 1601.

R5.4.2 Campbell I.A., J. Phys. C.: Sol. St. Phys. 2 (1969) 1338.

R5.5.1 Blandin A. and Campbell I.A., Phys. Rev. Lett. 31 (1973) 51.

R5.5.2 Friedel J., Nuo. Cem. 7 (1958) 287.

R5.5.3 Mayo W.R. and Dunlap R.A., J. App. Phys. 53 (1982) 8082.

R5.5.4 Price D.C., Rush J.D., Johnson C.E., Thomas M.F., and Webster P.J., J. de Physique C-37 (1976) C6-317.

R5.5.5 Dunlap R.A. and Jones D.F., Phys. Rev. B 26 (1982) 6013.

R5.5.6 Ishida S., Ishida J., Ansano S. and Yamahita J., J. Phys. Soc. Jap. 45 (1978) 1239.
Ishida S., Kubo Y., Ishida J. and Ansano S., J. Phys. Soc. Jap. 48 (1980) 814.
Ishida S., Akazawa S., Kubo Y. and Ishida J., J. Phys. F: Met. Phys. 12 (1982) 1111.

R5.5.7 See R5.6.2 and R5.6.3.

R5.5.8 Daniel E., Sol. St. Comm. 9 (1971) 1359.

R5.5.9 Campbell I.A. and Blandin A., J. Mag. Mag. Mat. 1 (1975) 1.

R5.5.10 Jena P. and Geldart G.J.W., Phys. Rev. B 7 (1973) 439.

R5.5.11 Allout H. J. Phys. F: Met. Phys. 4 (1974) 1501.

R5.6.1 See R5.5.10, R5.6.2 and R5.6.3.

R5.6.2 Jena P. and Geldart G.J.W., Sol. St. Comm. 15 (1974) 139.

R5.6.3 Jena P. and Geldart G.J.W., J. Mag. Mag. Mat. 8 (1978) 99.

R5.6.4 Delyagin N.N., Zonnenberg Y.D., Krylev V.I. and Nesterov V.I., Hyp. Int. 11 (1981) 65.

R5.7.1 Stearns M.B., Phys. Lett. A 34 (1971) 146; Phys. Rev. B 4 (1971) 4081; 8 (1973) 4383.

R5.7.2 Norbeck J.M. and Stearns M.B., J. App. Phys. 50 (1979) 2063.

R5.7.3 Stearns M.B., Phys. Rev. B 13 (1976) 4180; See also R5.7.1.

R5.7.4 Watson R.E. and Bennett L.H., Phys. Rev. B 15 (1977) 502.

R5.7.5 Campbell I.A., J. Phys. C: Sol. St. Phys. 2 (1969) 1388.

R5.7.6 Sondhi I., J. Chem. Phys. 62 (1975) 1385.

R5.7.7 Campbell I.A. and Vincze I., Phys. Rev. B 13 (1976) 4178.

R5.8.1 Le Dang K., Veillet P. and Campbell I.A., J. Phys. F: Met. Phys. 8 (1978) 1811.

HYPERFINE FIELDS MEASURED AT NON-MAGNETIC SITES

S6.1 Introduction.

This chapter deals with the hyperfine fields measured at the nuclei of atoms not carrying magnetic moments in Heusler alloys. These measurements include H_Z(Te) in Pd_2MnSb, H_X(Au) and H_Z(Sn) in PtMnSn and H_X(Ir) and H_Z(Sn) in $Ir_{1.07}Mn_{1.07}Sn_{0.86}$.

S6.2 Hyperfine Field at ^{125}Te Nuclei on Sb Sites in Pd_2MnSb.

As indicated previously the trends in the hyperfine fields measured at 5sp metals Cd to Sb in Heusler alloys are very similar to those found in ferromagnetic transition metal hosts. The fields at all these atoms had previously been measured in the Pd_2MnSb alloy with the exception of In. The purpose of this experiment was to extend the hyperfine field measurements to the Te atoms and compare the result with the predictions from the JG and BC models.

The simplest approach to making this measurement would be to substitute Te as an impurity into the D sites of the Pd_2MnSb alloy in place of the Sb following the practice established by Campbell and Leiper [R6.2.1] and Swartzdruber and Evans [R6.2.2]. However, unlike Sn which was used as a impurity atom in these works, no Heusler alloys exist which contain Te. Hence, it was not clear that Te would enter the Sb site. A liquid Helium temperature Mossbauer spectrum of a sample prepared in this manner contained only a single paramagnetic absorption line.

The procedure adopted to overcome this problem was to prepare a Pd_2MnSb alloy using radioactive ^{125}Sb which decays to ^{125}Te by β-emission and to perform a source experiment. Because of the low recoil energies (<0.1 eV) involved in this process, the Te is not expected to be dislodged from the site thereby ensuring that the resulting hyperfine fields would be measured at the D sites. Furthermore, since the half life of the 144.9 keV level of $^{125}Te^m$, which is the excited state from which the Mossbauer state is populated, has a relatively long half life ($\tau_{1/2}$=58 days), after effects due to the $^{125}Sb(\beta,\gamma)^{125}Te$ reaction have long since relaxed. Thus, the observed hyperfine field splitting pattern would be identical to that obtained by incorporating Te directly into the Pd_2MnSb structure.

Two Pd_2MnSb alloys, one with and one without 10 mCi of ^{125}Sb electroplated onto Pd foil were prepared by rf induction melting stoichiometic quantities of high purity Pd, Mn and Sb in an argon atmosphere. Both alloys were powdered and annealed in argon for three days at 650 °C and showly cooled. The non-radioactive sample exhibited less than 0.5% weight loss on preparation. An x-ray diffraction pattern of this sample was consistent with a single phase alloy with the $L2_1$ structure and indicated a lattice parameter of 6.420(6) Å. This value agrees with the values reported by other workers: 6.419(10) Å (Swartzendruber and Evans [R6.2.3]) and 6.413(8) Å (Webster and Ramadan [R6.2.4]). Since both alloys were prepared in an identical fashion, it was assumed that these results

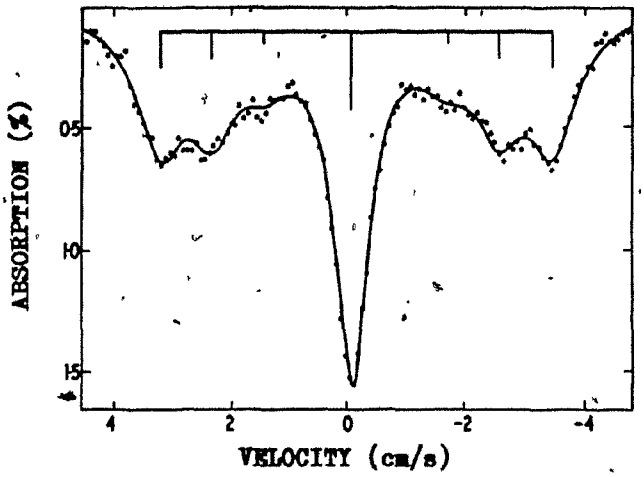

F6.2.1 Fitted spectrum of $^{125}Sb/Pd_2MnSb$ v.s. ZnTe, both at T = 4.2 K.

were applicable to the radioactive alloy as well.

Using the $^{125}Sb/Pd_2MnSb$ alloy as a Mossbauer source and a ZnTe (50 mg/cm^2) absorber, both at 4.2 K, a Mossbauer spectrum was accumulated. The statistics were improved by folding the two spectrum halves and pair summing the result to yield the spectrum shown in F6.2.1. The solid curve through the data points was obtained by fitting a singlet and a sextet with intrinsic Mossbauer parameters appropriate for ^{125}Te. Such two component spectra for Pd_2MnSb have also been obtained by Boolchand et al [R6.2.5] and de Waard and Lakshminarayana [R6.2.6].

The origin of the singlet absorption line has not been definitely established. One explanation involves the two stage decay of ^{125}Sb to the Mossbauer excited state. Because of the relatively long half life

of the intermediate state, $^{125}Te^{m}$, an appreciable amount of ^{125}Sb which had already decayed to this state prior to the fabrication of the alloy still remained in this state at the time that the spectrum was accumulated. Since Te is not easily incorporated into the D sites of Pd_2MnSb the $^{125}Te^{m}$ atoms would give rise to a second component in the Mossbauer spectrum. However, calculations reveal that the intensity of the singlet relative to the sextet should be about 0.22 while the spectrum reveals a ratio of about 0.5. A further contribution to the singlet might have arisen if some of the ^{121}Sb which was in the form of 1000 Å layer electroplated onto a thin Pd foil may have evaporated on heating and later condensed on the surface of the cooling alloy. Attempts at comparing the isomer shifts of the singlet to that found in $Pd_2MnSb_{0.9}Te_{0.1}$ were not successful because of problems encountered with the calibration spectra for the latter.

The hyperfine field which corresponded to the sextet was determined to have a magnitude of 85(3) T. The sign of the field, although not measured, was presumed to be positive and was subsequently found to be so by other workers. This result compares favorably with subsequent measurements by other workers. These results are given in T6.2.1.

The error is mostly due to the fact that large Doppler velocities (±5 cm/s) were required to exhibit the complete hyperfine absorption pattern for $^{121}Sb/Pd_2MnSb$ compared to those required for the Fe foil calibration (±7 mm/s). This lead to a large uncertainity in the velocity calibration constant for the ^{125}Te spectrum. For this reason

T6.2.1 Hyperfine Field Values at Te nuclei substituted on Sb sites in Pd_2MnSb.

H_Z(Te) (T)	Temperature (K)	Source	Absorber	Reference
85(3)	4.2	$^{125}Sb/Pd_2MnSb$	ZnTe	this work
+85.7(9)	4.2	$^{125}Sb/Pd_2MnSb$	ZnTe	R6.2.5
86.4(5)	4.2	$^{125}Sb/Pd_2MnSb$	ZnTe	R6.2.6
86.0(5)	4.2	$^{125}Te^m/Pd_2MnSb$	ZnTe	R6.2.6
85.6(9)	4.2	$^{125}Te^m/Pd_2MnSb$	ZnTe	R6.2.18

the isomer shifts were not determined.

Because the field value obtained at the Te impurity in Pd_2MnSb (85.0 T) was the largest obtained to date, an attempt was made to obtain a more accurate value for the magnitude of magnetic dipole moment of the excited Mossbauer state. The current measured values for μ' and μ'' had been $+0.62(2)\,\mu_N$ and $-0.88235(4)\,\mu_N$ respectively. By allowing g'/g'' to be an unconstrained parameter to be fitted, a value of 0.207(16) was obtained from the experimental spectrum. This value corresponds to $\mu' = g'I'M''/(g''I'') = 0.55(2)\,\mu_N$. The large error and deviation between these results again was attributable mainly to non-linearities and instabilities in the Doppler velocity waveform. These values of g'/g'' and μ' are comparable to the values of $-0.2270(15)$ and $0.604(4)\,\mu_N$, respectively, which were obtained by

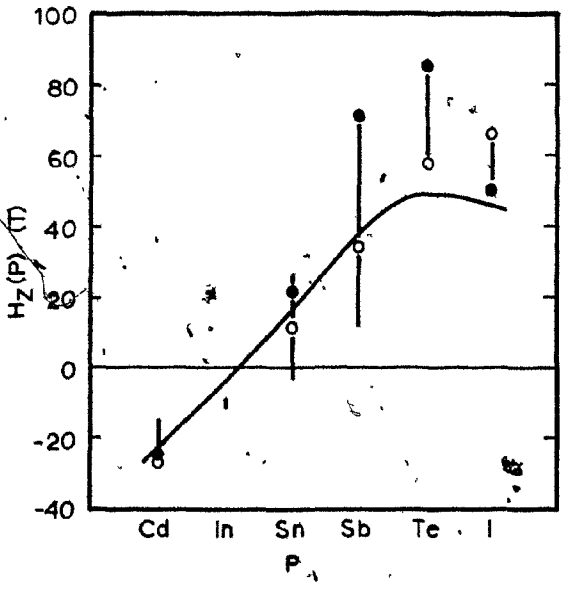

F6.2.2 Z site 5sp impurity hyperfine fields measured in Pd_2MnSb (•) and PdMnSb (o) plotted as a function of Z. The solid curve represents the predictions of Jena and Geldart [R6.2.22]. The vertical lines represent the total range of impurity 5sp hyperfine fields in all Heusler hosts. References for the Pd_2MnSb host are: Cd - R6.2.19, R6.2.10; Sn - R6.2.20; Sb - R6.2.3, R6.2.21; Te - This and other work (See T6.2.2); I - R6.2.6, R6.2.18. References for the PdMnSb host are given in R6.2.8.

Boolchand et al [R6.2.5].

The results of this and other more recent work in the measurement of the hyperfine fields for Cd to I sites in Pd_2MnSb appear in F6.2.2. These trends toward increasingly more positive fields as the atomic number of the impurity increases is common in ferromagnetic hosts (See

Rao [R6.2.7] for summary of hyperfine field values for impurities in non-Heusler hosts). However, in these cases the hyperfine fields do not exhibit a saturation value and then decrease before iodine. A similar curve is obtained for the PdMnSb host, as is shown in F6.2.2. However, the whole curve appears to be shifted toward the right to the I impurity and no saturation effects are observed in the 5sp series. The solid curve in the figure is calculated by the JG theory. They calculated the Fermi wave vector k_F using the free electron model from the average conduction electron density using the method described in S5.4 except that Pd atoms were each assumed to contribute 1.2 electrons to the conduction band. The band splitting parameter Δ/E_F was chosen to normalize the theoretical result to the experimental value for the hyperfine field measured at Sb nuclei PdMnSb and then scaled according to the magnetic moment on the Mn atoms in the host alloy. Thus, the curve is the result of an attempt to explain the trends of hyperfine fields at sp impurity sites in all Heusler alloys. Hence, although Figure 6.2.2 would seem to indicate otherwise, the quantitative agreement between experiment and the JG theory is quite good. The qualitative trends, namely, fields increasing from negative to positive values and then decreasing as the valence of the probe atom increases from Cd to I, are correctly produced by this theory.

Using the JG theory, Boolchand et al [R6.2.8] have attempted to reproduce the shift in the 5sp impurity hyperfine field curve as the Pd concentration is increased in the Pd-Mn-Sb Heusler alloys in going from the $C1_b$ to the $L2_1$ structure. The found essentially little

change in the theoretical curve predicted by the JG theory. Hence, they concluded that the JG theory was not applicable to the Pd-based Heusler alloys.

The BC model, with its explicit sinusoidal dependence on the impurity charge of non-magnetic ions in ferromagnetic hosts, can automatically account for the change of sign and the saturation of hyperfine fields measured at the 5sp impurities with reasonable values of k_F and Z_{eff} (see E5.5.6 and E5.5.9). However, quantitative agreement is poor (Schaaf et al [R6.2.9]). When the k_F values are adjusted so as to cause the saturation point on the curve to coincide with experiment the theoretical field values were found to be 30% too low.

This result is not surprising because Blandin and Campbell [R6.2.10] originally applied their theory to the Cu_2MnIn host where they were able to obtain qualitatively good agreement with the fields impurities up to Z=Sb. However, when In is changed to Sb this would increase conduction electron concentration, n_0 from 1.25 to 1.75 electrons per atom, considerably reducing the size of the screening phase shift 2_0 for a given impurity atom. Blandin and Campbell [R6.2.10] suggested that Pd atoms contribute very few electrons to the conduction band (about 0.12) thereby restoring n_0 to the value used for the Cu_2MnIn host. However, this does not account for the rapid increase in the hyperfine field measured at the Sb atoms when the number of Pd atoms is changed in the $Pd_{1+x}MnSb$ alloy system (Swartzendruber and Evans [R6.2.2], Price et al [R6.2.11], where the

T6.2.2 Calculation of the hyperfine fields at sp impurities in the Pd_2MnSb host using Stearns' Volume Misfit Model.

Z	A_Z (T)	$H_h(Z)$ (T)	V_Z ($Å^3$)	$H_V(Z)$ (T)	H(Z) (T)	H_{exp} (T)
Cd	470	-23	12.7	0	-23	-23
In	680	-33	14.9	29	-4	-
Sn	900	-44	16.7	65	21	+21
Sb	1130	-55	18.5	115	+60	+60
Te	1390	-68	20.5	187	+119	+85
I	1680	-82	(25.5)	(364)	(+282)	50

field changes from 30 T for the $C1_b$ structure to 60 T for the $L2_1$ structure. Since such a large change does not occur in the $Ni_{1+x}MnSb$ system (Swartzendruber and Evans [R6.2.12], Price et al [R6.2.11]) where the electronic structure of the constituent atoms is the same as in the Pd based system, it is possible that Pd based alloys are exhibiting an anomalous hyperfine field dependence on Z.

According to Stearns' volume misfit model (See S5.7) the hyperfine field at the Z site atom ought to be given by E5.7.1. The volume overlap contribution at the Cd impurity nucleus is considered negligible. Using the experimental values of $H_Z(Cd)$ of -23 T (Lindgren et al [R6.2.13], Schaaf et al [R6.2.9]), and the A_Z values of Stearns [R6.2.14], the values of H_h are found as indicated in

T6.2.2. The values of V_Z used to determine $H_V(Z)$ were the "smoothed" values of Stearns [R6.2.15]. which take into account differences in crystal structures of these atoms in their natural state. The value for V_I was obtained by scaling the value of V_{Te} with the atomic concentrations in the Te and I solids. The value of $H(Z)-H_h(Z)$, Z = Sn,Sb were used to determine the values of C and V_h in E5.7.3. These were found to be 0.164 Å^{-3} and 12.30 Å^3 respectively.

The overall trend in the hyperfine fields measured at sp impurity atoms are reproduced in the volume misfit model except for the lack of a saturation in the field values for Z=Te. The anonomously large value for the iodine field is due to the large value of V_I. If this value is obtained by the extrapolation of Stearn's "smoothed" values of V_Z, the resulting field value is still about 200 T. It would seem that Stearns model is incapable of accounting for a saturation in field values before the end of an sp series because of the monotomically increasing dependence of the atomic volume on atomic number. This lack of saturation is reflected in the detailed theoretical calculations of H_V by Norbeck and Stearns [R6.2.16]. There appears no obvious way to account for this saturation effect within the volume misfit model unless another external mechanism is incorporated into the model which might lead to a decrease in hyperfine fields measured at high valence sp impurities.

It would appear that all three models can account qualitatively at least for the increasing hyperfine fields measured at 5sp impurities on the D sites in the Pd_2MnSb alloy. However, only the

charge perturbation models of BC and JG reproduce the saturation in the field value measured at the Te probe atom.

S6.3 Hyperfine Fields at Au and Sn Nuclei in PtMnSn.

Although hyperfine fields had been measured at a large number of nuclear sites belonging to elements in the fourth and fifth row of the periodic table fewer hyperfine fields had been measured at period six sites in Heusler alloys. Among these were the hyperfine fields measured at Au atoms in Au_2MnAl [R6.3.1] and in AuMnSb [R6.3.2]. The first measurement of a hyperfine field at a Au impurity atom in a Heusler alloy, Au substituting the Pt in PtMnSn, is presented here.

Because of the large X-ray atomic scattering factor for Pt relative to those of Mn and Sn, it is difficult to distinguish between $C1_b$ and C1 structures using this method (Masumoto and Watanabe [R6.3.3], Gorlich et al [R6.3.4]). Masumoto and Watanabe [R6.3.3] have reported the PtMnSn alloy, when water quenched from 1250 °C, to be ferromagnetic with a Curie temperature of 354 K and a saturation magnetic moment per Mn atom of 3.37 μ_B. However, these values depend upon the precise heat treatment of alloy.

In the Au hyperfine field measurement advantage was taken of the fact that ^{197}Pt is the parent of the ^{197}Au Mossbauer nuclide. Thus, the Au hyperfine field in PtMnSn was obtained by using ^{197}Pt in a PtMnSn matrix as a source and a single line Au foil as an absorber in a Mossbauer spectroscopy measurement.

The source was prepared by irradiating a 97mg Pt foil, enriched to 97.5% with ^{196}Pt for six hours with a neutron flux of 10^{12} neutrons $cm^{-2}s^{-1}$ in the Slowpoke reactor at Dalhousie University. The ^{197}Pt nuclide was produced by the reaction $^{196}Pt(n,\gamma)^{197}Pt$. Details of the irradiation procedure have been given by Judah [R6.3.5]. The radioactive ^{197}Pt was incorporated into a PtMnSn matrix by melting the Pt foil with stoichiometric quantities of high purity Mn and Sn under Ar at one atomsphere pressure in an rf induction furnace. The alloy was kept molten for greater than two minutes to ensure complete melting and homogeneity. The alloy was cooled from the melt by turning the rf power off. Because of the short half life of ^{197}Pt (18 hours) no subsequent heat treatment was performed on this sample.

The source and a 200 mg/cm^2 thick Au foil were held at 4.2 K while the spectrum was accumulated. The statistics of this spectrum were improved by folding one half of the spectrum onto the other half as described in S4.6. The point about which the spectrum was folded was defined by the centroids of the absorption patterns of the individually fitted spectrum halves. The resulting spectrum is shown in F6.3.1. The solid curve represents the least squares fit to the hyperfine splitting pattern appropriate to ^{197}Au in a polycrystalline powdered sample. This pattern consisted of the eight absorption lines in ^{197}Au as given in T3.7.3. It was assumed that because of the cubic symmetry of the lattice that the electric field gradient at the nuclear site was zero. The hyperfine field corresponding to this fitted curve was found to be 70(1) T. The isomer shift of ^{197}Au in

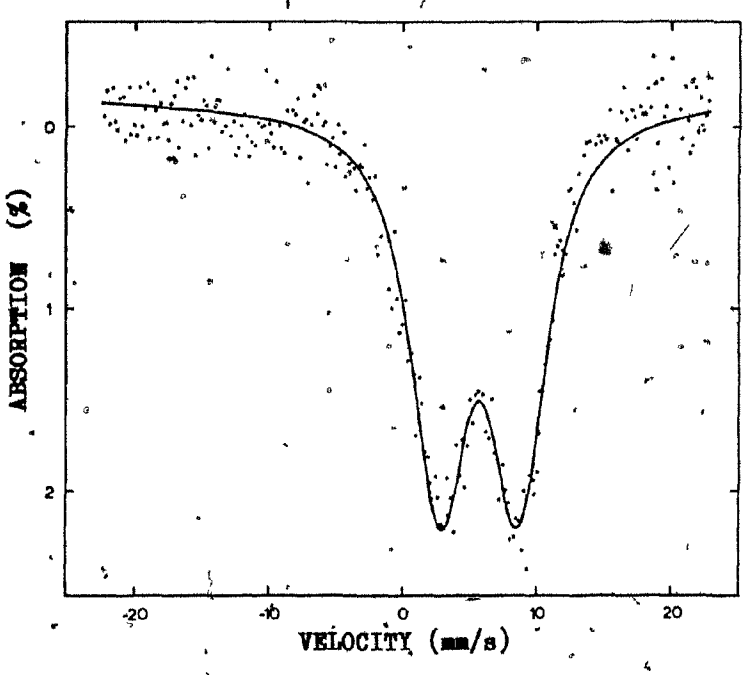

F6.3.1 Fitted spectrum of ^{197}Pt/PtMnSn v.s. Au foil, both at T = 4.2 K.

the PtMnSn matrix relative to ^{197}Au in a Au foil matrix was found to be -4.66(4) mm/s when referred to the same source matrix. This figure was arrived at by using the known isomer shift (+.226(10) mm/s) of ^{57}Fe in Cu with respect to Fe in Fe to determine the absolute velocity scale from the ^{57}Co/Cu v.s. Fe foil calibration spectrum. The width of the individual absorption lines constrained to be equal, was found to be 4.3(1) mm/s which is about 2.3 times larger than natural Mossbauer width. This width is consistant with the rather thick absorber and the short source-to-detector distance used during data accumulation.

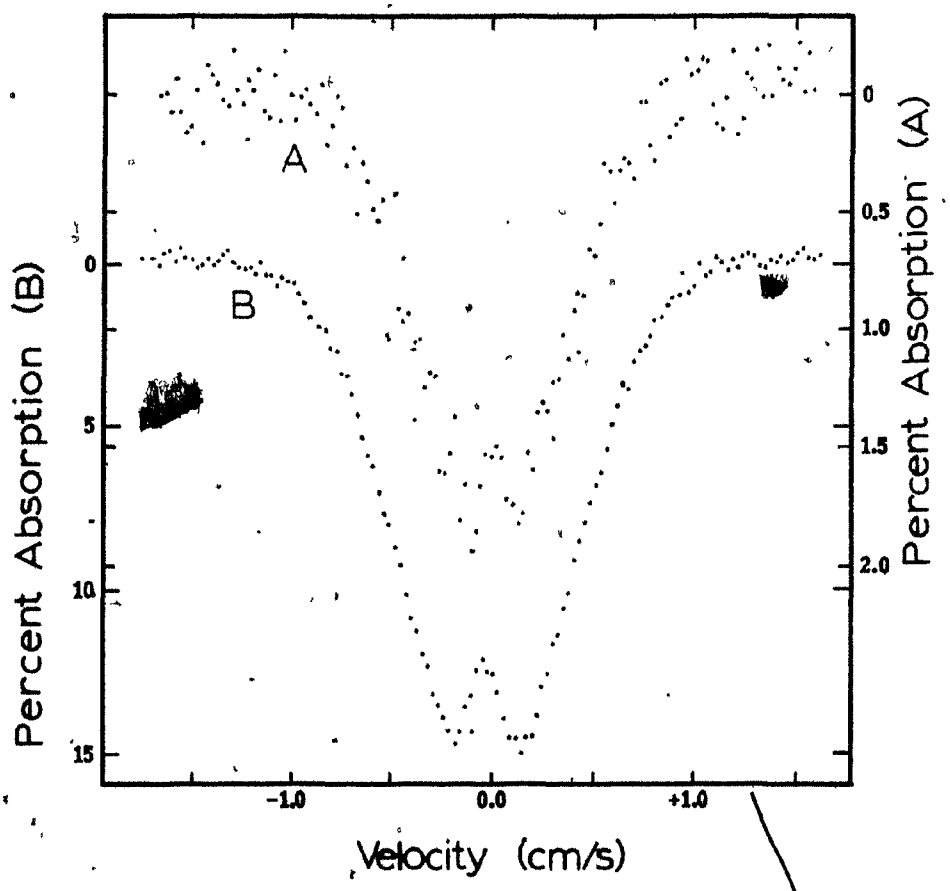

F6.3.2 Unfitted spectra of $^{119}Sn^{m}$/SnV v.s. PtMnSn, both at T = 77 K, with (A) and without (B) an applied transverse field of 1.0 T.

After the intensity of the ^{197}Pt activity had died away, the hyperfine field at the Sn site was measured in the $^{197}PtMnSn$ sample by using a $^{119m}Sn/VSn$ source and the $^{197}PtMnSn$ sample as an absorber. The spectrum was accumulated while the absorber was held at 77 K. This spectrum was obtained with and without an externally applied field of 1.0 T. These spectra are shown in F6.3.2. As can be seen in

the figure, the field is negative. This agrees with the result of Leiper et al [R6.3.6] and Arbique [R6.3.7], but is in conflict with the previously reported results of Rao and Iyengar [R6.3.8] and Campbell [R6.3.9].

Several attempts to fit the experimental spectra with a sextet appropriate to a M1 $(3/2^{+} \rightarrow 1/2^{+})$ ^{119}Sn transition were not successful. This was presumably due to a distribution of hyperfine fields due to disorder in the PtMnSn alloy. This ^{119}Sn spectrum is consistant with that obtained by Dunlap et al [R6.3.10] where the distribution of hyperfine fields was included in the fitting function using a program due to Window [R6.3.11]. These hyperfine field measurements at different probe sites in the PtMnSn host and those of other workers in the PtMnSn matrix are given in T6.3.1.

Examination of these results reveal a wide variety of values in the experimental results obtained for the hyperfine fields measured at Sn atoms. This is not surprising if one assumes that there is a varying amount of Mn-Sn disorder between the samples used by the various workers. Work by Dunlap et al [R6.3.10] and Gorlich et al [R6.3.4], where attempts were made to find some measure of the hyperfine field distributions at the Sn sites, indicate a relatively broad distribution in hyperfine fields which is consistant with the fact that the Mn sublattice may contain non-magnetic Sn atoms. More surprising is the fact that essentially no broadening occurs in the Au hyperfine fields. This would suggest that the hyperfine field at Au on Pt sites is either insensitive to the local ordering of the Mn

T6.3.1 Hyperfine Measurements in PtMnSn

Probe Site	Atom Type	H (T)	H/H (%)	T (K)	Technique	Reference
X	Pt	80	-	4.2	NMR	R6.3.12
X	Au	71(1)	-	4.2	ME	This work
Y	Mn	20.5	-	77	NMR	R6.3.13
Y	Mn	33.2	-	77	NMR	R6.3.12
Z	Sn	0	-	394	ME	R6.3.4
Z	Sn	+0.7	-	293	ME	R6.3.8
Z	Sn	0	-	293	ME	R6.3.10
Z	Sn	3.0	310	80	ME	R6.3.10
Z	Sn	-4.2(1)	-	80	ME	R6.3.7
Z	Sn	-3.0	-	77	ME	This work
Z	Sn	+2.3	-	77	ME	R6.3.9
Z	Sn	-4.3	.75	77	ME	R6.3.4
Z	Sn	+3.3	-	77	ME	R6.3.8
Z	Sn	-6(1)	-	4.2	ME	R6.3.6
Z	Sn	-6.2(1)	-	4.2	ME	R6.3.7

atoms or that the local short range of Mn atoms around the Pt atoms is relatively uniform. The former explanation is consistent with the JG theory, where no mechanism exists for considering the effects of disorder on the hyperfine fields measured at a particular probe atom. This suggests that the total CEP seen at each Pt site is influenced by fairly distant Mn atoms so that each Au atom sees essentially the same CEP even though the local order around Au atoms may vary.

According to the CB theory, the hyperfine field measured at a particular site is strongly dependent upon the distance to the Mn atoms around this site. This is consistent with the wide distribution observed in the hyperfine fields observed at the Sn sites if one assumes the presence of preferential Mn-Sn disorder. This can be seen by examining T2.2.1 which gives the first six neighbours to the A, B, C and D sites in Heusler alloys.

In the presence of perfect $C1_b$ order Mn is confined to the B sites, while Sn is confined to the D sites and Pt and also Au impurity atoms are confined to A sites, the C sites being vacant. Clearly if preferential Mn-Sn disorder occurs, then the average number of Mn atoms on the second and fourth nearest neighbours to Sn atoms on the D sites decreases while it increases in the third and fifth nearest neighbours. The variation of the number of Mn atoms on neighbouring sites form one Sn site to another would give rise to distributions in the CEP and hence hyperfine field at Sn atoms on D sites. The same effect occurs for Sn atoms on the B sites.

On the other hand, for each of the A sites only half of the atoms at the first, fourth and sixth nearest neighbour distances are Mn atoms in the fully ordered $C1_b$ structure, the other half being Sn atoms. For certain amounts of Mn-Sn disorder and radial dependencies of the CEP, the value of the CEP, and hence the hyperfine field may not vary appreciably from one Au site to the next. Also, if some of the Pt atoms and hence Au atoms migrate to C sites, as is suggested by Masumoto and Watanabe [R6.3.3] for certain heat treatments of PtMnSn, the hyperfine fields would be identical to those of Au atoms on the A site. This is because these two sites have the some configuration of Mn and Sn neighbours. Thus, it is possible that Mn-Sn disorder would not greatly influence the Au hyperfine fields at Pt sites in PtMnSn even though the Sn hyperfine field at the Sn sites is strongly perturbed.

It does not follow however that the hyperfine field at all probe atoms on X sites in Heusler alloys of composition XMnZ will be immune to Mn-Z disorder. The radial dependence of the CEP depends on the charge screening phase angle, $2\delta_0$, which depends on the local properties of the probe atom. This would explain why Malik et al [R6.3.12] observed broad NMR lines for the ^{195}Pt resonances in PtMnSn. The hyperfine fields of Pt atoms may be sensitive to the Mn-Sn disorder while the hyperfine fields at Au atoms are not.

S6.4 Hyperfine fields at Ir and Sn nuclei in $Ir_{1.07}Mn_{1.07}Sn_{0.86}$.

The measurement of the hyperfine field at the iridium sites in the Heusler alloy IrMnSn was performed to extend the number of hyperfine fields measured at atoms from the sixth series of the periodic table which up until this time had only included measurements at Pt an Au sites.

Masumoto and Watanabe [R6.4.1] have performed X-ray diffraction and magnetization measurements on the Ir-Mn-Sn ternary system. They found that the equi-atomic composition formed a polyphase mixture. However, the alloy of stoichiometry $Ir_{1.07}Mn_{1.07}Sn_{0.86}$ formed a single phase $C1_b$ structure with a lattice parameter of 6.182 Å. If particular interest is the fact that they reported the Ir, Mn, and Sn atoms to respectively occupy the B, D and A sites instead of the usual A, B and D sites respectively. This is equivalent to the Mn atoms, being located on the C sites instead of the B sites if Ir and Sn are assigned the A and D sites respectively. It would appear that this result is in conflict with the structure of Ir_2MnAl which, in the same paper, they indicate has the usual $L2_1$ Heusler structure. Also, as in the case for PtMnSn, the atomic scattering factors are such that it is difficult to distinguish between the $C1_b$ and C1 structures (Gorlich et al [R6.3.4]). Thus, the structure indicated by Masumoto and Watanabe should be viewed with caution. The Curie temperatures reported by two groups of workers, 265 K [R6.4.1], and 204 K [R6.3.4], were in disagreement. However, the two reported values for the magnetic moment per formula were in agreement at 2.2 μ_B.

For this work a 500 mg sample of $Ir_{1.07}Mn_{1.07}Sn_{0.86}$ was prepared from high purity components using rf induction melting. The heat treatment consisted of annealing at 900 °C for 95 hours followed by slow cooling at a rate of about 100 C°/hr. X-ray diffraction revealed a single phase structure compatable with the $C1_b$ or C1 structures and a lattice parameter of 6.201(5) Å in agreement with 6.199(12) obtained by Gorlich et al [R6.3.4].

To measure the hyperfine field at the Ir nuclei an ^{193}Ir source was prepared by irradiating 100 mg of Os, enriched to more than 95% with ^{192}Os , in a neutron flux of about 10^{12} neutrons $cm^{-2}s^{-1}$ for 16 hours [R6.3.5]. The ^{192}Os was in the form of a metallic sponge. In order to prevent the Os from vibrating with respect to the source holder during data accumulation, the Os, contained in a thin sealed polyethylene envelope, was clamped to the source holder with some Q compound using a 1mm thick nylon disk. This enabled the ^{192}Os to be removed for reirradiation should insufficient statistics be obtained after one irradiation. Using 100 mg cm^{-2} of $Ir_{1.07}Mn_{1.07}Sn_{0.86}$ as an absorber, the Mossbauer spectrum shown in F6.4.1, was accumulated with both the source and absorber at liquid helium temperatures.

Each spectrum half was independently fitted using an eight line hyperfine pattern compatible with the $1/2^+ - 3/2^+$ mixed E2/M1 transition between the Mossbauer and ground state of ^{193}Ir for a mixing ratio of 0.31. The relative heights and positions were constrained according to the ratios given in T3.7.3 while the widths of the absorption lines were constrained to be equal. Since the

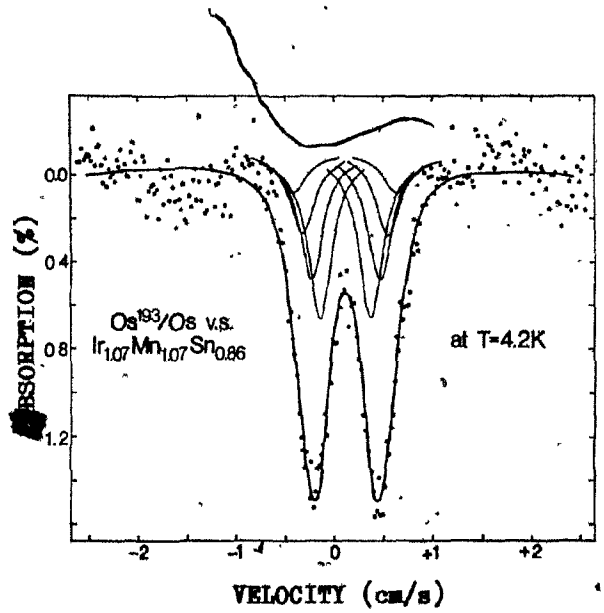

F6.4.1 Fitted spectrum of $^{193}Os/Os$ v.s. $Ir_{1.07}Mn_{1.07}Sn_{0.86}$, both at T = 4.2 K.

structure is cubic, the quadrupole splitting was fixed at zero. Hence, the spectrum was fitted using only six parameters: (1) the width of one of the absorption lines; (2) the intensity of one of them; (3) the position of their centroid; (4) the splitting parameter proportional to the separation of a symmetric pair of lines and (5) the height and (6) curvature of the baseline. The fitted parameters are given in T6.4.1.

The hyperfine field in $Ir_{1.07}Mn_{1.07}Sn_{0.86}$ has been subsequently remeasured by Amique [R6.3.7] where the sign was determined to be negative. The magnitude of his result 71.0(1.2) T differs from the result 65(2) T obtained in this work. However, in view of the considerably inferior statistics in the spectrum of this latter work, it is believed that the field value is closer to 65 T than 71 T.

T6.4.1 Fitted Parameters for the 4.2 K spectrum of $^{193}Os/Os$ v.s. $^{193}Ir/Ir_{1.07}Mn_{1.07}Sn_{0.86}$ x.

Spectrum Half	Line Width (mm/s)	Isomer Shift* (mm/s)	Hyperfine Field (T)
First	3.06(16)	1.16(5)	64.3(12)
Second	2.78(16)	1.28(5)	65.8(12)
Average	2.92(11)	1.22(4)	65.1(8)

* with respect to an Os metal source.

Two spectra using 30 mg cm^{-2} of $Ir_{1.07}Mn_{1.07}Sn_{0.86}$ at 77 K as an absorber and a $^{119}Sn^{m}/SnV$ source at 77 K were accumulated. These spectra differed only in that a different maximum velocity setting was used for each spectrum. The fitted spectra with the two velocity settings are shown in F6.4.2. The fitting model consisted of 6 absorption lines compatable with the $3/2^{+}$ - $1/2^{+}$ pure M1 transition of the ^{119}Sn nuclide. As in fitting the ^{193}Ir spectrum six free fitting parameters were used. The data for the high velocity spectrum is given in T6.4.2.

It is interesting to note that the low velocity spectrum resulted in a $H_{\mathcal{Z}}(Sn)$ = 2.8(4) T as reported in Leiper et al [R6.4.2]. The larger uncertainity is presumably due to the fact that at this low velocity setting the curvature of the baseline is poorly defined and

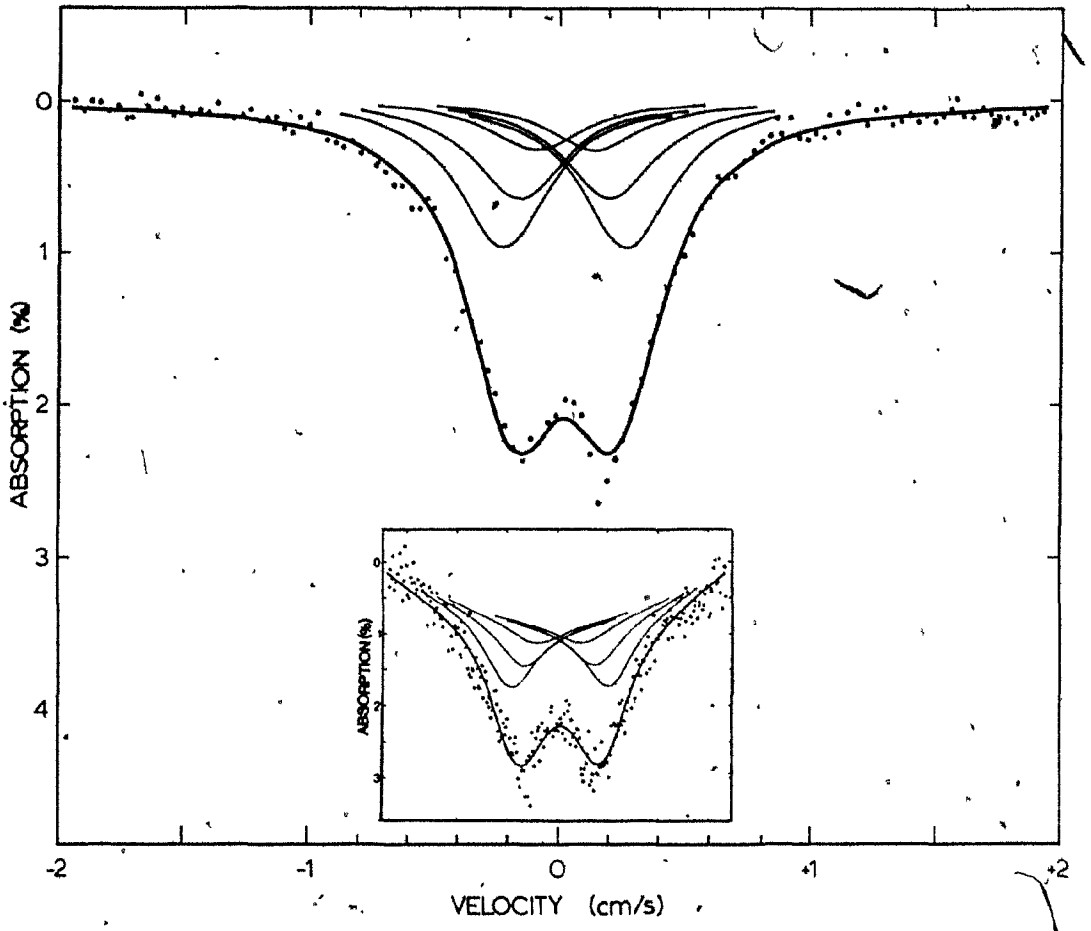

F6.4.2 Fitted spectra of $^{119}Sn^{m}$/SnV v.s. $Ir_{1.07}Mn_{1.07}Sn_{0.86}$, both at T = 77 K. The upper (lower) spectrum was obtained at high (low) maximum Doppler velocity setting. In each spectrum the heavier lines represent the computer-fitted total absorption curve. The finer lines represent the absorption for each of the individual hyperfine transitions in the ^{119}Sn sextet. The curvature of the baseline in the low velocity spectrum is clearly exaggerated. Hence, the fitted intensity and hyperfine splitting parameters are too small in this spectrum.

T6.4.2 Fitted parameters for the high velocity spectrum of $^{119}Sn^{m}/SnV$ v.s. $^{119}Sn/Ir_{1.07}Mn_{1.07}Sn_{0.86}$.

Spectrum Half	Line Width (mm/s)	Isomer Shift* (mm/s)	Hyperfine Field (T)
First	4.23(13)	0.22(3)	3.58(6)
Second	4.06(13)	0.07(3)	3.56(6)
Average	4.14(9)	0.15(2)	3.57(4)

* with respect to the SnV source matrix.

hence may adopt a variety of values without appreciably affecting the "goodness of fit" parameter χ^2. Changing the baseline curvature affects the fitted intensity parameter in turn would affect the spacing of the individual absorption lines. In general, spectra should be accumulated at a velocity setting so that the base line is well defined to minimize the correlation between the baseline fitted parameters and the resonant absorption fitted parometers. This is particularly important for spectra where the individual absorption lines are poorly resolved such as in spectra obtained using the ^{119}Sn and ^{121}Sb Mossbauer nuclides where the individual line widths can be comparable to typical hyperfine splittings.

The value of $H_Z(Sn)$ in $Ir_{1.07}Mn_{1.07}Sn_{0.86}$ has been measured at liquid helium temperatures and was found to be 5.9(1) T by Gorlich et al [R6.3.4] and +6.0(1) T by Arbique et al [R6.4.3]. This value is

too large to be compatible with the value obtained in this work if these values are scaled according to the magnetization curves obtained by Masumoto and Watanabe [R6.4.1]. However, this may be accounted for by the fact that $Ir_{1.07}Mn_{1.07}Sn_{0.86}$ is very sensitive to the heat treatment on preparation.

Among the Heusler alloys examined by Dunlap et al [R6.3.10] for hyperfine field distributions at Sn atoms was the $Ir_{1.07}Mn_{1.07}Sn_{0.86}$ alloy. At a temperature of 80 K, they found the maximum in the distribution curve occurred at 3.0 T which is consistant with this result. They also found a full width at half maximum value of 6 T in the field distribution peak. This wide distribution, twice the field value, is consistant with the large line widths found in the ^{119}Sn spectrum.

Unlike the ^{197}Au spectrum in PtMnSn, the ^{193}Ir in $Ir_{1.07}Mn_{1.07}Sn_{0.86}$ was found to exhibit broadened lines which were five times their natural line width. This may be attributable in part to the $^{193}Os/Os$ source whose physical structure was not optimized to produce minimum line widths.

The theoretical calculations of $H_X(Ir)$ are discussed in the following section in relation to the predicted values of $H_X(Au)$ and $H_X(Pt)$ found in several Heusler alloys containing period six atoms at the X sites.

S6.5 Calculation of Period Six Fields in Heusler Alloys.

In this section the JG and BC theories are used to account for the trends observed in period six hyperfine fields. The Stearns' volume misfit model is not used here because there is insufficient field measurements at the X sites to obtain the empirically fitted constants used in this model (See S5.7).

In these calculations, the valence of the X atoms is assumed to be one in all cases (See S5.5). The valance of Sn and Sb are assumed to be 4 and 5 respectively. The contribution of each atom to the conduction band is assumed to be equal to the valance of the non-magnetic atoms and to be 2-μ for Mn atoms as discussed in S5.5. The hyperfine field values are normalized to $H_X(Au) = 70.5$ T in PtMnSn.

The BC theory was applied by summing the preasymtotic expression for the CEP given by E5.5.10 over the first 25 Mn shells for each of the Heusler alloy hosts. These values were then multiplied by the hyperfine coupling constants given by Campbell [R6.5.1] and value of the magnetic moment per Mn atom. The results of these calculations appear in T6.5.1.

The calculations for the JG theory were somewhat more involved since in E5.6.1 the value of k_F affects in a complicated manner both the Bloch enhancement factors, $\alpha^2(k_F)$, and the CEP at the nuclear site, P(0). In addition, the value of $\alpha^2(k_F)$ depends on the type of inpurity atom as well. The Bloch enhancement factors for the period six atoms are determined by extropolating the values for the 4sp and

T6.5.1 Comparison of experimental and theoretical values of Hyperfine Fields at Period Six Atoms.

P	Host	Hyperfine Fields $[H_X(P)]$ (T) Theoretical JG	BC	Experimental Value	Reference
Au	Au_2MnAl	-76	-117	-121	R6.3.1
Pt	PtMnSn	-70.7	-60	-80	R6.3.12
Au	PtMnSn	-70.5	-70.5	-70.5	This work
Ir	$Ir_{1.07}Mn_{1.07}Sn_{0.86}$	-55	-13	-65	This work
Au	AuMnSb	-42	-43	-24	R6.3.2

5sp elements given by Jena and Geldart [R6.2.22] to the 6sp series as a function of atomic number and then by extrapolating the values obtained for Au through Pb, back to Ir and Pt. These extrapolations give the values of the Bloch enhancement factors for $k_F = 0.62\ a_0^{-1}$. A crude correction for the k_F dependence is obtained by extrapolating a plot of the values of $\{\Delta[\alpha^2(k_F)]/\Delta k_F\}/[\alpha^2(0.62\ a_0^{-1})]$ for the Group IIIA elements given in Figure 2 of Jena and Geldart [R6.2.22] as a function of Z to the period six element. This results in a value of approximately $-2a_0$ for this quantity. This value is used to adjust the Bloch enhancement for the Ir, Pt and Au atoms for small changes in the k_F. The P(0) values are obtained from Figure 1 of Jena and Geldart [R6.5.2], and scaled according to the magnetic moment assumed

to localized on the Mn ions in these alloys. Using these methods, a approximate expression for the hyperfine fields is given by:

$$H_X(X) = K\,\alpha^2(0.62\,a_0^{-1})\,\{1-2a_0^{-1}[k_F-(0.62\,a_0^{-1})]\}\,\mu\,P(0) \quad \text{E6.5.1}$$

where K is a normalization constant. The results of these calculations are also given in T6.5.1.

The overall trend in the experimental values is reproduced by the JG theory, although quantitative agreement is poor. However, the BC calculation fails to reproduce the relative magnitude in the Ir field $Ir_{1.07}Mn_{1.07}Sn_{0.86}$ and the relative magnitudes of the Pt and Au fields in PtMnSn. The latter discrepancy may be due to inaccurate values of the hyperfine coupling constants. However, the former disagreement is due to the anomously low value for the spin polarization obtained at the Ir nucleus in $Ir_{1.07}Mn_{1.07}Sn_{0.86}$ alloy. On the other hand, the BC theory gives better numerical agreement with the experimental values for the Au fields in these alloys. In this case, the use of inaccurate values for hyperfine coupling constants has no effect on the relative field values obtained from the BC theory since they affect only the relative fields calculated for different probe atoms.

In summary, the JG theory is able to reproduce the trends observed in the experimental values of the various hyperfine fields measured at different probe atoms. However, the BC theory better reproduces the range of values found experimentally for $H_X(Au)$. But it does not reproduce the observed trends of the hyperfine fields at

other impurity atoms relative to the values of $H_X(Au)$.

S6.6 References.

R6.2.1 Campbell C.C.M. and Leiper W., A.I.P. Conf. Proc. 18 (1973) 319.

R6.2.2 Swartzendruber L.J. and Evans B.J., A.I.P. Conf. Proc. 10 (1972) 1369.

R6.2.3 Swartzendruber L.J. and Evans B.J., Phys. Lett. A 38 (1972) 511.

R6.2.4 Webster P.J. and Ramadan M.R.J., J. Mag. Mag. Mat. 5 (1977) 51.

R6.2.5 Boolchand P., Tenhover M., Jha S., Langouche G., Triplett B.B. and Hanna S.S., Phys. Lett. A 54 (1975) 293.

R6.2.6 De Waard H. and Lakshimarayana V., Phys. Lett. A 69 (1968) 219.

R6.2.7 Rao G.N., At. Data and Nuc. Data Tab. 15 (1975) 553.

R6.2.8 Boolchand P., Tenhover M., Marcuso M., Blizzard M., Kim C.S., Langouche G., van Rossum M., and Coussement R. Hyp. Int. 4 (1978) 388.

R6.2.9 Schaaf J., Pasquevich A.F., Schreiner W.H., Campbell C.C.M., Fraga E.R. and Zalislak F.C., J. Mag. Mag. Mat. 21 (1980) 24.

R6.2.10 Blandin A. and Campbell I.A., Phys. Lett. A 31 (1973) 51.

R6.2.11 Price D.C., Rush J.D., Johnson C.E., Thomas M.F. and Webster P.J., J. de Physique 37 (1976) C6-317.

R6.2.12 Swartzendruber L.J. and Evans B.J. A.I.P., Conf. Proc. 5 (1972) 539.

R6.2.13 Lindgren B., Pernestal K., bedi S. and Karlson E., J. Phys. F: Met. Phys. 7 (1977) 2405.

R6.2.14 Stearns M.B., J. App. Phys. 50 (1979) 2060.

R6.2.15 Stearns M.B., Private communication to W. Leiper (1975).

R6.2.16 Norbeck J.M. and Stearns M.B., J. App. Phys. 50 (1979) 2065.

R6.2.17 Boolchand P., Tenhover M. and Jena P., Phys. Rev. B 18 (1978) 3393.

R6.2.18 Campbell C.C.M. and Cameron J.A., J. Phys. F: Met. Phys. 6 (1976) L221.

R6.2.19 Boolchand P., Tenhover M., Jha S., Langouche G., Tripplet B.B. and Hanna S.S., Sol. St. Comm. 21 (1977) 741.

R6.2.20 Langouche G., Dixon N.S., Yahmud Y., Triplett B.B., Hanna S.S. and Boolchand P., Phys. Rev. C 13 (1976) 2589.

R6.2.21 Jena P. and Geldart G.J.W. J. Mag. Mag. Mat. 8 (1978) 99.

R6.3.1 Leiper W., Blaauw C., MacKay G.R. and Woodhams F.W.D., J. Phys. F: Met. Phys. 6 (1976) 2191.

R6.3.2 Leiper W., Rush J.D., Thomas M.F., Johnson C.E., Woodhams F.W.D., Blaauw C. and MacKay G.R., J. Phys. F: Met. Phys. 7 (1977) 533.

R6.3.3 Masumoto H. and Watanabe K., Trans. Jap. Inst. Met. 14 (1973) 408.

R6.3.4 Gorlich E.A., Kmiec R., Latka K., Matlak T., Buebenbauer K. Szytula A. and Tomala K., Phys. Stat. Sol. (a) 30 (1975) 331.

R6.3.5 Judah J., M.Sc Thesis, Dalhousie University, Halihax, N.S., CAN. (1978).

R6.3.6 Leiper W., MacKay G.R., Judah J., Blaauw C. and Rush J.D. Can. J. Phys. 50 (1978) 877.

R6.3.7 Arbique G., M.Sc. Thesis, Dalhousie University, Halifax, N.S., CAN. (1980).

R6.3.8 Rao K.R.P.M. and Iyengar P.K. Phys. Stat. Sol. (a) 59 (1973) 297.

R6.3.9 Campbell C.C.M., J. Phys. F: Met. Phys. 5 (1975) 1931.

R6.3.10 Dunlap R.A., March R. and Stroink G., Can. J. Phys. 59 (1981) 1577.

R6.3.11 Window B., J. Phys. E: Sci. Instr. 4 (1971) 401.

R6.3.12 Malik S.K., Damle S.D., Vijayaraghavan R., Le Dang K. and Viellet P. Sol. St. Comm. 15 (1974) 953.

R6.3.13 Watanabe K., J. Phys. Soc. Jap. 28 (1970) 302.

R6.4.1 Masumoto H. and Watanabe K., J. Phys. Soc. Jap. 32 (1972) 281.

R6.4.2 Arbique G., White C.G., Blaauw C.and Leiper W., Inst. Phys. Conf. Proc. 55 (1981) 603.

R6.4.3 Leiper W., Blaauw C., Judah J. and MacKay G.R. J. App. Phys. 50 (1979) 2072.

R6.5.1 Campbell I.A., J. Phys. C: Sol. St. Phys. 2 (1969) 1338.

R6.5.2 Jena P. and Geldart G.J.W., Sol. St. Comm. 15 (1974) 139.

CHAPTER 7

HYPERFINE FIELD AT Fe IMPURITIES IN HEUSLER ALLOYS Co_2YZ

S7.1 Introduction.

With the exception of hyperfine fields measured at Mn sites (Shinohara [R7.1.1, R7.1.2], Le Dang et [R7.1.3], Shinogi et al [R7.1.4]), few attempts have been made to measure hyperfine fields at transition metal impurity sites in Heusler alloys particularly, at magnetic sites. The primary reason for this lack of interest is due to the fact that theoretical models have not been developed which accurately estimate the core polarization effects due to the magnetic moment on the probe atom. However, by measuring the hyperfine fields at impurity transition metal atoms, information can be obtained regarding the sites in the alloy which these atoms preferentially occupy. Using off-stoichiometric samples can be useful in determining the effect of changing local order on fields measured at these probe atoms. The resulting hyperfine field shifts can then provide experimental estimates of the relative contributions to the hyperfine from the probe atom itself and from the neighbouring atoms. Extensive work along these lines has been done using the NMR technique for the Fe_3Si alloy. (For review see Burch et al [R7.1.5]).

Another interesting point is that the hyperfine field measured at various impurities in Fe, Co, and Ni hosts follow a rather smooth trend across a series in the periodic table whether or not the atom carries a magnetic moment (Balabanov and Delagin [R7.1.6]). These

authors have presented an empirical formula which, when fitted to the experimental data, leads to deviations of less than 20% in the worst cases. Burch et al [R7.1.5] have extended the use of the Balabanov-Delyagin relation in discussing impurity fields in Fe_3Si. The use of this formula requires knowledge of the moments on the 1nn atoms to the probe atom.

Despite these difficulties, the measurements of hyperfine fields at transition metal sites in Heusler alloys is of interest to determine if the trends observed across the transition series follow those observed for Fe, Co, and Ni hosts. Fields measured at Fe sites in Co_2YZ Heusler alloys are particularly suited for Mossbauer spectroscopy using the ^{57}Fe nuclide since the ^{57}Co parent used to fabricate the alloys guarantees that the hyperfine field will be measured at Fe nuclei located on A and C sites. Also the spectra obtained using alloys with dilute impurities of ^{57}Fe when compared with the "source" spectra give information regarding the sites which Fe atoms occupy in these alloys.

S7.2 Hyperfine Fields at Fe Sites in Co_2MnZ (Z = Ga,Ge,Si,Sn).

S7.2.1 Sample Preparation.

The sample preparation procedures were described in S4.2. For the Co_2MnSn and Co_2MnSi samples those containing ^{57}Co or ^{57}Fe impurities were annealed at 800 C for 10 to 65 hours followed by quenching into ice water. The doped samples of Co_2MnGa and Co_2MnGe were not annealed since X-ray diffraction analysis on the undoped samples both prior to and after heat treatment showed little change. These latter two samples were slowly cooled from the melt. The x-ray diffraction results indicated that these alloys were single phase and consistent with the $L2_1$ structure. The lattice parameters obtained in this work are given in T7.2.1 along with the magnetization X-ray and neutron diffraction data of Webster [R7.2.1].

In addition to these stoichiometric alloys another alloy of the composition $Co_2Mn_{0.85}Fe_{0.15}Sn$ was prepared. The ^{57}Co doped alloys were prepared by evaporating about 1mCi of ^{57}Co in dilute HCl solution on about 75 mg of each sample and remelting the doped sample by rf induction. The ^{57}Fe-doped alloys were prepared by adding about 2% ^{57}Fe by weight of the Mn to the undoped alloys and remelting them by rf induction.

T7.2.1 Magnetic properties of Co_2MnZ (Z=Ga,Si,Ge,Sn) alloys.

Host	Lattice parameter (Å)		T_C (K)	μ_{Co} (μ_B)	μ_{Mn} (μ_B)
	This work	R7.2.1	R7.2.1	R7.2.1	R7.2.1
Co_2MnSi	5.649(5)	5.654	985(5)	0.75(8)	3.57(16)
Co_2MnGe	5.735(5)	5.743*	905(3)	0.75(8)	3.61(16)
Co_2MnSn	5.994(5)	6.000	829(5)	0.75(8)	3.58(16)
Co_2MnGa	5.766(5)	5.770	694(3)	0.52(8)	3.01(16)

S7.2.2 Data Accumulation and Analysis.

Using a 20 m thick 310 stainless steel absorber for the source experiments with the ^{57}Co doped alloys and a $^{57}Co/Rh$ or $^{57}Co/Cu$ source for the absorber experiments with the ^{57}Fe doped alloys, room temperature spectra were accumulated for Z = Si,Sn,Ga,Ge and for the $Co_2Mn_{0.85}Fe_{0.85}Sn$ alloy. The resulting spectra are shown in F7.2.1 and F7.2.2. Each spectra was fitted using the assumption that all absorption lines were of equal width and of intensity ratios 3:x:1:1:x:3. The quadrupole splitting parameter was unconstrained in the fitting model as well. The signs of the hyperfine fields were measured by applying a 1.0 T transverse external field to the alloy

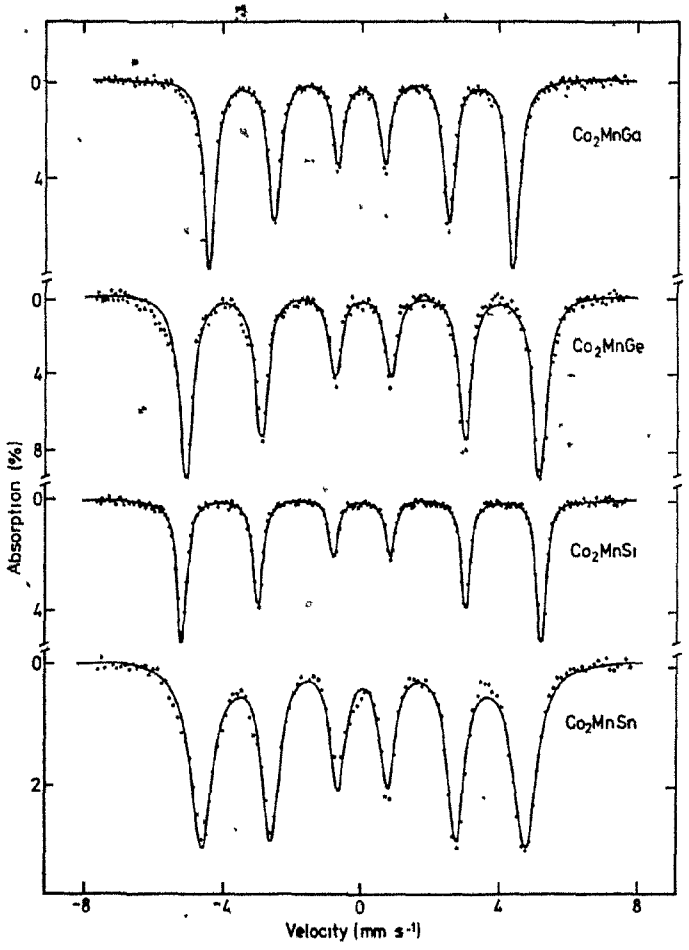

F7.2.1 Fitted room temperature spectra of $^{57}Co/Rh$ v.s. $^{57}Fe/Co_2MnZ$ (Z=Si,Ge,Sn,Ga).

during accumulation of another spectrum and visually comparing the spectra to those without an externally applied field. They were all found to be negative.

Using the value of T_C given by the magnetization data of Webster [R7.2.1], the hyperfine field values were extrapolated to T = 0 K. The results appear in T7.2.2 along with the values measured at Co

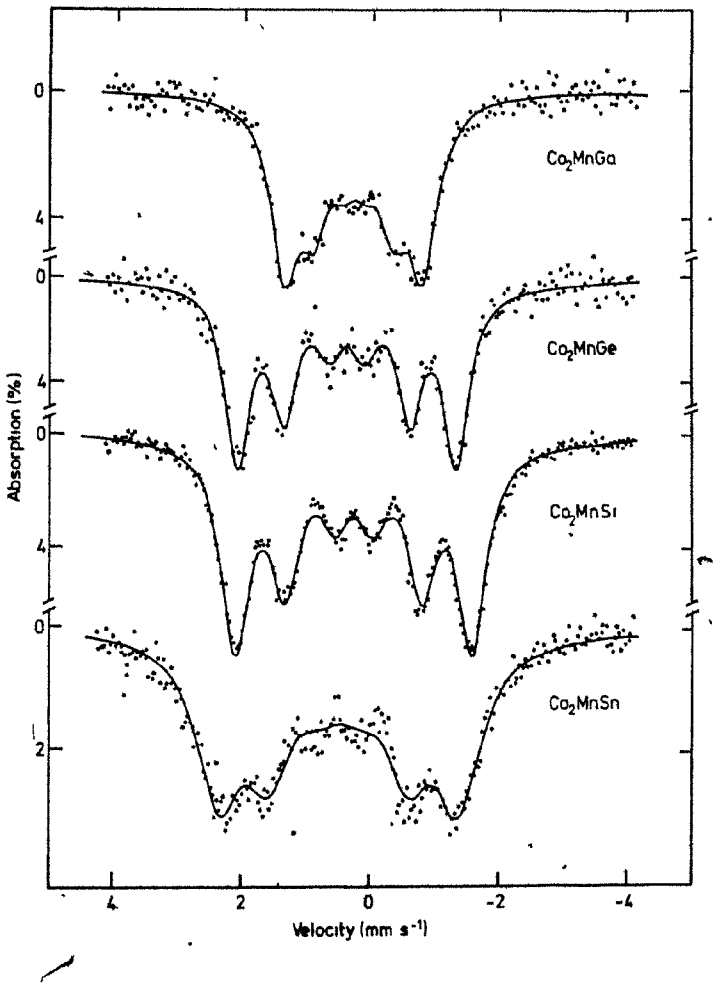

F7.2.2 Fitted room temperature spectra of $^{57}Co/Co_2MnZ$ (Z=Si,Ge,Sn,Ga) v.s. 310 stainless steel foil.

atoms on the A and C sites ($H_X(Co)$) at Mn atoms on the B sites ($H_Y(Mn)$) and at Sn impurity atoms measured on the D sites ($H_Z(Sn)$). The hyperfine fields measured in the alloys Co_2 MnAl, Cu_2 MnSn and Cu_2MnAl have also been included for comparison purposes.

T7.2.2 Hyperfine fields measured in Co_2MnZ Heusler alloys.

	Hyperfine fields (T)				
Host	$H_X(X)$	$H_X(Fe)$	$H_Y(Fe)$	$H_Y(Mn)$	$H_Z(Sn)$
Co_2MnSi	-14.6[a]	-11.9(2)[c]	-33.1(3)[c]	-33.7[a]	1.56[f]
Co_2MnGe	-14.1[a]	-11.2(2)[c]	-33.1(3)[c]	-33.9[a]	+0.62[f]
Co_2MnSn	-	-11.6(3)[c]	-30.0(3)[c]	-34.1[e]	+10.2[f]
$Co_2Mn_{0.85}Fe_{0.15}Sn$	-	-	-30.2(3)[c]	-	-
Co_2MnAl	-	-	-	-	+4.05[f]
Co_2MnGa	-17.3[a]	-7.5(2)[c]	-29.9(3)[c]	-28.0[a]	+3.52[f]
Cu_2MnSn	-17.5[b]	-	-19.6[d]	-23.1[b]	+21.4[g]
Cu_2MnAl	-21.4[b]	-	-20.0[d]	-21.4[b]	-

[a]R7.1.3 [b]R7.1.1 [c]This work [d]R7.2.10 [e]R7.1.2 [f]R7.2.7 [g]R7.2.11

S7.2.3 Site Preferences.

Burch et al [R7.1.5] have shown that transition metal impurities dissolved in Fe_3Si preferentially enter one of the inequivalent sites in this alloy. Because there are two inequivalent Fe sites in which the Fe moments differ, Fe_3Si may be regarded as a pseudo-Heusler alloy of composition Fe_2FeSi. These workers have found that the same types of atoms that enter a particular site in a Heusler alloy also

preferentially occupy the equivalent sites in Fe_2FeSi. Transition metals to the left and below Fe tend to occupy the B sites while the transition metals to the right of Fe tend to occupy the A and C sites. However, Fe is known to enter either the (A,C) or B sites as is evidenced by the existence of Fe_3Z (Z=Si,Al,Ga). Since the ^{57}Co samples give different field values than the ^{57}Fe samples, this seems to indicate that Fe preferentially enters the B or Mn site in Co_2MnZ alloys.

§7.2.4 Isomer Shifts.

The isomer shift data has been referenced to an iron foil absorber. The ^{57}Co source shifts have been converted to absorber shifts so that a direct comparison can be made between the source and absorber experiments. These isomer shifts are plotted in F7.2.3 as a function of the isomer shifts found at Fe atoms in Fe metal with one of the first nearest neighbour Fe atoms replaced by the corresponding 5sp impurity atom. These values were obtained from Van de Woude and Sawatzky [R7.2.2].

The straight lines are least squares fitted to the data for Fe on the two inequivalent sites in the Heusler alloy. The data clearly indicates a strong correlation between the effect of changing sp impurity atoms and the insomer shifts measured for Fe in the two hosts. This suggests that the same sort of mechanism is responsible for the isomer shifts in both systems. The stronger dependence of the isomer shifts for Fe on X sites then for Fe on Y sites is

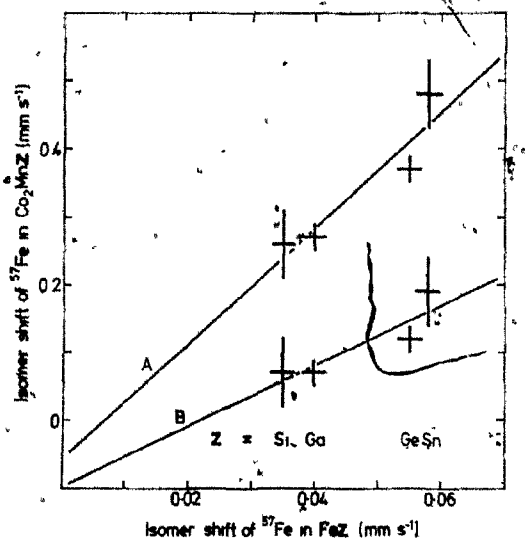

F7.2.3 Isomer shift correlations between Heusler Co_2MnZ hosts and dilute FeZ hosts.

consistant with the fact (See T2.2.2) that the X sites have four first nearest neighbour Z atoms while the Y sites have no first neghbour Z sites but six second nearest neighbour Z atoms. Hence, this correlation supports the assumption that Fe atoms in the alloys containing ^{57}Fe, occupy the Y sites instead of the Z sites where the nearest Z atoms are third nearest neighbours.

S7.2.5 The Magnetic Hyperfine Fields.

Examination of T7.2.2 clearly indicates that the hyperfine field measured at X sites in the Co_2MnZ alloys is about -10 T while that at Y sites is about -30 T. The trends for a more negative field at Y sites is consistent with the results found by Kawamiya et al [R7.2.3] in the "pseudo Heusler" alloys of the DO_3 structure, (Fe_3Z, Z=Al,Ga,Si), where the Y site fields are more negative without exception.

If one uses E5.8.1 to separate the contribution to the hyperfine field measured at a magnetic site due to magnetic moments on the neighbouring atoms from the contribution due to the local atomic electrons, then there is experimental evidence which suggests that only the first nearest neighbour need be considered, the effect of the other neighbours, especially those more distant than the second nearest neighbours, being negligible. Evidence for this conclusion is given by Drijver and Van der Woude [R7.2.4] who found that the variations of the hyperfine fields measured at Ni, Co and Fe in binary alloys with 12-coordination first nearest neighbours are linearly related to the average magnetic moment on this first nearest neighbour atoms alone. A similar conclusion has been reached by Burch et al [R7.1.5] for transition metal impurity fields measured in Fe_3Si. Work along these lines by LeDang et al [R7.2.5] for the Heusler alloy Co_2MnSi indicate that the contribution of the third nearest neighbours to the transferred component of the Mn hyperfine fields was only about +0.07 T.

These conclusions are consistant with the fact that the value of $H_Y(Fe)$ in Co_2MnSn is the same as the value obtained for $H_Y(Fe)$ in $Co_2Mn_{0.85}Fe_{0.15}Sn$. Here about an average of two 3nn Mn atoms to each Fe atom are changed to Fe atoms. Also the value obtained by Jaggi et al [R7.2.6] for $H_Y(Fe)$ in Co_2FeGa is -31 T which is very close to the value obtained for $H_Y(Fe)$ in Co_2MnGa. These results again seem to indicate that Fe selectively occupies the Y sites. Thus an understanding of the hyperfine fields measured at Fe atoms in the Co_2MnZ alloys can be obtained by considering core polarization effects and the transferred term due to only the nearest neighbour atoms.

Comparison of the values of $H_Y(Fe)$ and $H_Y(Mn)$ for Co_2MnZ alloys with the corresponding values for Cu_2MnZ alloys indicates the former are about 12 T more negative than the latter values. This is presumably due to the loss of the moments on the first nearest neighbour atoms when Co is changed to Cu. The larger moment (4.1 μ_B), on the Mn atoms in the Cu based alloys would have little effect on the different Fe field values because Mn atoms are third nearest neighbours to the Y atoms. However, the moments on the Fe atoms may differ in the two alloy systems and thus also contribute to changes in the core polarization component of the Fe hyperfine fields. Without a knowledge of these moments, it would be difficult to separate the local and transferred components of the hyperfine fields measured at Y sites.

Unlike the values of H_Y(Fe) the values of H_X(Fe) show a strong correlation with the valence of the Z element. In alloys where Z atom is from Group IVA of the periodic table (Si,Ge,Sn) the value of H_Z(Fe) is about -11.5 T while it is about -7.5 T for Z atom from the group IIIA of the periodic table. (Since this work Dunlap et al [R7.2.7] have found that the alloy Co_2MnAl can be made without the extensive disorder originally reported by Webster [R7.2.1]. It would be interesting to see if H_X(Fe) in this alloy is comparable to the value in Co_2MnGa.)

This trend is opposite to that found for H_X(Co) where the value for Z = Ga is more negative for Z = Ge or Si. However, the local contribution to the hyperfine field has been found to be positive by LeDang et al [R7.2.5] who suggest the negative core polarization is compensated for by a larger positive contribution due to an unquenched orbital moment on the Co atoms. Thus the hyperfine fields at Co sites may not follow the same systematics as those measured at other magnetic atoms. Experimental evidence for this is found in dilute Pd-Fe and Pd-Co alloys where Co is believed to possess an unquenched orbital moment while Fe does not (Senoussi [R7.2.8]).

The only other atom at which hyperfine fields have been measured in the Co_2MnZ alloys is the Sn atom (Dunlap and Ritcey [R7.2.9] and Dunlap and Jones [R7.2.7]). As can be seen from the T7.2.2 there appears to be no obvious correlation between these field values and the field values measured at magnetic atoms. This indicates that the local contributions in hyperfine field make a significant component

of the total fields at the magnetic sites.

S7.3 Hyperfine Fields at Fe Sites in Co_2YSn (Y=Ti,Zr,Hf).

These measurements were made to determine the influence of the Y atom on the Fe hyperfine fields at the various sites in the Co_2YSn alloys where Y =Ti,Zr,Hf and Mn.

S7.3.1 Sample Preparation.

The samples were prepared in a manner similar to those for the Co_2MnZ alloys according to the method used by Ziebeck and Webster [R7.3.1]. However, the spectra for these alloys were initially obtained without prior annealing of the samples. Subsequent spectra were obtained for the ^{57}Fe doped alloys after annealing for 24 hours at 900°C to obtain information as to which site the Fe atoms prefer to enter at high temperature. The results of magnetization data, x-ray and neutron diffraction by Ziebeck and Webster [R7.3.1] are given in T7.3.1.

S7.3.2 Data Accumulation and Analysis.

Using a ^{57}Co /Rh source and $^{57}Fe/Co_2YSn$ absorbers, spectra were accumulated with the absorber at both room temperature (RT) and at liquid nitrogen temperature (LNT). After the Heusler alloy absorbers were annealed at 900 C for 24 hours, the absorber spectra were accumulated at both temperatures.

T7.3.1 Structural and Magnetic Properties of Co_2YSn, (Y = Ti,Zr,Hf).

Host	Lattice parameter (Å)		T_C (K)	μ_{Co} (μ_B)
	This work	R7.3.1	R7.3.1	R7.3.1
Co_2TiSn	6.055(5)	6.218	359(4)	1.03(10)
Co_2ZrSn	6.215(5)	6.249	444(4)	0.80(10)
Co_2HfSn	6.202(50	6.218	394(4)	0.80(10)

By doping about 75 mg of the Co_2YSn alloys with about 1 mCi of ^{57}Co activity Heusler alloy sources were obtained. These sources were used with 310 stainless steel absorbers to accumulate RT spectra for these alloys.

The source spectra consisted of a broad single absorption line which was fitted to a sextet with area ratios constrained to 3:2:1:1:2:3 and equal line widths. The magnitude of the resulting fitted field values were less than 1.5 T.

The absorber spectra for these Co_2YSn alloys were much more complex than those found for the Co_2MnZ alloys as can be seen in F7.3.1. To check the local order and homogeneity of these samples, a ^{119}Sn spectrum of Co_2TiSn doped with ^{57}Fe was obtained. This spectrum contained, in addition to an expected sextet, two central

impurity singlets similar to those found by Endo et al [R7.3.2], Brooks and Williams [R7.3.3] and Gorlich et al [R7.3.4].

All absorber spectra required, in addition to sextets, one or two singlets in order to obtain a satisfactory fit to the experimental data points. These singlets are presumably due to non-magnetic impurity phases into which the iron atoms have entered. The existence of such phases is supported by the presence of the additional singlets in the ^{119}Sn spectrum of Co_2TiSn. The Co_2ZrSn, Co_2HfSn, and Co_2TiSn required one, two and three sextets, respectively, and two, two and one singlets, respectively, in order to be fitted. For the case of Co_2ZrSn, because of the relatively broad, weak lines, it is possible that there are two similar components present which cannot be distinguished by computer fitting. (The MOSFIT fitting program cannot fit two sextets corresponding to slightly differing hyperfine fields and isomer shifts because the relative intensities are not sufficiently well defined.) In the case of Co_2HfSn the two sextets corresponded to hyperfine fields and isomer shifts sufficiently different to allow the fitting program to distinguish between them. The third sextet found in the Co_2TiSn alloy had a small splitting, corresponding to 3.3 T at RT. This hyperfine field might correspond to one of the singlets which was observed in the other two alloys, although there seemed to be no internal correlation between the isomer shifts of these central absorption components in the three alloys. The values of these hyperfine fields extrapolated from the 77 K spectra to 0 K using the

T7.3.2 Hyperfine fields measured in Co_2YSn (Y=Ti,Zr,Hf).

Host	Hyperine Fields (T)					
Co_2YSn	$H_X(Co)$	$H_X(Fe)$	$H_Y(Y)$	$H_Y(Fe)$	$H_Z(Sn)$	$H_Z(Fe)$
Co_2TiSn	+2.12[a]	2	-	-34.3(5)	+8.5[c]	-28.5(5)
Co_2ZrSn	+4.46[b]	2	-	-35.1(3)	+10.4[c]	-
Co_2HfSn	+5.0[b]	2	-47(2)[a]	-35.9(5)	+12.0[c]	-31.1(10)

References: This work except [a]R7.3.6 [b]R7.3.7 [c]R7.3.4

magnetization data of Ziebeck and Webster [R7.3.1] are given in T7.3.2. In addition, the hyperfine field data at Co, Mn, and Sn sites in the three alloys are also given.

S7.3.3 Fe Site Preferences.

The absorber spectra indicate Fe impurities enters at least 4 inequilavent sites in the Co_2YSn samples, at least one of which, must be due to the presence of an impurity phase in the samples. This is in contrast to the Co_2MnZ alloys where Fe preferentially enters the Y sites. Due to this complexity in the spectra it considerably more difficult to determine which crystalographic sites of ^{57}Fe are responsible for the various components of the spectra. The sites designated in T7.3.2 are determined as follows.

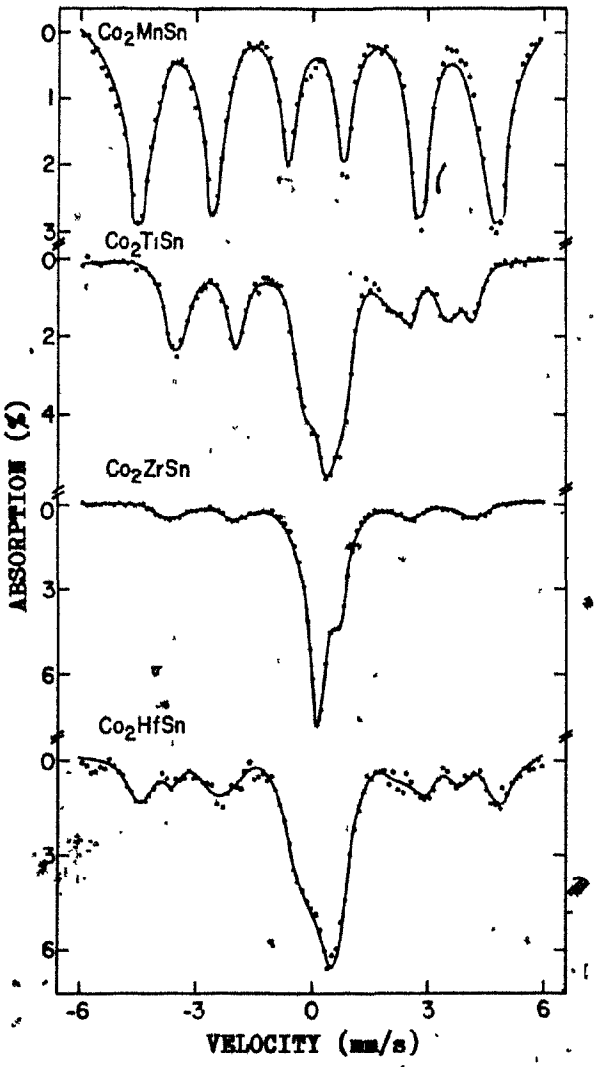

F7.3.1 Fitted room temperature spectra of $^{57}Co/Rh$ v.s. $^{57}Fe/Co_2YSn$ (Y=Mn, Ti, Zr, Hf).

The source spectra are due to Fe occupying the X sites since the ^{57}Fe nuclides are produced in situ from the ^{57}Co nuclides before the Mossbauer transition takes place.

The high field components of the absorber spectra are ascribed to Fe entering the Y sites because on annealing the absorption intensities of these components increased relative to the intermediate hyperfine field value in Co_2TiSn and Co_2HfSn. Since Fe is expected to enter the transition metal or Y site in preference to entering the sp metal or Z site on annealing, the high field components are probably due to Fe on the Hf or Ti sites. This designation is also applied to the Co_2ZrSn alloy even though the single high field component decreased upon annealing in this alloy.

The intermediate field values in the absorber spectra of Co_2TiSn and Co_2HfSn are attributed to Fe entering the Z sites. This is done because the local arrangement of the Moment carrying Co atoms around the Y and Z sites is the same in the 1nn shell. It is conceivable that this field is due to Fe being on Y sites where one of the first nearest Co atoms have been replaced by a non-magnetic atom. However, x-ray and neutron data [R7.3.1] indicate that there is insufficient disorder in the alloy to produce such a relatively strong absorption for this component in the spectra. In the case of Co_2ZrSn, it might be possible that there are two very nearly equal and unresolved high field components, and hence $H_Z(Fe) = H_Y(Fe)$.

Examination of the isomer shift data in T7.3.3 indicates that they are approximately equal for Fe occupying a particular site in all three alloys. This further supports the above site designations.

T7.3.3 Isomer shifts measured at Fe impurities in Co YSn, (Y=Ti,Zr,Hf).

host	Isomer Shifts (mm/s)		
	X Site	Y site	Z Site
Co_2TiSn	+0.33(4)	+0.25(10)	0.07(10)
Co_2ZrSn	+0.33(4)	+0.24(10)	-
Co_2HfSn	+0.33(4)	+0.20(10)	0.10(10)

As indicated previously, the central components including (the low field value in Co_2TiSn) revealed no internal correlations between their isomer shifts nor with those of the source spectra. This suggests that two singlets are due to Fe occupying sites in impurity non-Heusler phases.

S7.3.4 Hyperfine Fields.

The values of $H_Y(Fe)$ in the Co_2YSn (Y = Ti,Zr,Hf) are about 5.0 T more negative than the value of $H_Y(Fe)$ (-3.0 T) in Co_2MnSn. Since the Co moments are approximately equal (if the experimental uncertainities are taken into account) in all Co_YSn alloys, this suggests that the difference in these values is due to the presence of the Mn atoms which have large moments 3.58 μ_B as 3nn to the Y site Fe atoms. This implies that the transferred field per Bohr magnetism

per 3nn atom is +0.12 T/ $_B$ for total of +5.0 T. This agrees with the conclusions of LeDang et al [R7.3.5] who, using the NMR technique on non-stoichiometric Heusler alloys concluded that the component of the hyperfine measured at Mn atoms which was transferred from surrounding Mn atoms was positive. Another point is that this transferred field is relatively small in comparison to the total field, suggesting that the 1nn Co moments, even though much smaller than the Mn moments, are predominantly responsible for the hyperfine fields measured at magnetic atoms on the Y sites. This conclusion is consistent which the assumptions employed in the previous discussion of the hyperfine field systematics of the Co_2MnZ alloys.

The magnitude of the value of H_X(Fe) in the Co_2YSn (Y = Ti,Zr,Hf) alloys is considerably smaller than the H_X(Fe) value (-11.2 T) found in Co_2MnSn. This is consistent with the fact that in these former alloys the nearest atoms carrying moments to the X sites are the 2nn Co atoms while in Co_2MnSn the nearest atoms carrying a moment are the 1nn Mn atoms. Hence, the hypothesis that the 1nn magnetic moments dominate the transferred hyperfine field seems to be supported by the hyperfine field systematics of the X site as well as the Y site Fe hyperfine fields.

Because of the fact that the Y site atoms and the Z site atoms have the same local arrangement of Co atoms and the values of H_Y(Fe) and H_Z(Fe) do not differ by a large amount in these alloys, it would appear that the magnetic moments on the Fe atoms in both sites in these alloys are similar. There is no obvious explanation as to why

a distinct value for H_Z(Fe) in Co_2ZrSn was not observed, although it is possible that the values of H_Y(Fe) and H_Z(Fe), which have the same local arrangement of Co atoms, are not resolvable in the spectrum. However, if this is the case, it then represents an anomaly in that the magnitude of a hyperfine field measured with reasonable accuracy at a given probe atom increases with the atomic number of the Y host atom irrespective of the probe atom or the site on which it is located. The Co fields and the Sn fields became more positive while the Mn and Fe fields on the Y sites became more negative as Y varies from Ti to Zr to Hf. A similar trend occurs for the Mn and Sn fields in the Co_2MnZ (Z=Si,Ge,Sn) alloys. Except for the Co and Sn fields the change in the field values is quite small and may not be of any physical significance.

S7.4 References.

R7.1.1 Shinohara T., J. Phys. Soc. Jap. 27 (1969) 1127.

R7.1.2 Shinohara T., J. Phys. Soc. Jap. 28 (1970) 313.

R7.1.3 Le Dang K., Vijaraghavan R., Malik S.K. and Nagarajan V., Phys. Lett. 33A (1970) 435.

R7.1.4 Shinogi A., Vobchi Y., Endo K. and Kimura R., J. Phys. Soc. Jap. 34 (1973) 1418.

R7.1.5 Burch A., Budnick J.I., Niculescu V.A., Raj K. and Litventa T., Phys. Rev. B 24 (1981) 3866.

R7.1.6 Balabanov A.E. and Delyagin N.N., Sov. Phys. JEPT 27 (1968) 752.

R7.2.1 Webster P.J., J. Chem. Sol. 32 (1971) 1221.

R7.2.2 Van der Woude F. and Sawatsky G.A., Phys. Lett. C 12 (1974) 335.

R7.2.3 Kawamiya N., Adachi K. and Nakamura Y., J. Phys. Soc. Jap. 33 (1972) 1318.

R7.2.4 Drijver J.W. and Van der Woude F., J. de Physique C-6 (1976) 385.

R7.2.5 Le Dang K., Veillet P. and Campbell I.A., Physica 86-88B (1977) 413.

R7.2.6 Jaggi N.K., Rao K.P.R.M., Grover A.K., Supta L.C., Vijayaraghavan R. and Le Dang K., Hyp. Int. 4 (1978) 402.

R7.2.7 Dunlap R.A. and Jones D.F., Phys. Rev. B 26 (1982) 6013.

R7.2.8 Senoussi S., Campbell I.A. and Fert A., Sol. St. Comm. 21 (1977) 269.

R7.2.9 Dunlap R.A. and Ritcey S.P., Hyp. Int. 14 (1983) 195.

R7.2.10 Bjenjo B., Solly B., and Wikefeldt F., J. Phys. Chem. Sol. 31 (1970) 2289.

R7.2.11 Dunlap R.A., Ritcey S.P., Stroink G., and Hutt D., Sol. St. Comm. 45 (1983) 67.

R7.3.1 Ziebeck K.R.A. and Webster P.J., J. Phys. Chem. Sol. 35 (1973) 1.

R7.3.2 Endo K., Shinogi A. and Vincze I., J. Phys. Soc. Jap. 40 (1976) 674.

R7.3.3 Brooks J.S. and Williams J.M., Phys. Stat. Sol. (a) 32 (1975) 413,

R7.3.4 Gorlich E.A., Kmeic H., Latka K., Matlak T., Reubenbauer K., Szytula A. and Tomala K., Phys. Stat. Sol. (a) 30 (1975) 765.

R7.3.5 Ziebeck K.R.A. Ph.D. Thesis, University of Salford, England (1972).

R7.3.6 Le Dang K., Veillet P. and Campbell I.A., J. Phys. F: Met. Phys. 8 (1978) 1811.

R7.3.7 Caggio-Saitovitch E., Butz T., Vasquez A., Vincze I. Wagner F.E. and Endo K., J. de Physique C-6 (1976) 417.

R7.3.8 Vijayaraghavan R., Grover A.K., Gupta L.C., Itoh J., Shimizu K. and Misutani H., J. Phys. Soc. Jap. 42 (1977) 1779.

CONCLUSIONS AND RECOMMENDATIONS

S8.1 Systematics in the 5sp Series Hyperfine Fields in Pd_2MnSb

The magnitude of the hyperfine field measured at the Te impurity atoms on the Z site in Pd_2MnSb was found to be 85(3) T at a temperature of 4.2 K. The subsequent sign measurement by Boolchand et al [R8.1.1]and by de Waard and Lakshmanayana [R8.1.2] indicates that this is the largest positive value obtained for a 5sp impurity in the the Pd_2MnSb alloy indicating a saturation in the hyperfine fields for Z = Te. The models of Jena and Geldart [R8.1.3] and Campbell and Blandin [R8.1.4] are able to reproduce this saturation effect. However, the former provides better numerical agreement with the experimental values. The volume misfit model of Stearns [R8.1.5] was unable to reproduce this saturation in the hyperfine field curve for 5sp impurities.

It has been suggested that Pd_2MnSb, because it contains Pd atoms, exhibits an anomalous behaviour in the hyperfine field systematics [R8.1.6]. In order to verify this suggestion, the hyperfine fields at Te atoms substituted in other Heusler hosts should be determined. Recent work by Dunlap and Stroink [R8.1.7] suggests that neither the JG and the CB theory correctly predicts the trends observed at Sn impurities in the Co based Heusler alloys. It would be interesting to see if these theories also fail to predict the hyperfine field trends observed in the 5sp impurities in one of these alloys. Therefore, it is suggested that a ^{125}Te hyperfine field

measurement be undertaken in a Co_2MnZ or a Co_2YZ alloy. Because of the difficulties of incorporating Te into most Heusler matrices, a source experiment in which ^{121}Sb is incorporated in a Z=Sb alloy may be the only viable method of making this measurement.

S8.2 Hyperfine Fields at Non-Magnetic Sites in $C1_b$ Heusler Alloys.

The ^{119}Sn absorber spectra at the Z sites in the $C1_b$ alloys PtMnSn and $Ir_{1.07}Mn_{1.07}Sn_{0.86}$ tend to exhibit broad absorption lines indicating a lack of homogeneity in the local environments of the ^{119}Sn atoms. The values obtained for these hyperfine fields at liquid nitrogen temperatures were found to be -2.9(5) T for PtMnSn and 3.57(8) T for $Ir_{1.07}Mn_{1.07}Sn_{0.86}$. These small Sn hyperfine fields fit the general trend of the 5sp series hyperfine fields in the $L2_1$ Heusler alloys where the change in sign in the fields tends to occur near the Sn in the series.

The sign of the Sn hyperfine field in PtMnSn was found to be negative in disagreement with the results of Rao and Iyengar [R8.2.1] and Campbell [R8.2.2] but in agreement with the results of Leiper et al [R8.2.3] and Arbique [R8.2.4].

The magnitude of the hyperfine field measured at ^{197}Au impurity atoms in the PtMnSn alloy at 4.2 K was determined to be 71(1) T, while that of the hyperfine field at the Ir sites in $Ir_{1.07}Mn_{1.07}Sn_{0.86}$ was found to be 65(2) T at 4.2 K. These values along with the values of $H_x(Au)$ in AuMnSb [R8.2.5], $H_x(Au)$ in Au_2MnAl [R8.2.6] and $H_x(Pt)$ in PtMnSn [R8.2.7] were examined using the JG and

CB models to see if the general experimental trends of the hyperfine fields at these series six atoms could be reproduced. Although numerical agreement was rather poor, general experimental trends were reproduced using the JG model. However, the CB model which is sensitive to the local environment of the probe atom failed to reproduce the observed trends. This is particularly evident in the $Ir_{1.07}Mn_{1.07}Sn_{0.86}$ alloy where the off-stoichiometry of the sample greatly affects the resultant value of H_X(Ir). The volume misfit model of Stearns was not used because of lack of enough experimental hyperfine field values at X sites in these alloys necessary to evaluate the required numerical constants.

S8.3 Hyperfine Fields at Magnetic Impurity Sites in Co_2YZ.

In the alloys Co_2MnZ (Z = Si,Ge,Sn,Ga), Fe preferentially occupies the Y sites with a hyperfine field value of about -30 T. The hyperfine field at the Fe atoms on the X site, on the other hand, is typically about -11.5 T for a Z atom from Group IVa of the periodic table and -7.5 T for Z = Ga. The isomer shifts measured at the Fe atoms on both sites indicate that there is a strong correlation with the atomic number of the Z site atoms near the Fe probe atoms.

In the series of alloys Co_2YSn (Y = Ti,Zr,Hf) the Fe absorber spectra are very complex consisting of three or four components. The Fe atoms appear to enter both the Y and Z sites in these alloys. The Y site fields were found to be about -35 T while the Z site fields measured in Co_2TiSn and Co_2HfSn were found to be somewhat more

positive, -28.5 T and -31 T respectively. Fe atoms located on the X sites give unresolved fields in the range of -2 T to +2 T.

Because of the lack of knowledge of the magnetic moments on the Fe atoms, it is not possible to separate the transferred and local components to the total hyperfine fields measured. In the Co_2MnZ alloys where the spectra consist of a single component, a series of ^{57}Fe Mossbauer measurements using off-stoichiometric samples would provide information regarding the relative size of these two contributions and possibly some information about the size of the moments on the Fe atoms. It is recommended that this experiment be undertaken for one or several of these Co_2MnZ alloys.

S8.4 References.

R8.1.1 Boolchand P., Tenhover M. and Jena P., Phys. Rev. B 18 (1978) 3393.

R8.1.2 de Waard H. and Lakshimarayana V., Phys. Lett. A 67 (1978) 219.

R8.1.3 Jena P. and Geldart G.J.W., Sol. St. Comm. 15 (1974) 189; J. Mag. Mag. Mat. 8 (1978) 99.

R8.1.4 Blandin A. and Campbell I.A., Phys. Rev. Lett. 31 (1973) 51;
Campbell I.A. and Blandin A., J. Mag. Mag. Mat. 1 (1975) 1.

R8.1.5 Stearns M.B., Phys. Lett. A 34 (1971) 146; Phys. Rev. B 4 (1971) 4081; 8 (1973) 4383.

R8.1.6 Boolchand P., Tenhover M., Marcuso M., Blizzard M., Kim C.S., Langouche G., van Rossum M. and Coussement R., Hyp. Int. 4 (1978) 388.

R8.1.7 Dunlap R.A. and Stroink G., J. App. Phys. 53 (1982) 388.

R8.2.1 Rao K.P.R.M. and Iyengar P.K., Phys. St. Sol. (a) 59 (1973) 297.

R8.2.2 Campbell C.C.M., J. Phys. F: Met. Phys. 5 (1975) 1931; Ph. D. Thesis, Dalhousie University, Halifax, N.S., CAN. (1974).

R8.2.3 Leiper W., MacKay G.R., Judah J., Blauuw C., and Rush J.D., Can. J. Phys. 56 (1978) 877.

R8.2.4 Arbique G., M.Sc. Thesis, Dalhousie University, Halifax, N.S., CAN. (1980).

R8.2.5 Leiper W., Rush J.D., Thomas M.F., Johnson C.E., Woodhams F.W.D., Blaauw C. and MacKay G.R., J. Phys. F: Met. Phys. 7 (1977) 533.

R8.2.6 Leiper W., Blaauw C., MacKay G.R. and Woodhams F.W.D., J. Phys. F: Met. Phys. 6 (1976) 2191.

R8.2.7 Malik S.K., Damle S.D., Vijayaraghavan R., Le Dang K. and Veillet P., Sol. St. Comm. 15 (1974) 953.